Laser ablation driven by femtosecond optical and XUV pulses

Vom Fachbereich Physik der Universität Duisburg-Essen zur Erlangung des akademischen Grades eines Doktors der Naturwissenschaften genehmigte

Dissertation

von

Nikola Stojanovic

aus

Beograd

Referent: Prof. Dr. Dietrich von der Linde

Korreferent: Prof. Dr. Marika Schleberger

Tag der mündlichen Prüfung: 20.11.2008

Mom dedi Milošu.

To my grandfather Miloš.

Acknowledgements

I would like to thank to Prof. Dietrich von der Linde and Klaus Sokolowski-Tinten for providing me an opportunity to work on the ablation studies described in this thesis.

Special thanks to Klaus Sokolowski-Tinten, Ping Zhou and Ivan Rajkovic, for being in the lab with me for many extra hours and helping me solve the unsolvable problems.

This list can not be complete without people like Matthieu Nicoul, Konstantin Lobov, Wei Lu, Manuel Ligges, Stephan Kähle, Oliver Heinz, Uladzimir Shymanovich and Jan Göhre whom I could depend on, for help from scientific expertise to solving mundane lab problems. I would also like to thank our "technical staff", Michael Bieske, Bernd Prof and Doris Steeger, whose technical knowhow saved me from typical scientific clumsiness. Thanks to Kay Eibl for help on all administrative issues that I had to deal during the years.

I am grateful to Prof. Marika Schleberger and Prof. Lothar Schäfer for their agreement to review my dissertation.

I thank Eplinius and Igelbrink families for hospitality and warmheartedness that they let me enjoy for the last four years.

My family in Belgrade will always have my gratitude, for support and love that I enjoyed all my life, even now far away from home.

Many thanks to Ana Stojanovic, Aliya Sadvokassova, Jelena Falatov and Branislav Uzelac, for keeping me (almost) sane during my writing process.

Contents

Chapter 1

Introduction

1.1 Importance of understanding laser ablation

Pulsed laser ablation is the process of material removal from a target after it has been irradiated by an intense laser pulse. This phenomenon has found use in several industrial and medical applications (micromachining [1], cleaning [2], annealing [3], growth of thin films [4], production of nanoparticles in vacuum [5, 6] and aqueous solutions [7, 8], surgery [9]).

With a suitable choice of the laser parameters (i.e. wavelength, intensity and pulse duration) laser ablation can be tailored to achieve specific structuring objectives (depth, surface quality, machining of transparent materials, etc.) in a wide range of materials. The use of ultrashort pulses (sub picosecond) confines heat diffusion in the sample, high temperatures needed to ablate material are reached in a small volume and a significant part of the absorbed energy is transferred to ejected material[9]. New possibilities have been opened up for the fabrication of optically transparent materials [10] and subwavelength structuring [11, 10, 12].

In the medical laser applications, the laser radiation applied in the form of short pulses, ablates tissue with minimal thermal side-effects and high efficiency.

1.1.1 Ablation mechanisms and motivation for further research

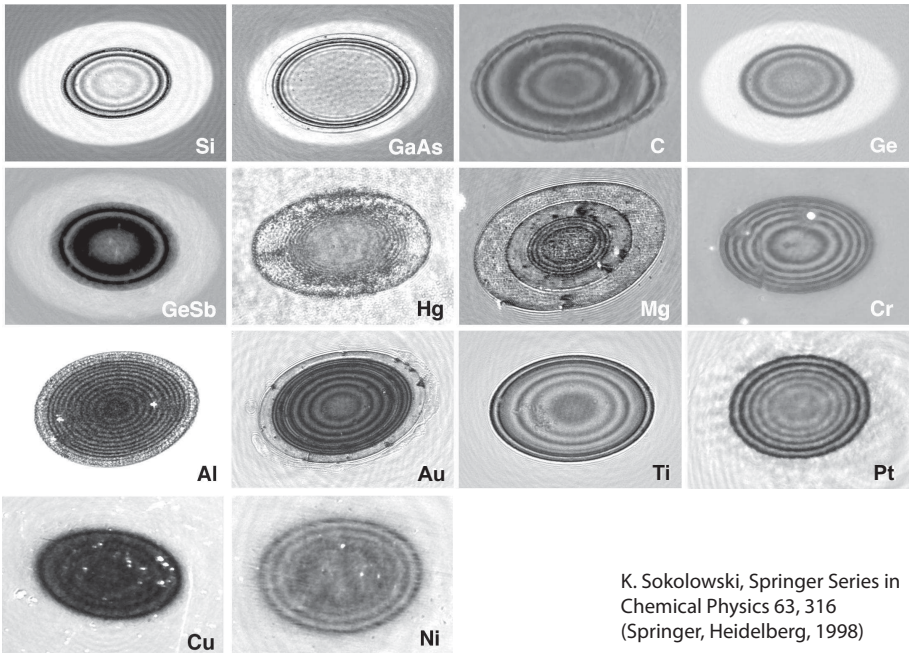

Figure 1.1: Surface reflectivity snapshots during ablation on absorbing solids. Images are taken several nanoseconds after irradiation by a single intense femtosecond laser pulse. Optical interference pattern (Newton rings) formation indicates mechanism of femtosecond laser ablation.

The craters produced during the ablation of absorbing materials by single femtosecond pulses have well defined boundaries [13], which indicate a sharp ablation threshold. Time resolved optical studies have revealed important characteristics of the ablation process: an optically sharp ablation front and an apparently transparent ablation plume. On all the investigated materials a clear interference pattern (Newton rings) is observed in the ablating area a few nanoseconds after the laser irradiation [14, 15]. As an example, snapshots of different materials a few nanoseconds after excitation by a single laser pulse, are presented in figure 1.1.

The formation of a steep ablation front in which the density drops sharply over a distance smaller than the probe wavelength is proposed as a possible

ablation mechanism. A homogeneous liquid forms a bubble-like structure with a highly reflective outer shell [16], while the inside of the shell is filled with a a transparent mixture of liquid and gas. The optical probe light forms an interference pattern in the form of Newton rings. The principle scheme of the formation of Newton rings in this model is given in Figure 1.2.

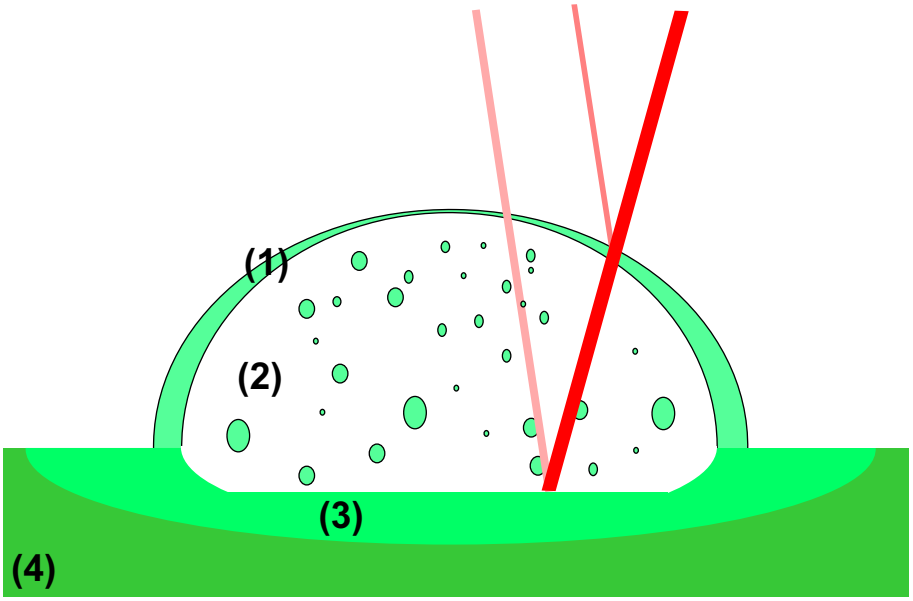

Figure 1.2: Scheme of formation of Newton rings, during the ablation process, near the ablation threshold fluence. Ablation shell (1) moves away, and reflected and transmitted light interfere. After certain time (typically, several hundreds of picoseconds), the two phase material (2) inside the shell becomes transparent enough , so that the transmitted light is not significantly absorbed. Upon reflection from crater bottom (3) passes once again through shell, and it interferes with the portion of the light which is reflected from the shell.

The hydrodynamic calculations, modeling fs-laser induced ablation [17, 18, 19], were first used to describe this process. Here one assumes that the material is heated instantaneously and than expands without any restrictions. This expansion is assumed to be adiabatic, because it occurs occurs on picosecond to nanosecond timescales and energy exchange with the environment is negligible. The expanding material passes through a liquid-gas coexistence regime and forms a thin shell. The material inside the shell consists of a low density

two-phase mixture with sound velocity orders of magnitude lower than in unexcited material. This low sound velocity is found to be a reason for formation of steep ablation front and subsequent shell formation. The shell is observed to expand with a constant velocity. The formation of the high reflectivity shell and transparent two phase material inside explains the appearance of the Newton rings. The sharp crater boundary and the sharp ablation threshold have not been explained by this model.

Molecular dynamic (MD) simulations of ablation, induced by fs-laser pulses, confirm the results of hydrodynamic calculations: material heated with fluences above the ablation threshold forms a liquid shell which expands with a constant velocity [20, 21, 22]. However, around the ablation threshold the main mechanism of material removal is material rapture induced by tensile stresses in the expanding material. This process is called spallation. It has been observed that for material excited below the ablation threshold, voids form in the material and than recollapse, leading essentially to no material removal.

The already mentioned Newton rings that appear following the femtosecond laser ablation were observed experimentally using the time resolved microcopy technique designed by Downer *at al* [23]. Using this technique, one can follow the evolution of material reflectivity, i.e. the amplitude of the probe light used to investigate the ablation process. However, the information about surface deformations that appear as result of the laser heating, particularly below the ablation threshold, can not be obtained using only reflectivity measurements, because this information is contained in the *phase* of the reflected light, rather than in its amplitude.

The phase of light can be measured interferometrically, and an experimental setup utilizing time resolved interferometric microscopy was designed by Temnov at al [24, 25] to study transient surface deformations during laser ablation. Indeed, first experiments using this technique show expansion of the ablation front on GaAs. Above the ablation threshold, the expanding front moves with

constant velocity, thus confirming the results of hydrodynamic and MD calculations. Below the ablation threshold, the surface is observed to expand and retract on a nanosecond timescale. These long-lasting reversible surface deformations are observed on GaAs as well as on Si, and they are interpreted as an indication for the formation of transient voids as predicted by the MD simulations.

As Newton rings (figure 1.1) indicate some "universality" of the ablation mechanism, two questions arise: first, are reversible deformations below the ablation threshold unique for GaAs and Si, or is this a more general mechanism (meaning that this behavior is material independent); second, does the expansion velocity above the ablation threshold scale with fluence, as predicted by hydrodynamics and MD calculations, for different materials like it does for GaAs.
As an attempt to give answers to some of these questions, the ablation behavior of a number of elemental metals (representing materials with a simpler structure) has been studied by time resolved interferometry, and the results, and the results are presented in this thesis.

Typical threshold fluences needed to induce ablation with femtosecond optical pulses are in the range of a $0.1 - 1 J/cm^2$ corresponding to intensities of about $10^{12} - 10^{13} W/cm^2$. Due to these high intensities energy deposition is in most cases influenced or even dominated by non-linear absorption mechanisms. This can drastically change the amount of energy that is absorbed, from the value expected from the optical constants [26, 27, 28].
However, if the photon energy is much higher than for visible light the influence of optical non-linearities is strongly reduced. The recent appearance of short-wavelength accelerator-based light sources [29, 30] has made it possible to use the short- wavelength femtosecond radiation as excitation as well as probe. The extreme ultraviolet XUV free electron laser in Hamburg (FLASH) at the Deutsches Elektronen- Synchrotron (DESY) in Hamburg, Germany is is cur-

rently the only self-amplified spontaneous emission FEL [31] operating in the 6−100 nm wavelength range.
The first results from the experiments that use the femtosecond XUV radiation to induce the ablation, are presented in this thesis.

1.1.2 Contents of the thesis

This thesis is divided in to two parts, both dealing with the ablation by femtosecond laser radiation. The part describes new results of ablation on metals by near infrared irradiation (NIR). Observed slow expansion, for fluences below the ablation threshold, motivates further research on metals as materials with simpler properties (optical and mechanical). Chapter 3.1 deals with the layout of the experimental setup (interferometric microscopy) used to follow small surface deformations induced by laser heating, and specific problems associated with metal samples. Section 3.2 gives an overview on the morphology of the ablation craters and demonstrates the specifics of different materials with respect to ablation in the spallation regime. As study on transient reflectivity changes and the formation of Newton rings, as the first indication on specific of femtosecond laser ablation, is presented in the section 3.3. Together with the ablation crater morphologies, The Newton rings give an insight into the different mechanisms of ablation.
The result of interferometric measurements, i.e. studies of the expansion dynamics on Au, Al, Pt and Ti are presented in the section 3.4.

The chapter 4 gives a short report on first results of ablation experiment where the XUV femtosecond radiation has been used, with emphasis on semiconductors (Si and GaAs).

Chapter 2

Different regimes of ablation: theoretical considerations

Heating of the near-surface layer a solid material by femtosecond laser pulses can be regarded as isochoric because the deposition of energy and its thermalization (transfer of energy from the optically excited electrons to the lattice) occur much faster (within a few ps) than any material expansion. Therefore, just after thermalization the material is in a state of high temperature and pressure. The excess pressure drives then the hydrodynamic expansion of the heated layer towards vacuum (or the ambient atmosphere). This expansion is essentially isentropic/adiabatic since it occurs on 100s of ps to ns-timescales which is too fast for any significant heat exchange.

In the work by Perez and Lewis [21], the isochorically heated and adiabatically expanding material was found to material was found to decompose in different manners depending on the magnitude of the irradiation fluence. They suggested that near the ablation threshold the spallation of the material represents the main mechanism of decomposition, followed by the so-called phase explosion,

fragmentation and finally evaporation. The term spallation describes the process of material decomposition due to strong tensile forces, which exceed the absolute tensile strength of the material. These forces are generated by rapid material expansion that follows fast heating. In the schematic pressure-density ($p - \rho$) phase diagram shown in figure 2.1 this process corresponds to the expansion along the isentrope (c), where the isochorically heated material reaches the negative pressure region upon expansion. A negative pressure (i.e. tensile forces in material) of sufficient magnitude will lead to material rapture.
The decomposition of the rapidly heated liquid, which, during the expansion, enters the two phase (liquid-gas) region by *cooling* adiabatically, is named *phase explosion*, and in the $p - \rho$ diagram it is represented by line (b). The material, which is heated to sufficiently high initial temperatures, will expand above the critical point (expansion along line (a) in Fig. 2.1), and ablation is governed by fragmentation and evaporation [21, 32, 33].

In the regimes of both spallation and phase explosion, the expanding material is expected to form a flying shell structure [21, 32], which represents a sharp interface for optical probe radiation. This shell can be experimentally observed by the appearance of Newton rings and represents the surface which can be followed in time resolved interferometric experiments (see Chapter 3). The mechanisms of spallation and phase explosion will be discussed in this chapter.

2.1 Phase Explosion

The phase explosion mechanism of material decomposition will be discussed first, as this was the first proposed mechanism to explain the rapid removal of material during ablation induced by intense femtosecond pulses. Phase explosion or explosive boiling has been first discussed in the context of nanosecond laser ablation [34, 35] when the material gets overheated (at temperatures close to the critical temperature) due to fast heating during the expansion process.
Phase explosion or explosive boiling happens when thermal energy is deposited

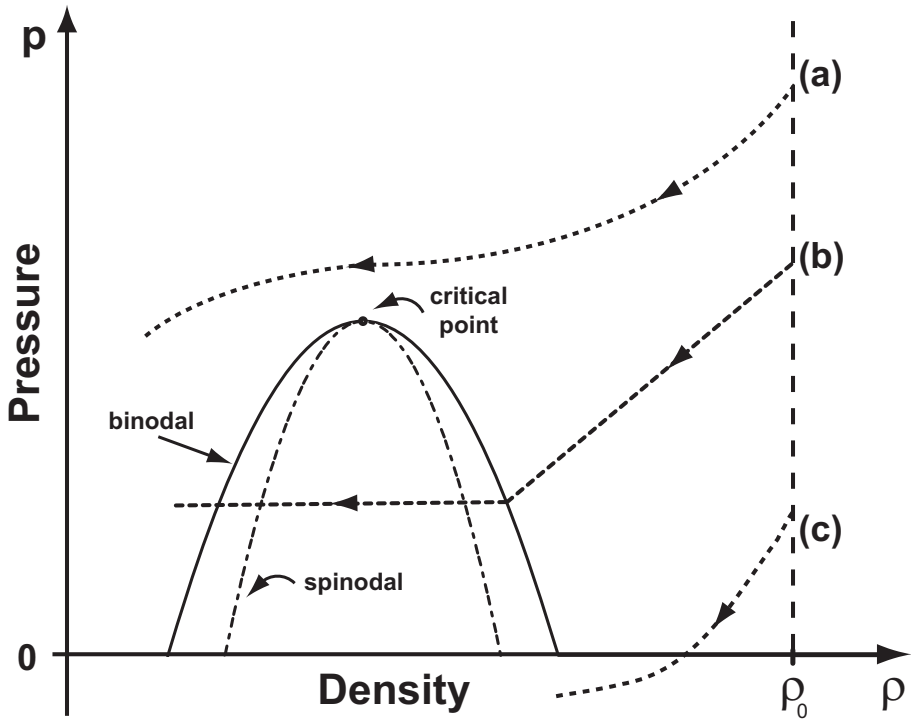

Figure 2.1: Scheme of the pressure density diagram for rapidly heated material(vertical dashed line at ρ_0) that expands along isentropes, for three different initial temperatures. For the isentrope (a) expansion is above the critical point, for (b) it goes through the two phase mixture, and for (c) it reaches the negative pressure region. (Adapted from Temnov 2004 [25])

too fast for normal boiling [1] to occur.

Phase explosion will also occur after excitation with ultrashort laser pulses. The material becomes overheated, although it cools upon adiabatic expansion, because it is rapidly driven into the metastable part of the phase diagram between the binodal and the spinodal. The phase transformation proceeds in an explosive fashion, as overheated material relaxes by decomposing into a mixture of the liquid droplets and the molecules in the gas phase.

Phase explosion occurs in a material when expansion isentrope crosses the binodal between the critical and the triple point. After crossing the binodal, the pressure inside the liquid is lower than the saturation vapor pressure, and there-

[1] here normal boiling refers to formation of gas bubbles as consequence of heating of the material

fore the homogeneous liquid is not in a stable configuration, since the free energy of the gas is lower than that of the liquid [36]. Nucleation of the gas bubbles proceeds when the pressure is decreased below the saturated vapor pressure, either by adiabatic expansion, or by the passing of the tensile wave [21]. The ablation is caused by the rapid transition of superheated liquid to a mixture of liquid droplets and gas.

Upon crossing the binodal line a drastic decrease of the local sound velocity occurs. Since the sound velocity is defined as $c_s = \sqrt{\frac{\partial p}{\partial \rho}}_S$ this drop manifests itself as a kink of the isentrope at the binodal. Qualitatively this behaviour can be understood by considering that large variations of the average density can occur at nearly constant pressure by changing the ratio of the two phase components.

This drop of the sound velocity has important consequences for the denisty profile that forms during the expansion. In the initial stage of expansion, the jump in sound velocity leads to the formation of a steep front in the rarefaction wave [14, 16, 18, 37]. Upon reflection of this wave on a "cold" (non-ablating) part of the sample, or back surface, a thin shell of condensed material is formed which moves away with a constant velocity [14, 16]. The velocity can be estimated to scale as $v_{exp} = c_0 \ln(\frac{\rho_1}{\rho_0})$ [14], where c_0 is the initial sound velocity in the unexcited material, ρ_0 is the initial solid density, and ρ_1 is density at the point where the isentrope crosses the binodal.

In recent calculations by Anisimov *at al* [32] it has been shown that the shell thickness scales with the incident fluence. When the ablating shell becomes thin enough that a significant portion of the probe light is transmitted and interferes with the reflected light, it will produce the typical Newton rings pattern already mentioned in the Introduction.

2.2 Negative pressures

The negative pressure states for liquids are metastable states and they are closely related to the superheated states. In both cases rapid expansion after isochoric heating is the driving mechanism. While a superheated liquid becomes unstable with respect to the vapor phase leading to phase explosion, a material can become mechanically unstable when the negative pressure (tensile stress) comes close to or exceeds the tensile strength of the material. In this case the sudden nucleation and growth of voids (cavitation) will occur which represents the first step in the mechanical rupture of a material (also called spallation).

Here I discuss in some more detail the thermodynamic pathways by which a material can reach the region of negative pressures. As an example I use Aluminium, for which a well-tabulated equation of states exist and which has been extensively studied both experimentally and theoretically. The initial temperature at the ablation threshold is estimated from the incident laser fluences in order to compare it with the characteristic temperatures in the phase diagrams. Using simple linear acoustics for two distinct situations, namely a homogenously heated (thin) film and a bulk material with some temperature profile, the propagation of strain and pressure waves is calculated and its implication on the spallation process is discussed.

2.2.1 Equation of states for Aluminium

The equation of states allows us to follow the thermodynamic pathways of material from initial heating and during subsequent expansion. Tables for the equation of states (EOS) are available for a range of materials [38]. As an example the phase diagram for Aluminium is presented in figure 2.2.

It is assumed that the initial heating is instantaneous and thus iscochoric on thermodynamic timescales [16], depicted with a vertical dashed line (ma-

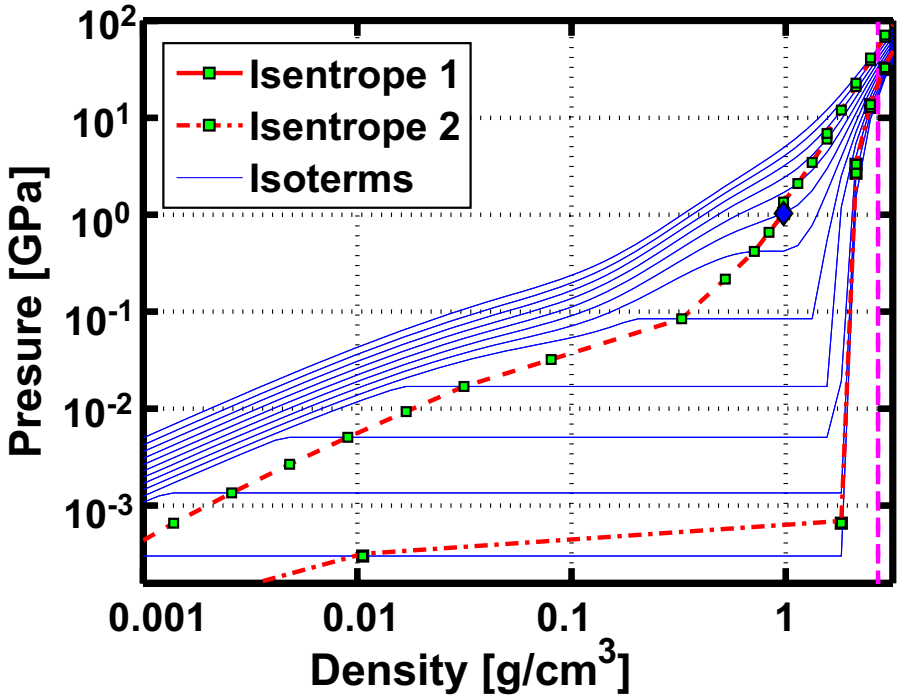

Figure 2.2: Phase diagram for Aluminium - logarithmic scale, thick red dashed lines are isentropes and full thin blue ones are isotherms (3049 K - 16416 K). Upper isentrope starts at the initial temperature T=15836 K and solid Al density ($\rho = 2.7\text{g/cm}^3$), and it goes through the critical point for Aluminium (blue diamond, T_c=7151 K, P_c=0.5458 GPa). Lower isentrope starts from temperature T=4563 K and this is the lowest temperature for which isentrope still enters two phase region.

genta color), and starts at the solid density of Aluminium (2.7 g/cm^3). Typical expansion timescales extend into the nanosecond region, and we assume that the exchange of thermal energy with the environment is negligible. Therefore, expansion is adiabatic and the material expands along isentropes. The isentropes are represented with red dashed lines in p$-\rho$ diagrams (isotherms are represented by thin solid blue lines). Two isentropes (marked as 1 and 2 in figure 2.2), drawn as thicker dashed red lines connecting the green points, represent adiabatically expanding material which is initially heated to the temperatures T_1=15836 K and T_2=4563 K. The higher one (isentrope 1) passes thorough the critical point for Aluminium (T_c=7151 K, P_c=0.5458 GPa), and the lower one

(isentrope 1) is the isentrope with the lowest initial temperature available from the tables, that does not enter the negative pressure region. These two isentropes limit the range of initial temperatures where the subsequent expansion leads into the two-phase region of the phase diagram and where phase explosion is the responsible ablation mechanism. Moreover, isentrope 1 also represents the upper limit for the appearance of Newton rings because the formation of a steep ablation front requires a significant drop in the sound velocity which is associated with crossing of the binodal.
On the other hand, the isentrope 2 marks the upper limit of the ablation threshold temperature, since the material which passes through the two-phase region definitely ablates. These two temperatures define the region of initial temperatures for which the material reaches the two phase region when it is expanding along isentropes.

In order to follow the isentropes into the negative pressure region, the pressure density diagrams are ploted in linear scale (see figure 2.3). The isentropes represent material heated to the initial temperatures T_2=4563 K and T_3=3164 K respectively. Material expanding along isentrope 3 (figure 2.3) reaches the negative pressure region and it reaches maximal amplitude of $p = -0.4$ GPa. This value exceeds the static tensile strength of solid Aluminium [2] by a factor of 10.

In the next section the initial temperature at the ablation threshold is estimated to be T_{abl}=2528K. For this temperature, the adiabatically expanding material, reaches negative pressure down to the value of the $p = -2$GPa, which greatly exceeds the static tensile strength of solid aluminium. This observation indicates that close to the threshold negative pressures (tensile stresses) play an important role and ablation is indeed caused by spallation.

[2] 40-50 MPa [39]

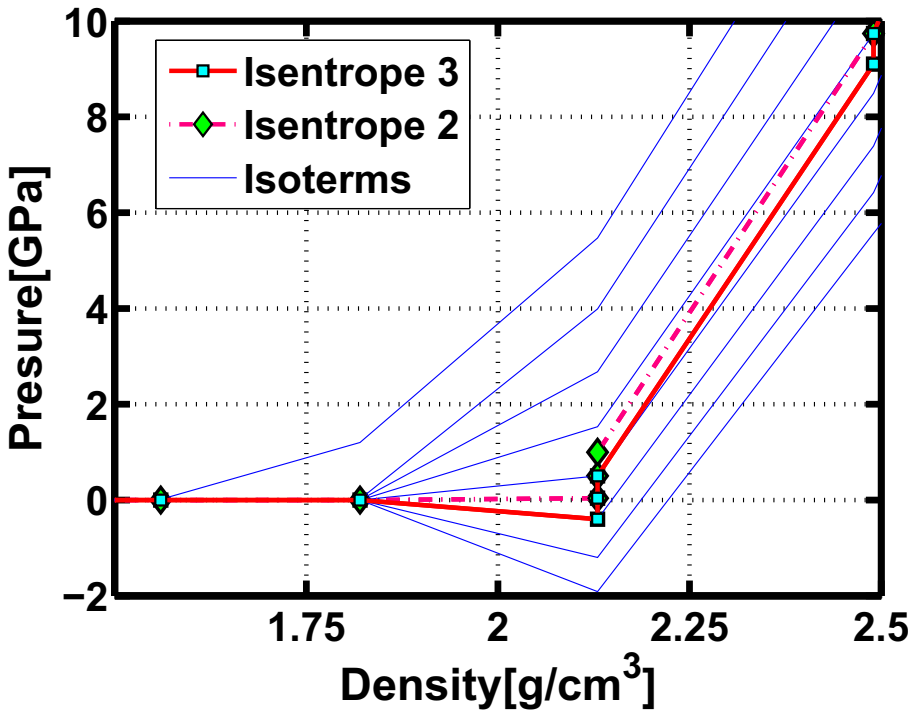

Figure 2.3: Thicker dashed red line (with diamond points) is lower isentrope from graph (a), starting at initial temperature T=4563K, thin dashed blue lines are isotherms (1697K-5089K). Full line (with rectangular points) is isentrope, starting at initial temperature T= 3164K. This is the first isentrope reaching the negative pressure region. Negative pressure is $p = -0.4$ GPa. The tensile strength of solid Aluminium has a maximal value of 50 MPa.

2.2.2 Estimation of the initial temperature for ablation threshold

In order to compare the material expansion along different isentropes in the phase diagram, it is important to know the initial temperature of the material that undergoes adiabatic expansion.

Here I use simple energy considerations to estimate the initial temperature for a given laser fluence. Energy per unit of volume needed to melt the material, is estimated from the following equation:

$$E_m = [c_p(T_M - T_0) + L_M]\rho_0 \tag{2.1}$$

where c_p= 888 $\frac{J}{kgK}$ is the heat capacity (which is assumed to be constant in this estimation), T_M=933 K the melting temperature, T_0=300 K is the room temperature, L_M= 3.96×10^4 J/kg is the latent heat of fusion and ρ_0=2.7 g/cm^3 is the density of solid aluminium.

The absorbed energy is estimated from the incident fluence: $F_{abs} = (1 - R) \cdot F_{inc}$, where R is the reflection coefficient and F_{inc} is the incident fluence. For aluminium reflectivity is R=83% at the wavelength λ= 800 nm and angle of incidence 35° [3]. The rise of the temperature, above the material melting temperature is estimated using the following equation:

$$\Delta T = \frac{\frac{F_{abs}}{d} - E_m}{c_p \rho_0} \tag{2.2}$$

where d is the the thickness of the excited layer. In this example I assume a film thickness of 100 nm that is homogeneously heated. This thickness has the same value as one of the investigated aluminium films which will be presented later.

The ablation threshold fluence for aluminium[4], is measured to be F_{th}=0.42 J/cm^2 and the calculated initial temperature rise at this fluence is T_{abl}=2528 K. According to the presented thermodynamic phase diagram, adiabatic expansion starting at this initial temperature pushes the material deep into the negative pressure regime, supporting the conclusion of published MD simulations that the ablation threshold is mainly governed by the tensile forces generated in the material [21, 21].

Considering the high peak intensities and observed change of reflectivity for various materials, a question arises: how accurate is this simple estimate of deposited energy. Considering that the absorbance (1-R) has a relatively high value (approximately 20%), even the variation in reflectivity up to 5% due to high irradiation intensity[5] does not drastically change the amount of deposited

[3] value for reflectivity is calculated using optical constants [40]

[4] irradiated with $\pi-$ polarized light

[5] Typical peak intensities for ablation close to the threshold are in the range of 10^{-12} –

energy. Namely, for a wide range of fluences, the reflectivity for aluminium remains almost constant[6] during the laser pulse [41], the real temperature rise is not expected to differ much from this estimate.

Another example discussed here concerns gold film. Using the published values for the optical constants, reflectivity of gold is much higher than that of aluminum and therefore absorbance is low (approximately 4%)[40]. Therefore, even small changes of the reflectivity [7] or deviations from the expected value can lead to a significant variation of the absorbance and a respective change in the estimated amount of deposited energy.

Contrary to aluminium, gold self- reflectivity decreases with increasing intensity during the irradiation with fs laser pulses for absorbed fluences between 1-10 J/cm^2 as reported by several investigators [42, 27, 28]. This effect could lead to an underestimation of the energy deposited in a sample compared to the real value. However, the absorbed fluence range in above mentioned studies is two to three orders of magnitude higher than the fluences used to induce ablation[8], so it is reasonable to assume that there is no significant change of reflectivity for fluence range around the ablation threshold.

In order to get a reliable estimate of the absorbance of the gold films used in the experments, the reflectivity of these films have been measured for low fluences (results are presented in Appendix C). The measured values are significantly lower than from what was expected from optical constants. Using these values together with the measured ablation threshold fluences, the initial temperatures at ablation thresholds are calculated using the same procedure as for aluminium. The estimated initial temperature at the ablation threshold is 2837 K for a 34 nm thick film, 1877 K for a 57nm thick film and 1020 K for 125nm thick film. What is interesting to note here is that only for the 34 nm film the estimated temperature is significantly higher than the melting temperature. Although

$10^{-13} W/cm^2$

[6] Reflectivity remains constant up to a few percent.

[7] up to 5%

[8] For approximately 1J/cm^2 incident fluence at ablation threshold and more reflectivity higher 90%, absorbed fluence is still less than 0.1J/cm^2

these temperature estimates should be taken with some caution, calculated values close to the melting temperature lead to the conclusion, that also in gold negative pressures/tensile stresses and thus spallation are responsible for the material decomposition at the ablation threshold.

2.2.3 Pressure waves and spallation

Spallation is the term commonly used to describe the dynamic fracture of a material due to the tensile forces induced by the reflection of a strong compression (shock) wave from the back surface of a sample [43]. The term front-surface laser spallation is the name for material ejection due to the laser-induced stresses [44, 43]. The processes of back-surface shock spallation and front-surface laser spallation are similar in their nature and can both be attributed to the reflection of a incoming compressive wave at a free surface [45, 46]. However, there are differences in the mechanisms of material fragmentation and ejection for these two cases. Laser heating strongly affects the mechanical stability of the front-surface region, which can affect dynamic fracture mechanisms compared with cold material spallation.

Several experiments show that in water gels and biological tissue ablation occurs, when the material is heated to a temperature lower than the boiling temperature (assumed to be 100°C) [47, 48, 49]. The laser pulses used in these experiments were of nanosecond pulse duration. The transient heating by a laser pulse induces a thermal expansion of the absorbing-liquid volume (rarefaction zone), which initially pushes the surrounding liquid medium. The formation of a compression and rarefaction zone, inside the heated volume, are responsible for the compressive and tensile stresses in the medium. The expansion that is considered to be an acoustic pulse in the medium has both compressive and tensile components. Whereas the thermal expansion directed into the medium generates positive stress (compression wave), the outward expansion directed to the free surface generates negative stress (rarefaction wave). If a liquid medium

is subjected to a high tensile stress[9], cavitation bubbles can be formed in the liquid, which can lead to the detachment of material and ablation.

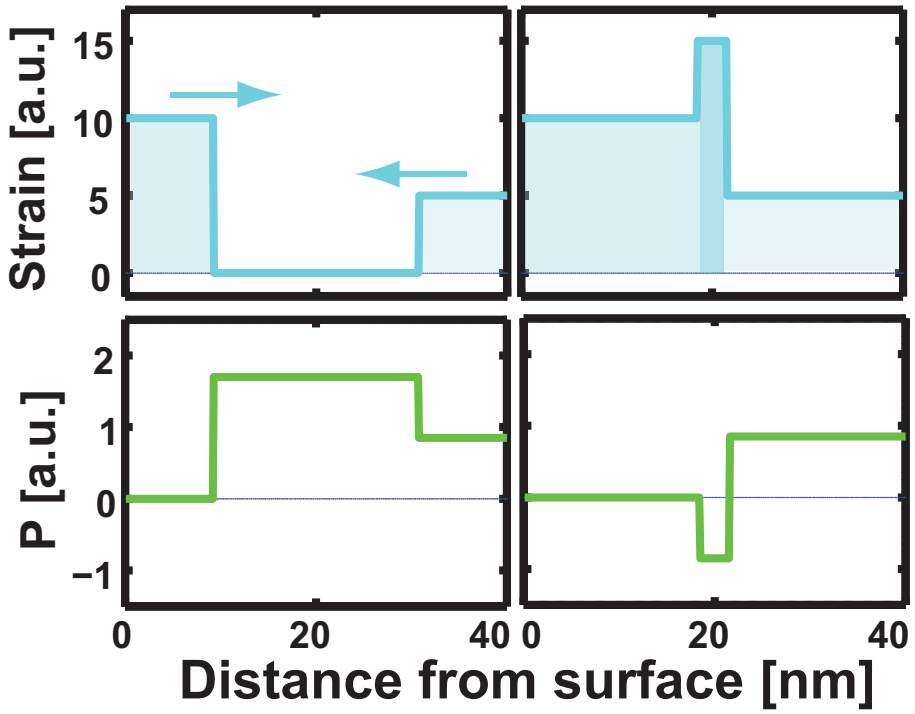

Figure 2.4: Strain and pressure waves in homogeneously heated film. Strain waves meet in the middle, which results in negative pressure developing from center of the film.

To gain some qualitative understanding of the spallation process due to expansion of an impulsively heated material a simple one-dimensional[10] acoustic model is applied. It should be emphasized that in the real situation, for fluences near the ablation threshold, the material response is not linear, because the induced density changes are large and the sound velocity is not a constant. Therefore, the considerations presented here should only be understood as an qualitative illustration of the expansion process. Two different situations will

[9] in order of 100MPa

[10] a 1-D description is justified because the typical lateral length scale (i.e. diameter of the focused laser beam; approx. 50 m) is much larger than the relevant length scale perpendicular to the sample surface given either by the film thickness or the absorption depth (approx. 100 nm).

be considered. The first one is a homogeneously heated (pressurized) layer; the second one assumes that the initial temperature (pressure) of the material decreases with depth[11].

Homogeneous heating

A single femtosecond laser pulse can produce a homogeneously heated layer of material in two ways. The first way occurs when the film thickness is less then the optical absorption depth, so that the radiation is absorbed almost homogeneously over the film depth. This is the case when the material is a film with a thickness that ranges up to approximately 20nm, which is a typical absorption lengths for metals at near infrared radiation wavelengths.
The second way is when the energy transport is fast compared to the expansion process (velocity of the heating wave is higher than local sound velocity [50]). In this case, one can have significantly thicker layers heated almost homogeneously, with the thickness of the heated layer up to a few hundreds of nanometers. Typical examples are gold with extremely fast hot electron transport [42] and aluminium with fast heat diffusion [50].

Two strain waves are launched in a homogeneously heated film (figure 2.4), one from the free surface and the other one from the other interface, i.e the back of the substrate, where the film is fixed. Both waves propagate through the material with the local sound velocity, which is assumed to be constant through the material that has not yet expanded. The waves will meet in the middle of the film. Material expansion and the amplitude of the strain waves depend on the initial temperature increase and it is determined by the volume that the material would occupy when the pressure is relaxed. When the two strain waves meet, the resulting strain is the sum of strains of the incoming waves, and in the overlap region, material overexpands and tensile stresses develop. If the stress exceeds the material tensile strength, the material can break. Since the

[11] in the case of linear absorption, temperature will decrease exponentially with increasing distance from the irradiated surface

maximum amplitude of the tensile stress is reached where the two waves meet spallation of a homogenously heated film should occur always in the middle of the film.

Inhomogeneous heating

Inhomogeneous heating can be expected in materials with the slow energy transport (like Nickel[44]). When the absorption is linear for example, the laser pulse is absorbed in the material and the deposited energy density decreases with depth exponentially (Beer-Lambert law). Due to the slow heat diffusion the temperature profile will essentially follow the absorption profile.
The behavior of picosecond acoustic waves in materials with a temperature profile decreasing from the surface has been discussed in the work by Thomsen *at al* [51]. Calculations for the case of gold with an exponential temperature profile (scale length given by the absorption depth) are presented in figure 2.5. 2.5. The initial temperature rise is just $\triangle T$ $\approx$30 K. As the material starts to expand, two compressive pressure waves are launched, one towards the free surface, the other one towards the bulk. The first one gets immediately reflected and changes sign manifesting itself as the negative part of the bipolar pressure wave propagating towards the bulk, following the positive pressure wave [52, 53]. As the wave travels, the negative part of the stress wave increases its amplitude until it becomes equal to the positive part. Even for such modest initial heating, the tensile stress calculated within this simple linear acoustic model exceeds the static tensile strength of the material (100MPa for Au [39]) giving additional indication that tensile stresses/negative pressures may play an important role for the material decomposition and ablation close to the threshold.

As for the case of an homogenously heated layer some conclusions on the depth where spallation occurs can be also drawn for a decreasing temperature profile. As can be seen in figure 2.5 the amplitude of the tensile stress increases with time (and depth) until it reaches the same absolute value as the compressive leading edge of the acoustic pulse. If one assumes that spallation occurs for a well

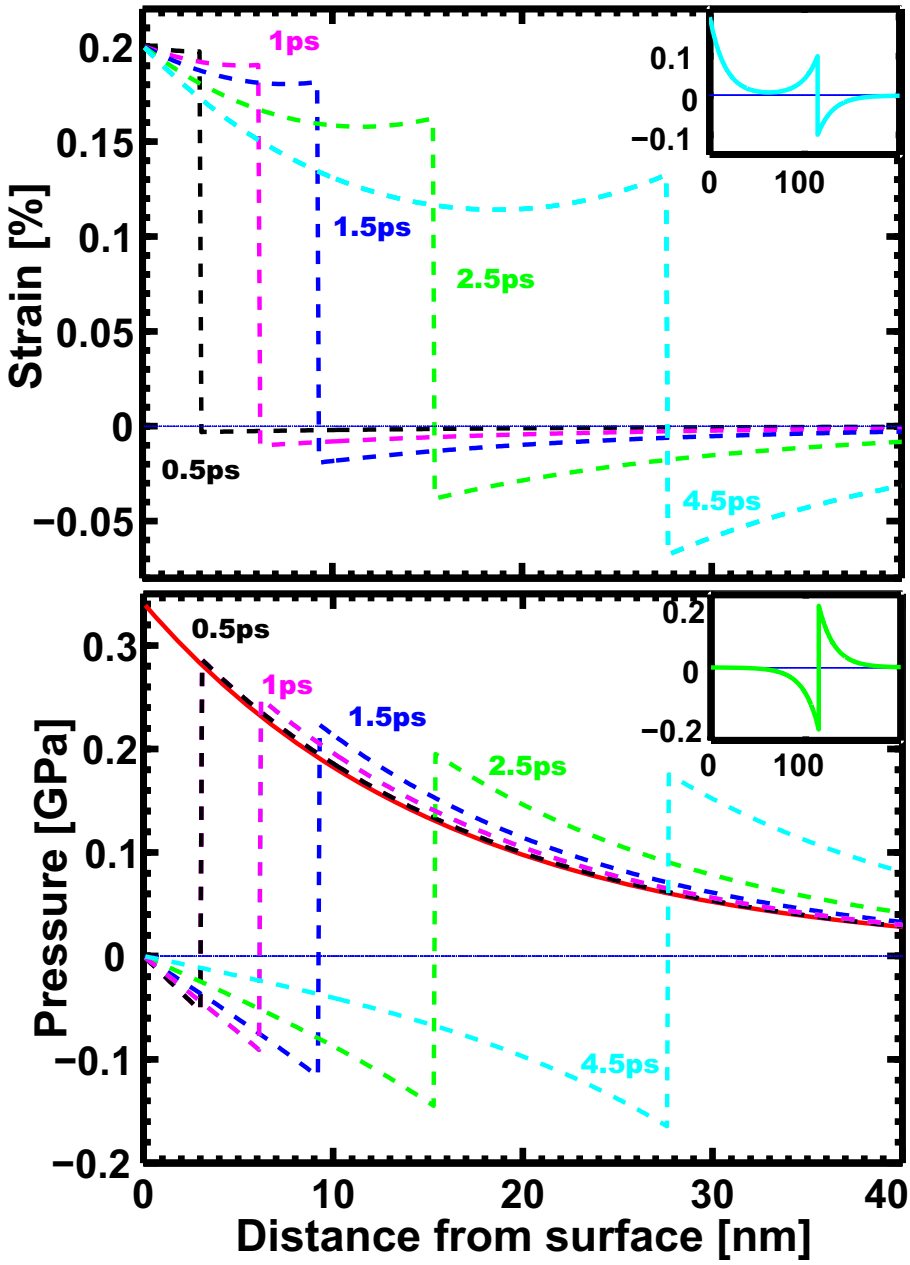

Figure 2.5: Strain and pressure profiles in a inhomogeneously heated material. Initial temperature decreases exponentially with distance from the irradiated surface. Initial heating at the surface is just 30K. The red line represents initial pressure profile and the five other profiles show the evolution of strain and pressure at different moments in time in their respective graphs. Insets show strain and pressure wave after 18.5ps, and amplitude of propagating wave does not change any more with time. Exact scale is derived from properties od gold and is meant to illustrate that even for modest heating significant stresses are generated in material.However, they are just an illustration purpose only, since gold has in fact extremely rapid heat diffusion.

defined threshold value of the tensile stress (the dynamic tensile strength) it is expected that with increasing fluence this value is reached closer to the surface. Moreover, since the (dynamic) tensile strength of a material may decrease with increasing temperature void nucleation and spallation must not necessarily occur at the depth where the tensile stress is maximum. Such behavior has been recently also observed in MD-simulations[54, 55].

Chapter 3

Ablation by femtosecond optical radiation

3.1 Experimental setup

To study ultrafast phenomena in the femtosecond to picosecond time range the so-called pump-probe technique is usually applied. An ultrashort optical pulse is split and one portion is used to excite the sample under investigation while the other is delayed with respect to the first and used to probe the material. The main objective of my work was to measure the small movements of the surfaces after irradiation close to the ablation threshold.

This section contains details on the experimental setup, the laser system and the data processing technique. The experimental setup consists of a time and space resolved optical interferometer, and its optical design and properties are explained in section 3.1.2. The laser system produces 50 femtosecond light pulses with a 1 kHz repetition rate, and details on how this system is utilized are presented here. Finally, the data processing section contains an explanation of the Fourier processing technique and its modifications for the analysis of the measured interferograms.

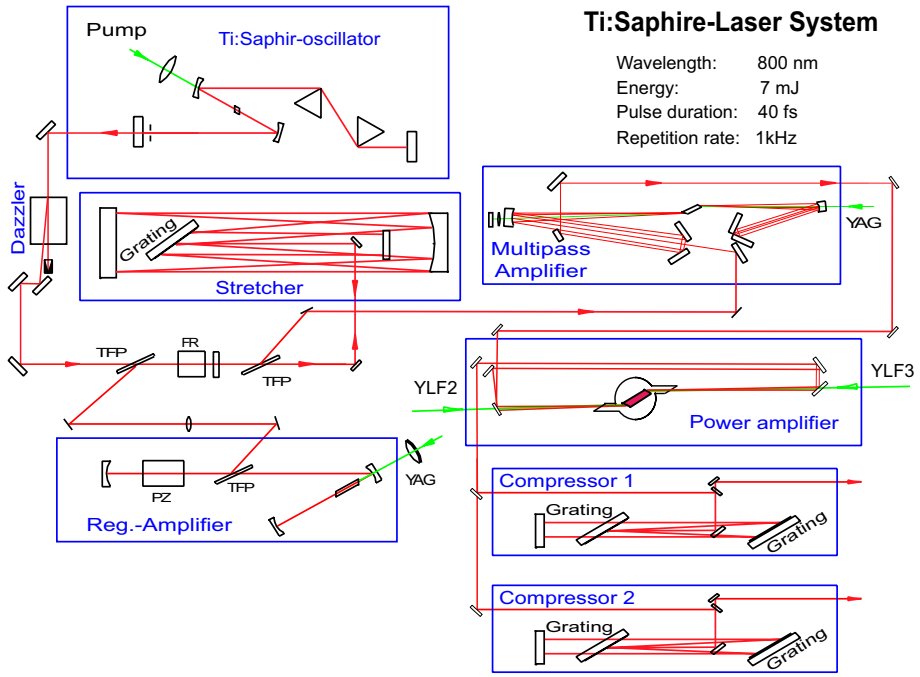

Figure 3.1: Laser System scheme

3.1.1 Kilohertz Laser System

The femtosecond laser pulses are generated in a Titanium:Sapphire (Ti:Sa) system, using the Chirped Pulse Amplification (CPA) technique [56, 57, 58, 59]. A scheme of the system is presented in Figure 3.1. The system consists of a femtosecond oscillator, a "stretcher", three amplification stages and a "compressor".

The mode locked Ti:Sa laser oscillator is pumped with a commercial CW Nd:VO_3 laser (532 nm wavelength and average power 3.6 W) and delivers 100 mW average power in pulses of 20fs duration. The repetition rate of the laser oscillator is 82MHz.

The femtosecond pulses from the oscillator, before being amplified, enter an acousto-optic pulse-shaper, a so-called Dazzler [60], which manipulates the phase of the pulses, usually to minimize the pulse duration after amplification.

In order to effectively amplify ultrashort pulses, the radiation intensity in the amplifying media must be kept as low as possible to avoid damage and nonlinear optical effects. Therefore, before amplification, the laser pulses are stretched in the so-called "stretcher" with positive GVD (Group Velocity Dispersion), meaning that the short wavelength components have a shorter path through the Stretcher than the long ones. The pulse duration is increased by almost four orders of magnitude (from 20 fs to 170 ps) and, consequently, the peak power is decreased by the same factor. The stretched pulses can be amplified by a factor of 10^6 without damaging the amplifying media (Ti:Sa crystal).

After the stretching, the pulses are switched into the regenerative amplifier, where, after 20 round trips, they are amplified to an energy of 600μJ and then sent to the first multi-pass amplification stage. This stage consists of four passes through the Ti:Sa crystal and here the pulse energy is amplified to 2.2mJ.
In the final two-pass amplification stage the pulse is further amplified, resulting in pulse energy of 7 mJ. All amplification stages are pumped with three Nd: YLF- Lasers, each with average pumping power of approximately 10 W. To decrease the effects of the thermal lens from thermal loading, the amplifying media (i.e. Ti:Sa crystal) is cooled using a Joule-Thompson cooler. The temperature of this stage is kept at 120 K. To avoid condensation on the crystal surface, this stage is kept under the vacuum.

Pulses amplified in this way have high energy, but pulse length is almost 200 ps. Therefore, the amplified pulses, are sent through the Compressor, which has negative dispersion that compensates the positive dispersion from the Stretcher and dispersion induced by some optical components. In this way the pulse is compressed to approximately 50 fs. After compression, the maximum energy is 5 mJ.

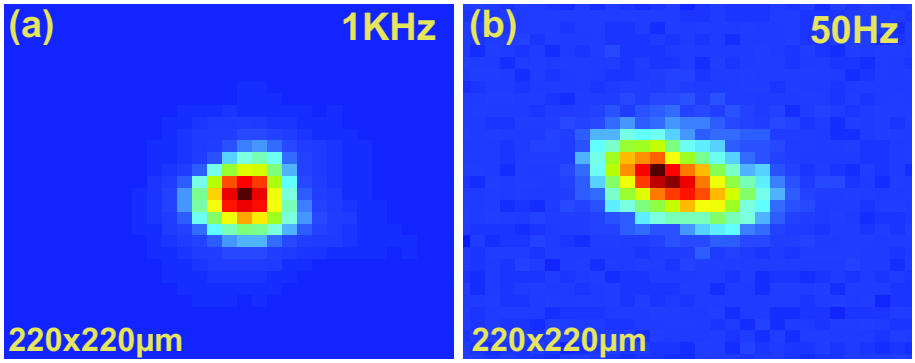

Figure 3.2: Images of focal spot. (a) 1kHz repetition rate. (b) Repetition rate reduced to 50Hz, by inserting optical chopper between final amplification stage and the compressor. Because of different thermal loading on the diffraction grating inside the compressor, laser beam shows increased astigmatism, and the maximal intensity is reduced, due to the increased focus size.

Single pulse selection

The pump and probe experiments discussed in this thesis are of a destructive type, which means that the material is permanently modified after irradiation with a single laser pulse (ablation crater is formed). For each measurement, the sample is moved to irradiate the fresh spot. Therefore, in the experiment, only a single laser pulse irradiates the surface, and produces the illumination for the probe. Therefore, it is necessary to select single pulses from the kHz train of amplified pulses.

An upgrade of the laser, into a system with an average power of 5W, made on-line changing of the repetition rate within the laser system very difficult. Indeed, because of the thermal lens effect in the Ti:Sa crystal and thermal loading of the compressor gratings, the final compressed laser pulses have different shapes at different repetition rates, even if all other settings of the system are equal. To illustrate this, igure 3.2 shows the focus shape at repetition rates of 1 kHz (a) and 50 Hz (b). The repetition rate is changed by an optical chopper, placed in front of the compressor and after the last amplification stage. The oscillator and amplifiers are operated with a 1KHz repetition rate. This demonstrates the effect of different thermal loading in the compressor for two repetition rates

(1KHz vs. 50Hz) on the final focused pump beam on the sample.
To avoid these effects single pulse selection is done using a combination of an optical chopper placed after the compressor and an electro-mechanical shutter. Details can be found in Appendix A.

3.1.2 Setup for time-resolved Michelson interferometry

In order to study the behavior of the materials near the ablation threshold, it is instructive to observe the surface deformations of materials irradiated with different laser fluences.
Time- and space-resolved optical interferometry combines the pump-probe technique with optical interference microscopy. This technique can be realized in different experimental configurations. Some of the recent applications of the conventional two-beam interferometry (such as Michelson or Mach-Zehnder) include the dynamical studies of the laser ablation of polymer films irradiated by nanosecond pulses [61], and the propagation of the ionization front in He-gas, induced by ultrafast ionization [62]. The recently developed spectral interferometry was used to investigate the expansion dynamics of fs-laser- produced plasma [63], fs-laser-driven shocks in metals [64] and the dynamics of the electron gas in the bulk of laser-irradiated dielectrics [65].

Temporal resolution, lateral spatial resolution and phase sensitivity determine the performance of a time- and space-resolved interferometer. The duration of the probe pulse on the sample determines the temporal resolution. Properties of the imaging optics, adjustment of the interferometer, interferogram recording and mathematical algorithms for processing the interferograms determine lateral spatial resolution and phase sensitivity.

Temnov at al [24, 25] designed a setup for optical Michelson interferometry with a Linnik imaging configuration [66]. Using this setup one can measure both very small phase shifts ($< \lambda/200$) and amplitude changes ($\sim$ 1 percent) with femtosecond time resolution ($\sim$ 100 fs) and 2D-lateral spatial resolution of

about 1 μm [24]. A 2D-Fourier-transform algorithm is used to reconstruct the amplitude and phase of the interference fringes [67, 68].

Figure 3.3(a) shows a schematic of the experimental setup for ultrafast Michelson interferometry with a Linnik imaging configuration. A π-polarized pump pulse (Ti:Sa, τ = 50 fs, λ = 800 nm) at an angle of incidence of approximately 35° excites the surface of the sample. A weak, frequency doubled probe pulse illuminates the excited surface area. The probe pulse irradiates the sample surface at normal incidence and passes through the objective lens of a high-resolution microscope objective (20X, NA=0.3) which has a working distance of 17 mm. The frequency doubled probe pulse has a significantly longer duration than the 50fs of the fundamental because it is generated in a thick crystal ($\sim 1mm$) and it is passing through the thick microscope objective. Using the ultrafast phase transition in GaAs (accompanied with an increase in reflectivity [26]), the pulse duration was estimated to be less than 500fs. The pulse lengthening is not very important, since the processes studied in this thesis are happening on picosecond and nanosecond timescales.
The probe pulses are spatially filtered before entering the interferometer, in order to achieve a spatially homogeneous surface illumination. They illuminate a large surface area in the object plane, because they are strongly divergent at the microscope objective (a parallel beam would be focused to a small spot of approximately 2 μm diameter). This is accomplished by placing a lens in front of the interferometer. Figure 3.3(b) sketches the formation of the interferogram: in the image plane on a CCD-camera, the reflected probe light (the object beam, which is visualized as a cone of rays within an angle β) interferes with a reference beam which passes through an identical reference arm of the interferometer. Adjustment of the reference mirror changes the angle between the wavefronts of the object and the reference beam. The tilt is marked by the angle α in figure 3.3(b) and determines the orientation and spacing between the interference fringes. The fringes are adjusted so that they are vertical on the

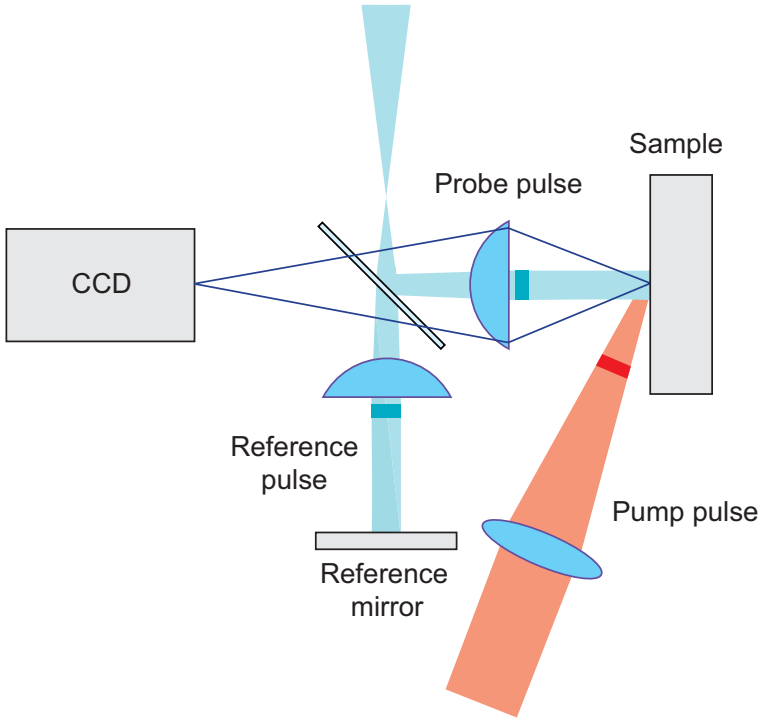

(a) Setup for ultrafast Michelson interferometry with Linnik imaging configuration.

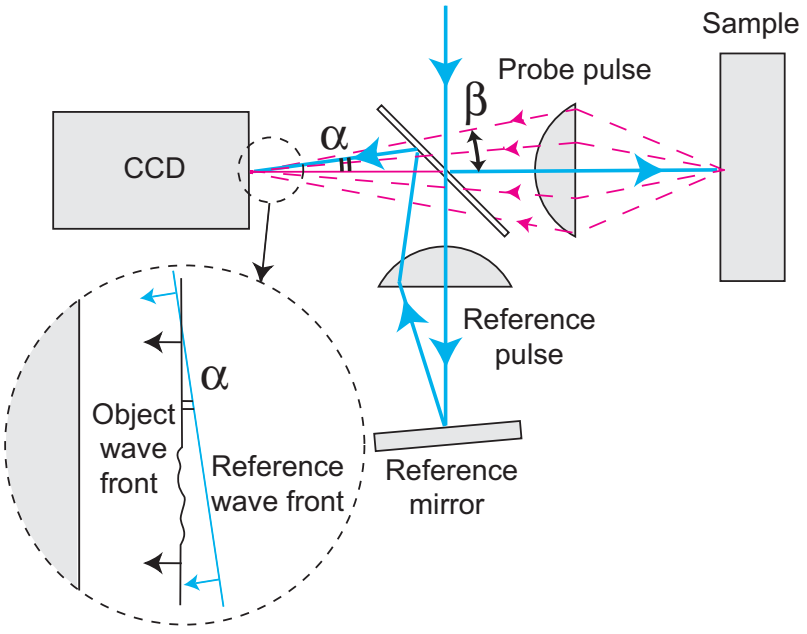

(b) Formation of an interferogram in a Linnik microinterferometer.

Figure 3.3: Scheme of the interferometer, reprinted from Temnov PhD thesis[25], with permission of the author.

CCD chip, and have almost equidistant spacing along the width of the CCD. More detailed explanation of technique is given in the original work by Temnov [25].

An optical delay line can change the pump- probe delay up to 1.8 ns, with a minimal step size of 6.7 fs. The optical delay line consists of a gold coated retro- reflector mounted on a translation stage, which, in turn, is powered by a computer controlled stepper motor. Additional pump- probe delay is provided by a "manual" optical delay line, which consists of two mirrors on a rail that can be adjusted by hand, with an accuracy of ∼1mm (approximately 3 ps). The usual procedure in the experiment is to find zero delay between the pump and probe pulses (usually ultrafast reflectivity change due to the phase transition on Si or GaAs[26]), investigate the early delay times (up to 1.8 ns) with the high resolution, and then switch to later delay times. The drawback is that once the "manual" stage is used the exact (down to 500 fs) time overlap is lost, but for ablation studies this is not of great importance (tens of picoseconds to tens of nanoseconds phenomena).

3.1.3 Intererogram processing

The technique for phase retrieval from the images produced in an interferometry experiment is described by Zakharov *at al* [69]. This tool can be extended to the time-resolved experiment simply by including the transient interferograms [70, 71]. The technique for data processing is described in the work of Temnov *at al* [70] in detail and here it is discussed only briefly.

An interferogram is a recording of the spatial intensity distribution $I(x, y)$ of the probe beam on the CCD chip ((x, y) are the coordinates of a single pixel on the CCD). This measured intensity distribution is the result of the interference of the object and the reference probe beams. The electric field of these two

beams is defined as:

$$\begin{aligned} E_{obj}(x,y) &= \tilde{r}(x,y)E_1(x,y)\exp(i\phi_1(x,y))\,, \\ E_{ref}(x,y) &= E_2(x,y)\exp(i\phi_2(x,y))\,. \end{aligned} \tag{3.1}$$

The complex reflection coefficient $\tilde{r}(x,y)$ is defined for the object beam, and its value will change for different images (initial, transient and final). The complex reflectivity describes amplitude changes (reflectivity) as well as phase changes, due to changes of the optical constants of the material.

$$\tilde{r}(x,y) = r(x,y)\exp(i\psi(x,y))\,, \tag{3.2}$$

The reference beam does not change for one set of measurements, so in the equation for the electric field a variable reflection coefficient is left out. For a particular time delay between pump and probe, three interferograms make one set of measurements. "Initial" is the interferogram of the sample surface before excitation. "Transient" is the interferogram of the same surface spot after irradiation, for the investigated time delay between pump and probe pulse. "Final" is the interferogram of the surface couple of seconds after the pump pulse, representing the final morphology of the surface. The three interferograms have intensity which can be represented as follows:

$$\begin{aligned} I_i = r_i^2E_1^2 + E_2^2 + 4r_iE_1E_2\cos(\phi_1 - \phi_2 + \psi_i)\,, \\ i \in \{\text{Initial}, \text{Transient}, \text{Final}\}\,. \end{aligned} \tag{3.3}$$

Indices x and y are omitted in this formula, but all variables are a function of coordinate (x,y).

By tilting the reference wavefront, the fringes on the experimental interferogram are adjusted to be almost equally spaced, parallel and aligned with one axis of the CCD chip (designated the y axis). If the reference and object wavefronts have the same curvature on the CCD chip, the phase of the interference

fringes has a linear dependance:

$$\phi_1(x,y) - \phi_2(x,y) \quad \simeq \quad 2\pi f_0 x + \varphi_i(x,y)\,. \tag{3.4}$$

f_0, is the spatial frequency of the interference fringes, called the carrier frequency, and it is proportional to the angle between reference and object wavefronts (α in Figure 3.3(b)). The term $\varphi_i(x,y)$ contains changes of the phase due to geometrical changes of the sample, as well as deviations of the wavefront from a plane wave.

The Fourier transform method [72, 73] is used to extract phase and reflectivity information from the interferograms. The fringe pattern can be expressed mathematically (as mentioned before) as follows:

$$g(x,y) = a(x,y) + b(x,y)\cos(2\pi f_0 x + \Psi(x,y))\,, \tag{3.5}$$

Functions $a(x,y)$ and $b(x,y)$ describe the background illumination and the fringe contrast, f_0 is the carrier frequency, and $\Psi(x,y) = \psi(x,y) + \varphi(x,y)$ is the complete phase of the interferogram, including both the geometrical phase and the phase of complex reflectivity.
The extracted phase shift from the initial to transient (and initial to final) interferogram and the reflectivity changes are relative changes in phase and amplitude of the object wave with respect to the unexcited surface, and they are the quantities whose evolution we want to follow in time.

$$\Delta\Psi_{tr}(x,y) \quad = \quad \Psi_{tr}(x,y) - \Psi_{in}(x,y) \qquad \text{(transient phase shift)}\,, \tag{3.6}$$

$$\Delta r_{tr}(x,y) \quad = \quad r_{tr}(x,y)/r_{in}(x,y) \qquad \text{(transient amplitude change)}\,, \tag{3.7}$$

A proper retreival algorithm has to fulfill some conditions if one wants to obtain the phase without any ambiguity:

- The largest gradient of the object phase has to be considerably smaller than the spatial carrier phase frequency ($\frac{\partial \varphi}{\partial x} \ll 2\pi f_0$);
- Background illumination and the fringe contrast functions are both slowly varying compared with the carrier frequency.
- The carrier frequency f_0 has to be less than half of the sampling frequency (Nyquist condition). Typically, fringes are set with 10 pixel spacing. This gives reasonable separation of DC (associated with background illumination) and AC (carrier frequency) components and is not too low to introduce significant sampling errors.

The function $g(x, y)$ can be rewritten in an exponential form:

$$g(x, y) = a(x, y) + c(x, y)e^{2\pi i f_0 x} + c^*(x, y)e^{-2\pi i f_0 x}\,, \tag{3.8}$$

where the new coefficient is defined as $c(x, y) = \frac{1}{2}b(x, y)e^{i\Psi(x,y)}$. The Fourier transform of the intensity function of the fringe pattern $g(x, y)$ gives the spatial frequency spectra:

$$G(f_x) = A(f_x) + C(f_x - f_0) + C^*(f_x + f_0)\,, \tag{3.9}$$

f_x denotes the spatial frequency in x direction. If the functions describing background illumination $a(x, y)$, fringe contrast $b(x, y)$ and phase $\Psi(x, y)$ are slowly varying over x compared to the term $\cos(2\pi f_0 x)$, then the Fourier spectra are separated in three peaks (one DC and two AC peaks, see figure 3.4(a)). One AC peak is isolated by multiplying the spectra with a windowing function (Hamming window), and shifted by f_0 to origin. This removes the carrier frequency and gives $C(f_x)$. Inverse Fourier transform of $C(f_x)$ gives the complex function $c(x, y)$. The phase is defined as:

$$\Psi(x, y) = \arctan \frac{Im[c(x, y)]}{Re[c(x, y)]}\,, \tag{3.10}$$

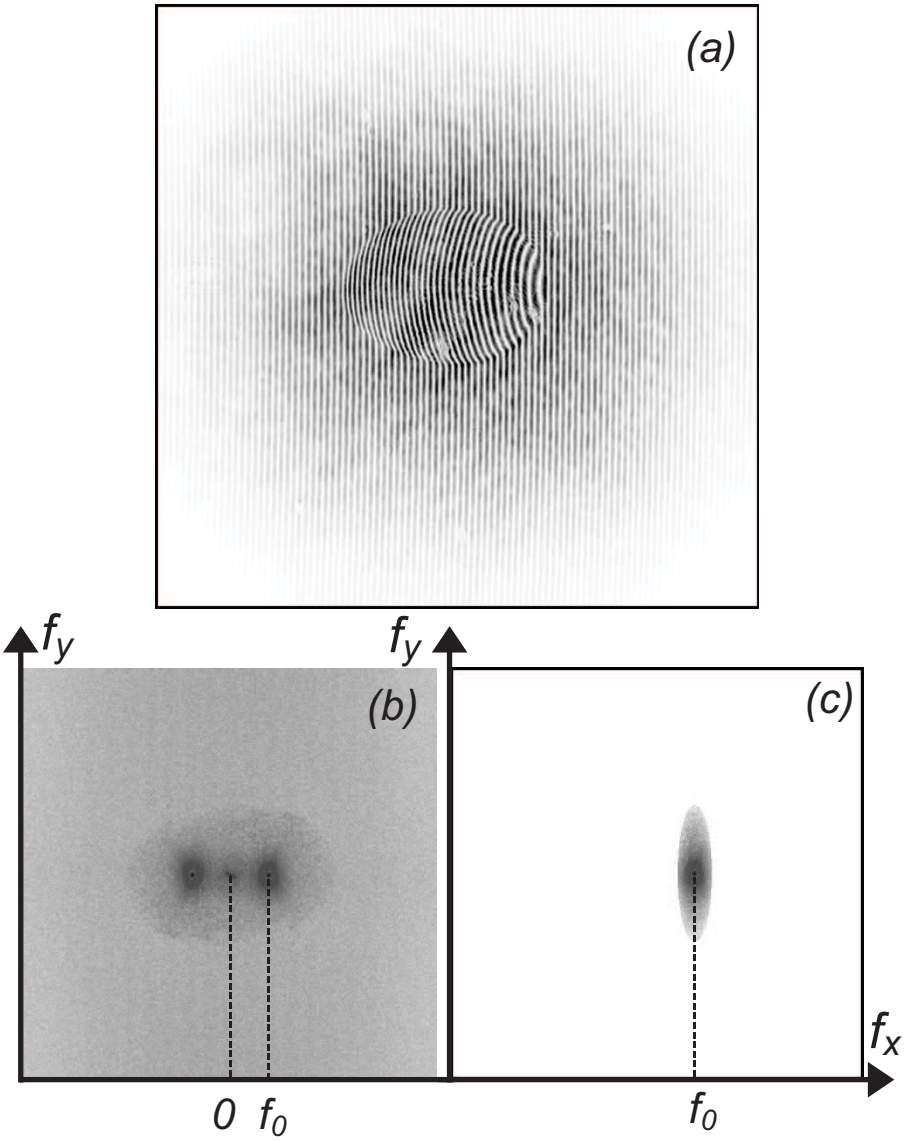

Figure 3.4: (a) Transient interferogram of 125 nm thick gold film 2.3ns after irradiation with the laser pulse (1.2J/cm^2 peak fluence). Interferogram is multiplied with windowing function to reduce boundary effects. Image (b) is Fourier transform of the interferogram on image (a) and image (c) is the isolated AC peak, at the carrier frequency f_0, which is the spatial frequency of interference fringes

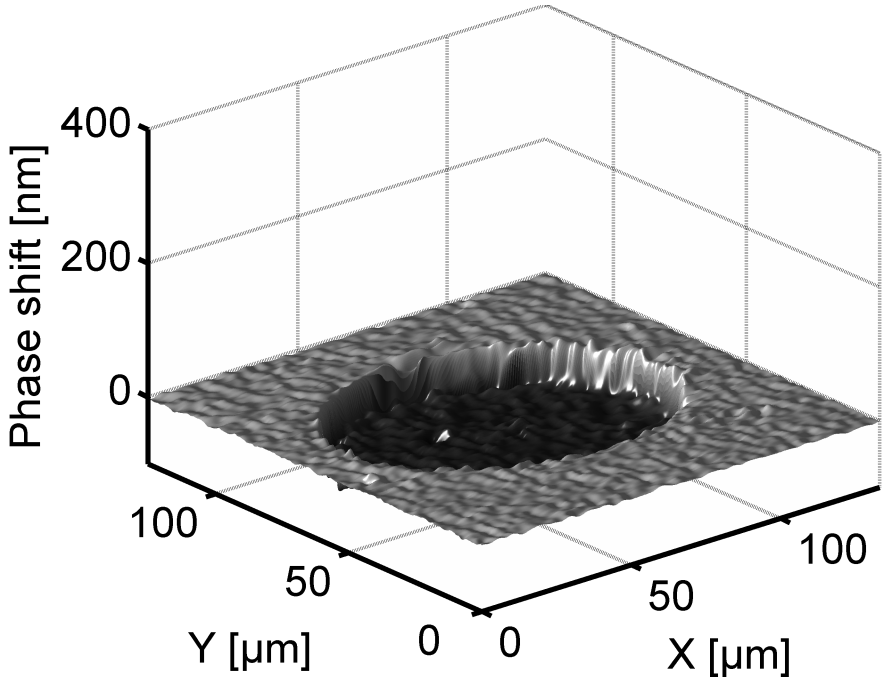

Figure 3.5: Final phase map of ablation crater in 3D representation.

As an example of reconstructed phase maps, the transient irradiated spot on a gold film and the corresponding final crater are presented in Figures 3.6 and 3.5, respectively. Interferograms are made on a 125nm thick gold film, with a fluence of 1.2J/cm^2. The delay time between pump and probe was 1.6ns.

The experimentally recorded interferogram represents an rectangularly windowed part of the complete interference pattern. Windowing of a simple waveform, like $\cos(\omega t)$, causes its Fourier transform to have non-zero values (commonly called leakage) at frequencies other than ω. Leakage increases the overlap of frequency components belonging to the background illumination (DC peak) and fringes (AC peak).

The level of leaked frequency components depends on the function used for waveform windowing. A proper selection of the windowing functions can reduce the level of leaked frequencies by several orders of magnitude [72, 74], compared with simple rectangular windowing imposed by physical limitations of the CCD

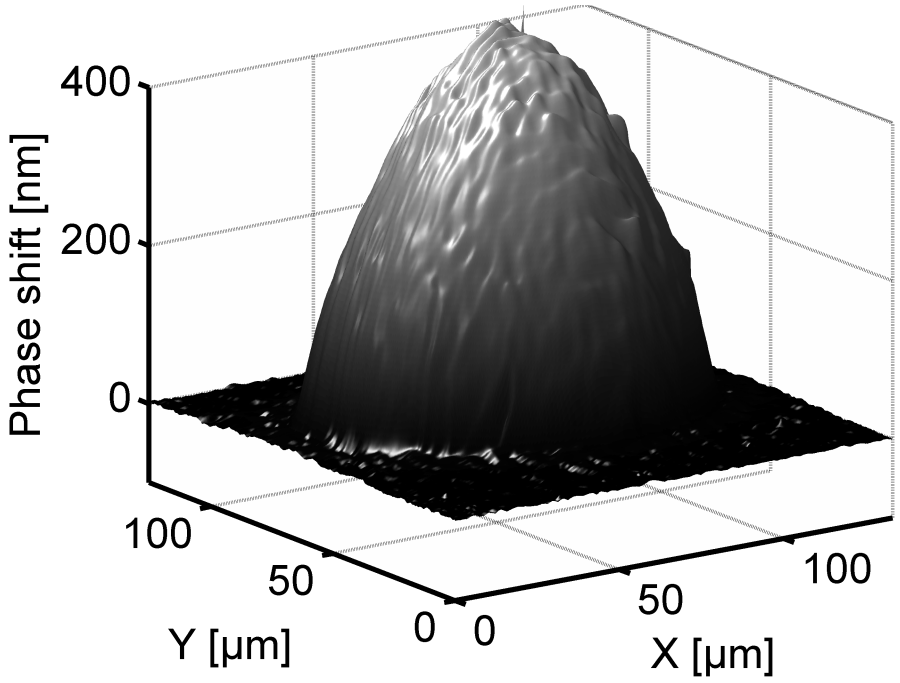

Figure 3.6: Transient phase map of surface expansion on 125nm thick Gold film, 1.6ns after irradiation with laser pulse (1.2J/cm^2 peak fluence).

chip.

A Hamming window is used here [75], as it provides a good balance between the reduction of leaked components and the loss of information due to windowing. An example of a windowed interferogram can be seen in figure 3.4(a).

The microscope objective has a finite aperture, and only a limited cone of rays forms an image on the camera (see figure 3.3(a)). The maximal frequency that should appear in the Fourier spectra is determined as:

$$f_{max} = NA/\lambda = (1.1\mu\text{m})^{-1}\,, \tag{3.11}$$

for NA=0.3 being the numerical aperture of the objective and λ the probe wavelength. The frequency components of the two AC peaks are localized in circles with radius f_{max} and centered at $\pm f_0$(figure 3.4(b)).

Multiplying the Fourier spectra by a Hamming window centered around f_0 isolates the AC peak (figure 3.4(c)). The Hamming window has a width in y direction which is equal to the maximal detectable frequency f_{max}. In x direction it is four times narrower in order to allow for a good separation from the DC peak. Maximum frequency in our case is f_{max}=(1.1 μm)$^{-1}$, and this gives:

$$\Delta x = 4.0\ \mu\text{m}\,,\ \Delta y = 1.1\ \mu\text{m} \tag{3.12}$$

The pump laser pulse impinges on the surface of the sample with an angle of 35° and the irradiated spot has an elliptical shape. The pulse has an approximately gaussian spatial intensity profile and the incident fluence is mapped on the surface, with the amplitude decreasing from the center of the irradiated spot. The contours of constant fluence are ellipses with the same center and eccentricity. These two parameters are defined from the crater shape, as the crater boundary follows the contour of the constant threshold fluence. As mentioned above, ablation has a well defined threshold with respect to the fluence and the crater has a sharp boundary that coincides with the place on the sample where the fluence reaches threshold value.
The accuracy of the retrieved phase is estimated from the regions of the phase map corresponding to the nonirradiated part of the sample surface. Its value is typically $\sigma = \text{rms}\{\Delta\Psi(x,y)\} \simeq \pi/100$. Averaging the phase shift and reflectivity along contours of constant fluence (ellipses), the error typically decreases [25] by an order of magnitude.

Cutout technique

The semiconductor samples used in the first interferometry experiments by Temnov *at al* [24] had a surface with a very high quality and they are good candidates for the elliptical averaging technique (along contours of constant fluence) mentioned above. The metal films, that were available for the experiments discussed

in this thesis, exhibit a lower quality surface, with a number of irregularities[1].

These surface irregularities produce irregularities in the ablation process for example by changing locally hte absorption and the ablation threshold. This induces discontinuties and ambiguities in the retrieved phase maps because the phase gradients around these irregularities often exceed the carrier frequency f0 and, consequently, the conditions for applying the Fourier transform method are not fulfilled. Therefore, the phase can not be uniquely determined and errors usually occur. In the work by Temnov [25], the author managed to solve the problem of the so-called phase-dislocations caused by the steep ablation front close to threshold by the technique of *Fourier unwrapping*. However, this technique requires a *priori* knowledge of position of the phase dislocations. In the case of semiconductors these dislocations were caused by the high slope of the expanding surface near the ablation threshold in the later stages of the expansion. They are positioned on the ellipse defined by the future ablation crater. In the case of metals, equivalent phase dislocations exist, which will be discussed in more detail later in this section, but there are also phase dislocations associated with the above mentioned imperfections. These are randomly distributed on the sample, which makes Fourier unwrapping impractical.

Another aspect of the same problem with ablation on metals is the relatively large maximum surface excursion, as compared to GaAs (approximately by a factor of 2, depending on the metal). For large surface deformations (1-5 μm), interference lines change their spacing up to a factor of two, due to the high slope of the deformed surface in the direction perpendicular to the fringes, mainly in the region near the ablation threshold.

Interference fringe spacing is typically set to $\Delta x \simeq 10$ pixel. For a large surface excursions fringe spacing changes. On the right side of the plume it has

[1]There are generally two different kind of surface irregularities. One is caused by contamination of the substrate prior to deposition process, leading to elevated surface at the specific point, after deposition of the metal film. The other one is harder to trace, and is connected with deposited film thickness. Namely, for thicker metal films (50nm and more) there is general tendency of formation of points that are elevated with the respect to the rest of the surface, which have no origin in surface contamination.

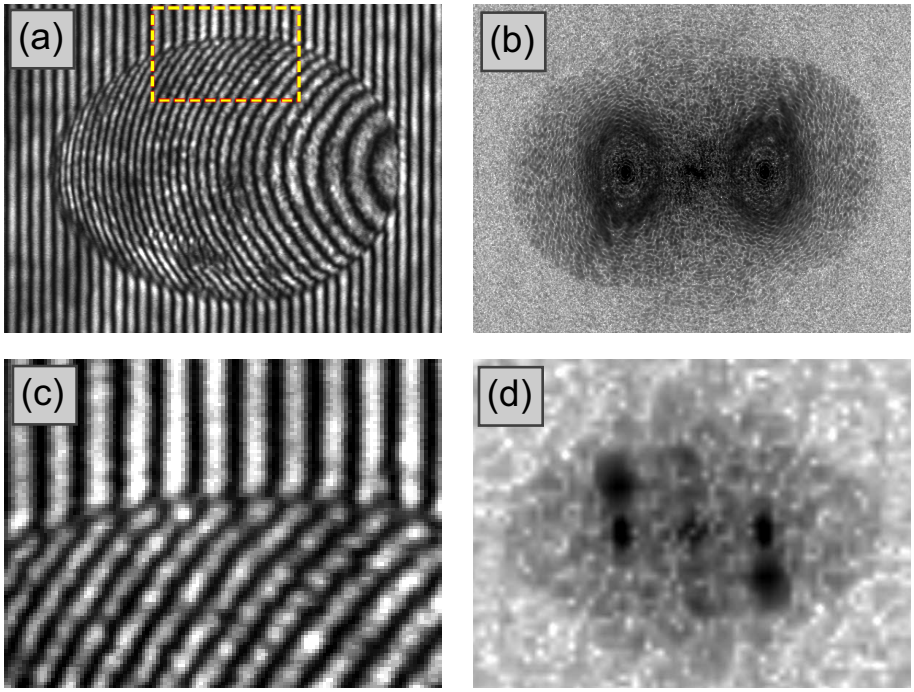

Figure 3.7: Transient interferogram of a gold surface 6.1 ns after irradiation with femtosecond laser pulse is depicted at image (a). Spacing of fringes changes from one side to the other, and this indicates change of carrier frequency at different positions. In interferogram Fourier transform this is visible as wide ring around AC peak. Cutout of interferogram, is selected so that fringes have more equal spacing is presented on image (c) and the frequency components in its Fourier transform are more localized around AC peaks.

a lower frequency ($\Delta x_{low} \simeq 20$ pixel); on left side it is higher ($\Delta x_{high} \simeq 5$ pixel). In the Fourier spectra, this appears as components of the AC peak, which are in ($-f_0/2$, $f_0/2$) range around the DC peak. This enhances the already mentioned problems of separating the AC-components from the DC peak, even more.

By selecting only a small area, such as in figure 3.7(a), two things can be accomplished. First, the spatial frequency of the interference fringes remains constant across the "cutout" image. This relates to the AC components which are more localized (figure 3.7(b) vs 3.7(d)), and the overlap with the DC peak is reduced.

Second, by reducing the size of the observed area, the probability that irregular-

ities will appear on this portion of the images is reduced. The retrieved phase is unwrapped along vertical lines, and the phase profile is taken along the short ellipse axis. This axis is usually oriented with a small angle with respect to the vertical axis (see figure 3.8(d) as an example). Defects induced by vertical unwrapping can be detected and corrected in most cases.

Also, since the cut images have an area approximately 100 times smaller than the original ones (100×100 pix, and original ones 1000×1000 pix), there is a significant boost in computational speed.

Problems with phase retrieval near threshold fluence for longer delays

The fact that the ablation craters are typically almost flat makes it possible to use the value of half depth as a criterion to locate the crater boundary and its contour. The crater contour can be determined using this approach. Fitting an ellipse using these points gives us the parameters of the laser pulse which irradiated a particular spot (see Figure 3.8).

From the final phase maps (figures 3.8 (a) Au and (b) GaAs) the crater boundary points are detected, and the contour of ablation threshold fluence is determined by fitting the ellipse to these points (figures 3.8 (c) and (d)). However, the crater boundary deviates from the perfect ellipse. These deviations are presented in figure 3.9 for craters on Au and GaAs, already presented in the previous image. The deviation is normalized to the local ellipse radius, and presented in percent of its value. The boundary of the crater on GaAs deviates from the ideal case much less than that on gold ($\sigma_{GaAs} \approx 0.7\%$ vs. $\sigma_{Au} \approx 1.8\%$).

For an ideal material irradiated with a circular laser beam at an oblique angle of incidence, the ablation crater would be a perfect ellipse whose eccentricity is determined by the angle of incidence. The observed random deviations from the ellipse can be explained by local changes of absorption induced by surface irregularities. Increasing or decreasing the absorption locally will shift the

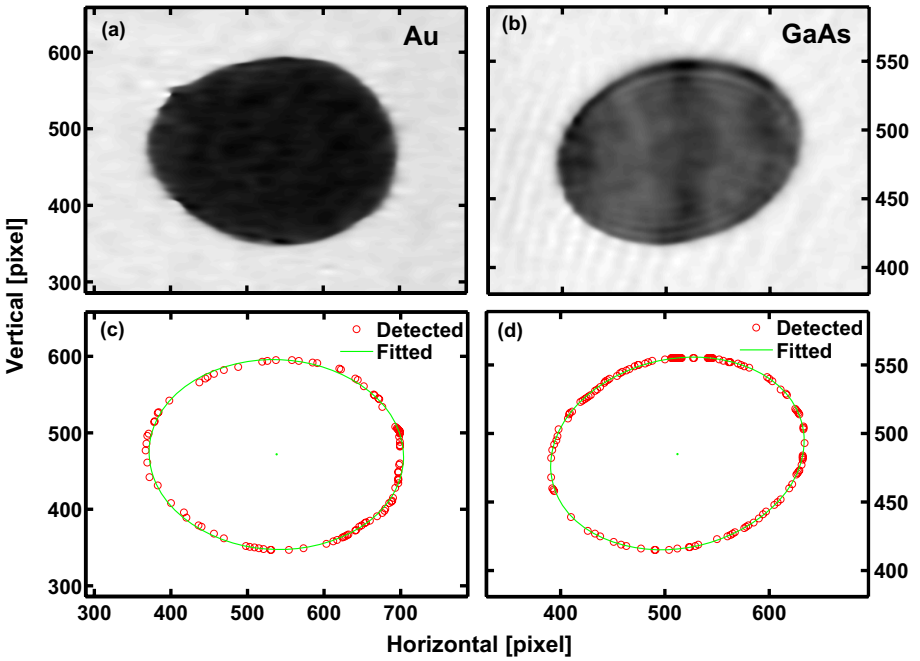

Figure 3.8: Phase maps of final craters for Au (a) and GaAs (b). Points of crater boundary *detected* by threshold algorithm are represented as red circles in figures (c) and (d). They are *fitted* to ellipse (green line), which determines contour of constant fluence F_{th}

crater boundary further and closer to the crater center, respectively. Absorption change due to the random roughness of the sample can be in the range of a couple of percent [76]. The fluence of the laser pulse with Gaussian intensity distribution scales as $F \sim F_0 \cdot e^{-\frac{r^2}{r_0^2}}$, and when one wants to determine fluence from crater radius, the relative error is approximately $\frac{\Delta F}{F_0} \sim \frac{\Delta r}{r_0}$ (assuming craters with sizes in FWHM range). Therefore, the observed relative error of a few percent in the crater radius can be explained by changes in local absorption induced by sample roughness and imperfections.

A partial solution to this problem is to recalculate the local fluence starting from the local threshold point. This provides correction for beam deviations from the perfect ellipse and for changes in the local ablation threshold that are relatively large in scale (with respect to the boundary width). The problems remain for fluctuations in the threshold for small irregularities, and this, in general, can

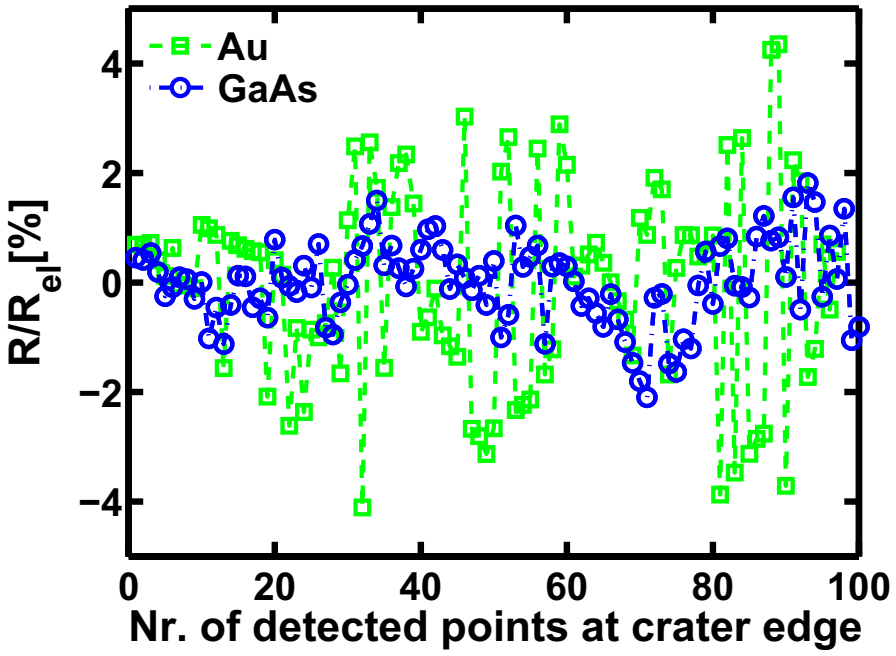

Figure 3.9: Deviation of detected points from fitted ellipse, for previous images (Au and GaAs). Distance is normalized to the radius of ellipse at that point.

not be corrected.

Material excited above threshold expands continuously, whereas material excited below the threshold returns back. This results in an increasing steepness of the surface in the threshold region. Figure 3.10 shows the profiles of the ablating plume in y direction for different delay times. The horizontal coordinate is the relative fluence (normalized to the ablation threshold fluence) that is mapped onto the sample surface, and the vertical axis denotes vertical expansion of the plume (blue line) and the final crater (green line). The increase of the surface gradient is apparent in the region around the threshold.

The limitation of the Fourier method used here is that for a given optical resolution phase gradients have to take small values (phase gradient has to be less than $\pi/\Delta y$, Δy being the optical resolution). In y direction the resolution is 1.1μm and one pixel shows 256 nm on the sample surface, which results in 5 pixel optical resolution. For late delay times, this limit is approached, and the

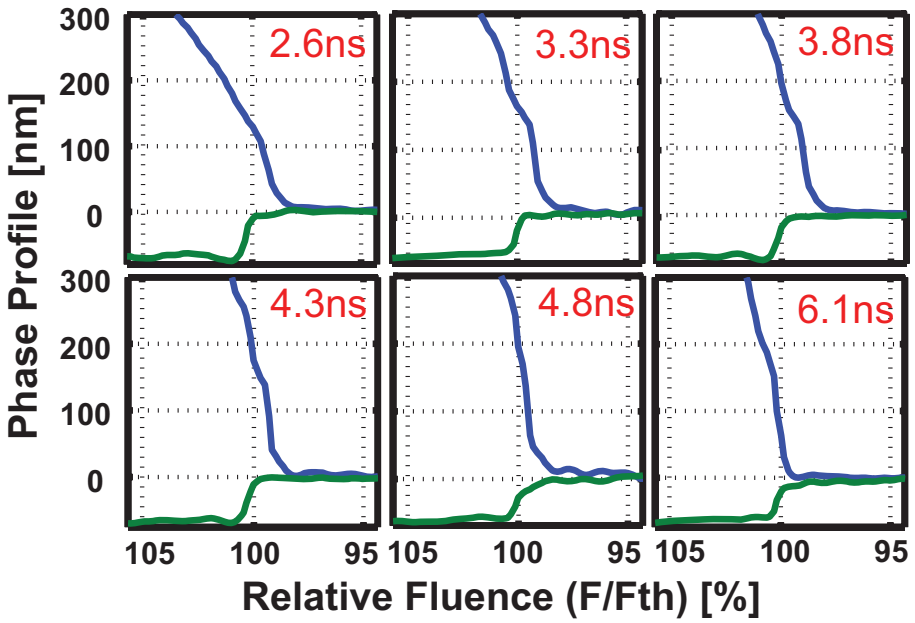

Figure 3.10: Profiles of the ablating plume as measured on gold for different delays. Blue line represents ablating surface while green is final crater. Surface becomes steeper around ablation threshold, as plume expands.

errors in the slope of the surface increase.

The combined effects of errors in the slope and the uncertainty of the local ablation threshold give rise to errors in the retrieved surface excursion which are in the range of the excursion amplitude itself.

3.2 Ablation thresholds and crater morphologies

A characteristic feature of the ablation with a single femtosecond pulse is a very sharp threshold. Within a very narrow fluence range the response of the material changes from essentially no material removal to formation of the ablation crater of finite depth. For a laser pump pulse with a spatially varying intensity/fluence distribution (usually bell shaped) this sharp ablation threshold manifest itself in the formation of an ablation crater with a sharp boundary. The crater boundary therefore provides the information on the value of the ablation threshold for a particular sample and its width provides some information on the "sharpness" of the ablation threshold. The depth of the crater can give an insight into the mechanism of ablation that is predominant in the fluence regime near the threshold.

This section discusses following topics: the technique used to determine the ablation thresholds; results of the depth measurements on ablation craters; crater morphologies discussion wit emphasis on laser induced periodic structures.

3.2.1 Determination of thresholds

The focused laser pulses used in experiments presented here have a bell-shaped spatial intensity distribution which can be well approximated by a Gaussian function. To illustrate relation between laser fluence and ablation threshold, the distribution of intensity of two such pulses is plotted in figure 3.11. For the pulses of equal shape, but of a different peak fluence, the one with a higher fluence will make a larger crater. The crater boundary represents the contour of constant (threshold) fluence on the irradiated sample. For a Gaussian laser beam that irradiates the sample at some angle of incidence, as in our case, the contours of the constant fluence are ellipses, and thus the craters have an

elliptical shape. For the sake of clarity, the following discussion only considers a circular Gaussian fluence distribution[2], but a generalization for an elliptically shaped beam is straightforward.

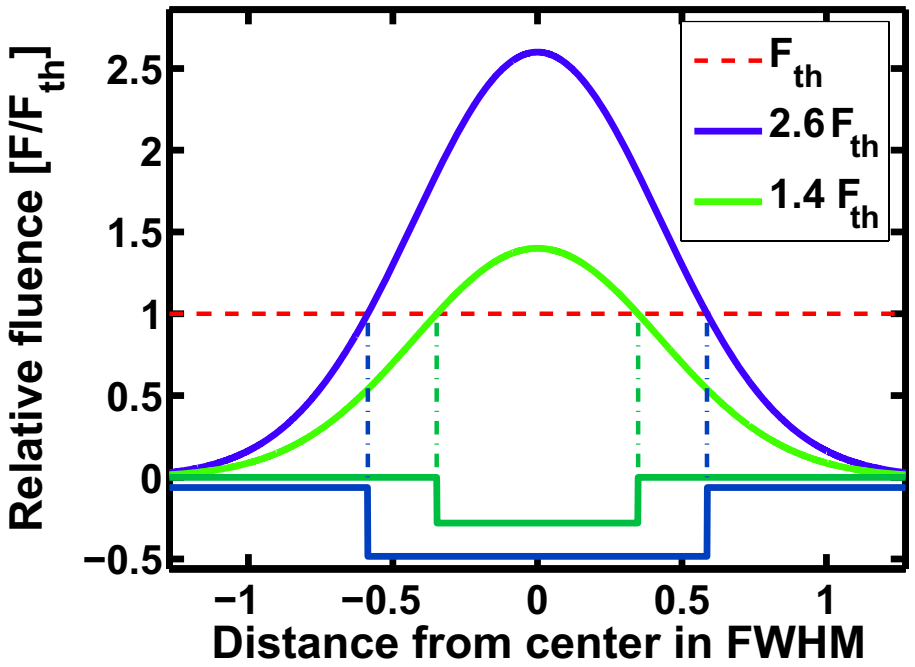

Figure 3.11: Plot of two gaussian fluence profiles, 2.6 and 1.4 times ablation threshold (F_{th}). Crater is formed where fluence reaches F_{th}, and increasing fluence increases crater size. Lateral dimensions are normalized to the Full Width at Half Maximum (FWHM).

A simple method to determine the ablation threshold, which was first described by Liu [77], is used here. The fluence of the light pulses is assumed to have a Gaussian spatial profile, and the local fluence at a certain distance from the center is given by:

$$F(r) = F_0 \cdot e^{-\frac{r^2}{\rho^2}} \tag{3.13}$$

Here F_0 is the peak fluence in the center of the beam and is defined as:

[2]this is a case when laser beam has a normal incidence angle with respect to the sample.

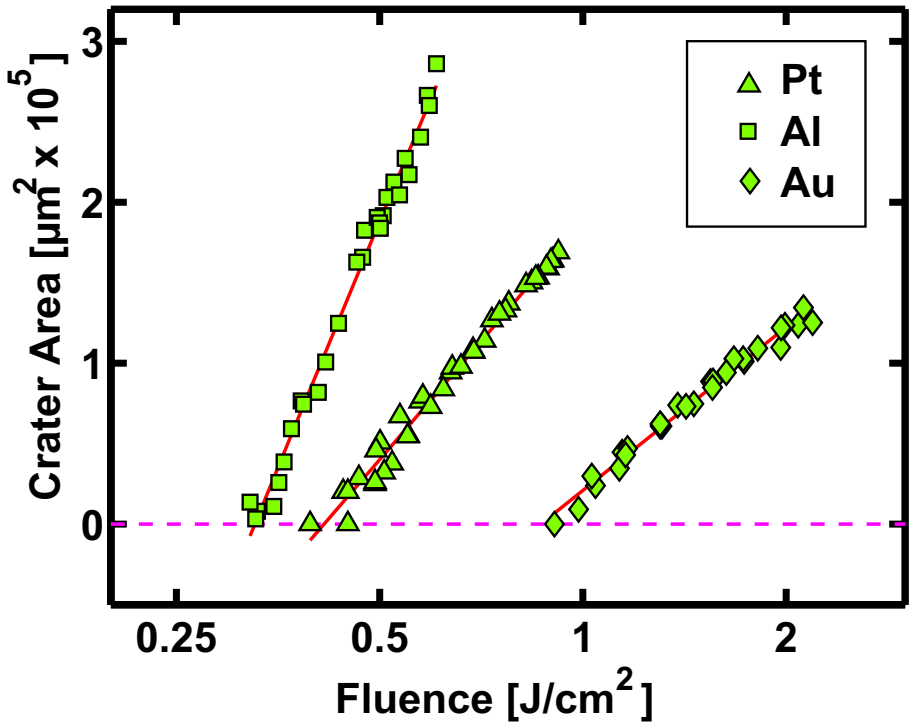

Figure 3.12: The ablation threshold calibration plot for Au, Pt and Al. Area of the crater is plotted as a function of the incident laser fluence. Offset on x-axis defines threshold fluence for ablation, and slope defines beam parameter ρ (see text)

$$F_0 = \frac{E}{\sqrt{\pi}\rho} \tag{3.14}$$

where E is the total pulse energy and ρ is the spatial radius where the fluence is e times lower than at the maximum ($F = \frac{1}{e} \cdot F_0$). I will refer to ρ as the *beam parameter*. The variable r represents the radial distance from the center of the beam.

For the processes such as ablation and melting, which have well defined thresholds, the surface will be modified within an area defined by the contour of the threshold fluence:

$$F(r_{th}) = F_0 \cdot e^{-\frac{r_{th}^2}{\rho^2}} = F_{th} \tag{3.15}$$

Taking the logarithm of equation 3.15, the radius r_{th} of the ablation crater (or molten spot) can be expressed as:

$$r_{th}^2 = \rho^2(\ln F_0 - \ln F_{th}) \tag{3.16}$$

From equation 3.16 it follows that the area of the ablation crater scales linearly with the logarithm of the incident fluence.
As an example, three such dependencies are presented in figure 3.12, for Al, Au and Pt films of 100nm, 125nm and 104nm thickness respectively. The measured crater areas are plotted as functions of the incident laser fluence in a semilogarithmic plot. The data points fit the straight lines reasonably well. The slopes of the fitted lines, ρ^2, define the laser beam parameters. Extrapolating to zero crater size, intercepts with fluence axis yield ablation threshold fluence.
Spatial fluctuations of the beam shape on a pulse-to-pulse basis, as well as spatial imperfections of the sample manifest itself in the deviations of the points from the fitted line.

3.2.2 Crater depths and ablation thresholds for different materials

Knowledge of the crater depth provides the information on the amount of material removed during the ablation. The flying shell, mentioned in the Introduction, that forms during the ablation by fluences comparable to the ablation threshold, can reach the thickness as high as the crater depth [32]. This information can lead to a better understanding of the appearance of Newton rings. The results of the ablation threshold together with the respective crater depth measurements on different metals are summarized in the table 3.1.

The crater depths are measured using the interferometry technique described in Section 3.1. This technique is compared with profiles obtained by Atomic Force Microscopy (AFM), for the 400nm thick Al films, and the results are in

Material	Polarization	Film thickness [nm]	Ablation threshold [J/cm^2]	Crater depth [nm]
Au	$\sigma-$	125	0.87	60
Au	$\pi-$	125	0.41	60
Au	$\pi-$	57	0.35	20-25*
Au	$\pi-$	34	0.13	detached
Pt	$\sigma-$	104	0.41	40
Pt	$\pi-$	104	0.30	40
Pt	$\pi-$	60	0.21	40
Pt	$\pi-$	31	0.16	10
Al	$\pi-$	400	0.33	180
Al	$\pi-$	100	0.42	45
Ti	$\pi-$	>500	0.180	7

Table 3.1: Ablation thresholds and crater depths for investigated metal films.

good agreement with each other. For the 34nm thick Au film, ablation always leads to the complete removal of the film from the substrate.

In the case of the 57nm thick Au film it was not possible to uniquely determine the ablation crater depth, because the film was detached from the substrate for all but fluences very close to the the threshold (see figure 3.17). In this case, the retrieved phase shift of the irradiated final spot, with respect to the unexcited one, is influenced by difference in the optical constants between Au film and Si substrate, as well as the crater depth. This is discussed in next section in more detail.

3.2.3 Sample thickness- threshold dependency

As is evident from table 3.1, the ablation thresholds differ for samples made of same material, but different thickness. The information about the amount of energy that is deposited into the ablating material can give additional insight into the ablation process and the question is how the amount of deposited energy at threshold depends on the sample thickness. The deposited energy density can be estimated knowing the sample reflectivity using the values of the

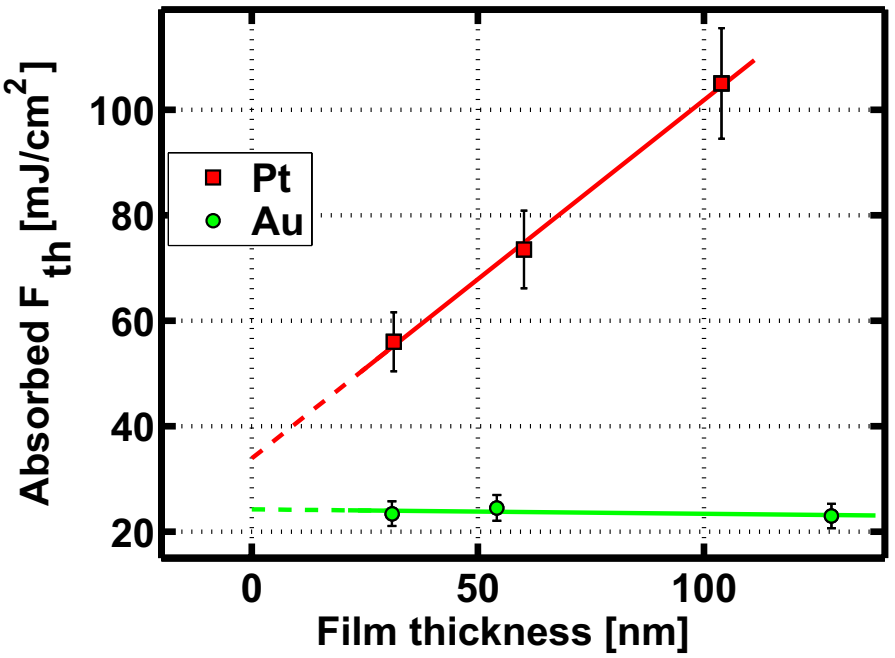

Figure 3.13: The absorbed threshold fluence for different thicknesses of the metal film. The full squares represent platinum and circles gold samples. Gold samples have high reflectivity for λ =800 nm, and small reflectivity changes caused by surface imperfections makes dramatic change in absorbed energy. For platinum, fitted absorbed fluence increases linearly with film thickness, while for gold it remains almost constant.

incident ablation threshold fluence for Au and Pt films of different thicknesses (see Table 3.1). The reflectivity for gold and platinum calculated using optical constants [40] is R_{Au}=96.2% and R_{Pt}=66%, for λ= 800nm and $\pi-$ polarization, and a 35° angle of incidence.

For the platinum sample, the absorbance is relatively high[3], and, even including observed small changes in reflectivity due to surface roughness, one would not expect a significant difference in the absorbed energy. On the other hand, gold has a relatively high reflectivity under similar conditions, and even the similar small deviations of reflectivity from the theoretical value would mean a up to an order of magnitude difference in the absorbed energy.

The reflectivity was measured under conditions identical to those in the experi-

[3]Absorbance is (1-R) and it has value of approximatelly 33%

ment for gold films. The results are summarized in the table D.1, which can be found in Appendix D. The reflectivity for three investigated films differs from the expected values (determined using the optical constants [40]).

Figure 3.13 shows the dependance of the absorbed ablation threshold fluence for gold and platinum, for three different sample thicknesses (exact values given in Table 3.1). For increasing film thickness the absorbed fluence at the threshold increases linearly for platinum but it remains almost constant for gold films.

As it has already been discussed in chapter 2 in the case of an instantaneously homogeneously heated film, the negative pressure in the middle of the film is determined by the strain amplitude, caused by the initial temperature, which is independent of thickness. This means that the volume energy density, needed to heat the material to this temperature, is constant, and the absorbed fluence is expected to scale linearly with the film thickness. The conclusion that the whole the whole film thickness is heated to the same temperature, can not be drawn since fitted line does not start in zero energy for null thickness, although for platinum the deposited energy scales linearly with film thickness, as it can be seen in figure 3.13.

Unlike to platinum, gold shows different behavior, where absorbed fluence needed to induce ablation remains constant[4] for three investigated films of different thickness. The question arises about how appropriate is the model of instantaneous heating in the case of gold films.
The work by Brorson *at al* [42] demonstrated that hot electrons are distributed extremely fast through the thin gold films (100fs for 100nm), so film heating is governed mainly by energy exchange between electrons and the lattice. However, recent measurements on gold [78] show that this energy exchange occurs on $10-20$ps time. The typical sound velocity for gold is approximately $c_s \approx 3$km/s [79, 39], and the strain waves will meet in the middle of the film after approximately $10-15$ps for 30nm thick film. At this moment, the material temperature

[4]Within error bars.

is still rising and maximal tensile stress, which could be expected from amount of deposited energy, is thus not yet reached. For spallation to occur, negative pressure has to exceed tensile strength. The amplitude of the pressure waves is proportional to the temperature, and for thinner films, higher initial electron temperature is needed to reach the negative pressure amplitude that exceeds the material tensile strength. This effect might explain that the threshold fluence for thinner films is higher than expected.

3.2.4 Morphologies of the ablation craters

As already mentioned, one result of the ablation caused by single femtosecond pulse is a sharp threshold from incident fluence. This was demonstrated by the observation of the sharp boundaries of the ablation craters [80, 13]. The fluence of a Gaussian laser beam is mapped on the sample surface along the spatial coordinate and the width of crater boundary gives estimate on the threshold fluence range. For high quality samples (single crystal GaAs wafers), the boundary can be as narrow as 300nm [13].

Due to the sample quality, reflectivity and absorption can deviate locally from values expected from the optical constants. The surface roughness or dust particles change the absorption process and the amount of absorbed energy is altered locally. This, in turn, shifts the apparent position of the crater boundary. As an example, figure 3.14 shows ablation craters on a GaAs wafer and two Aluminium films of two different thicknesses. In all cases the samples were irradiated at approximately 1.4 times the ablation threshold fluence in order to have comparable excitation conditions.

The ablation crater on GaAs has a regular elliptical shape and the boundary is sharp[5]. Craters on 400nm thick aluminium sample show a wider boundary with more irregularities than the thinner one (100nm) of the same material. Thin sample has a sharp boundary (sharper than it can be resolved by optical

[5]less than 300nm as reported in work by Temnov *at al*[25]

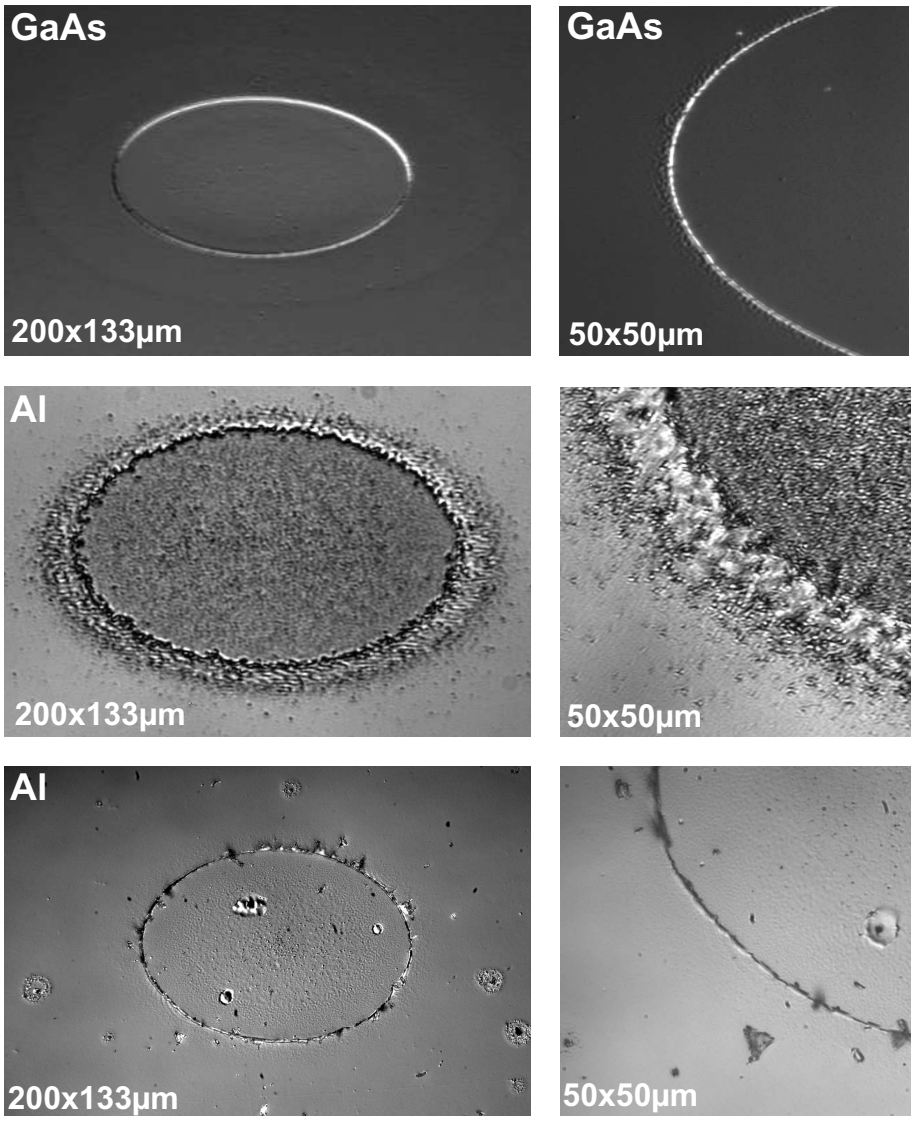

Figure 3.14: Crater boundary morphology depends on the material, as well as on its surface quality. Whole craters are depicted in the left column, and zoomed view on boundary is presented in the right column. The peak laser fluence in all three cases is approximately 40% higher than respective fluence needed to induce ablation. GaAs crater has regular elliptical shape, with sharp boundary. Crater boundary on 400nm thick aluminium film is wider and less regular than for GaAs and thin (100nm) Al film.

microscopy, $< 1\mu$m). However, in contrast to to the boundary of GaAs, there are bigger pieces of material ($> 5\mu$m lateral scale) that are randomly distributed along the boundary, and whose hight extends up to 10-20 microns.

The surface of a 400nm thick sample has more irregularities, than the 100nm thick sample. These irregularities are induced by difficulties of growing thicker metal films. In the study made by Elson *at al* [76] it has been demonstrated that even the surface roughness, smaller than the wavelength of the incident light, changes absorption. It has been demonstrated that surface roughness increases absorption from 1-2% from the initial value for a case of random surface irregularities up to more than 100% of the intrinsic absorption (due to optical constants) because of periodic irregularities. Random surface irregularities smaller than the incident wavelength induce fluctuations in absorption that can explain observed deviations in crater boundary from a perfect ellipse. Observations on other materials indicate that this is the case, and a more accurate explanation is given see in the next section.

Another feature of the ablation on aluminium are different widths of the craters for two sample thicknesses, which might be depending on surface quality as well as on film thickness. Craters on the 100nm thick film have much narrower ($<1\mu$m) boundary than on on 400nm (10-15 μm). Elliptically averaged profiles of crater depth are presented in figure 3.15. Profiles are obtained by interferometry as described in Section 3.1. For the 100nm thick sample, the crater has a boundary sharper than the resolution limit, while craters on 400nm film show a gradual smooth profile that decreases towards bottom of the crater. One possible explanation could be that flying shell might not detach completely, in the case of thicker film, at a a place irradiated close to the threshold fluence. Namely, it has been observed in the spallation experiments on aluminium performed by Tamura *at al* [81], that during the back surface induced spallation (using the 50fs laser pulses), the detached shell thickness depends on the initial film thickness. It has also been observed that for thicker shells material is not

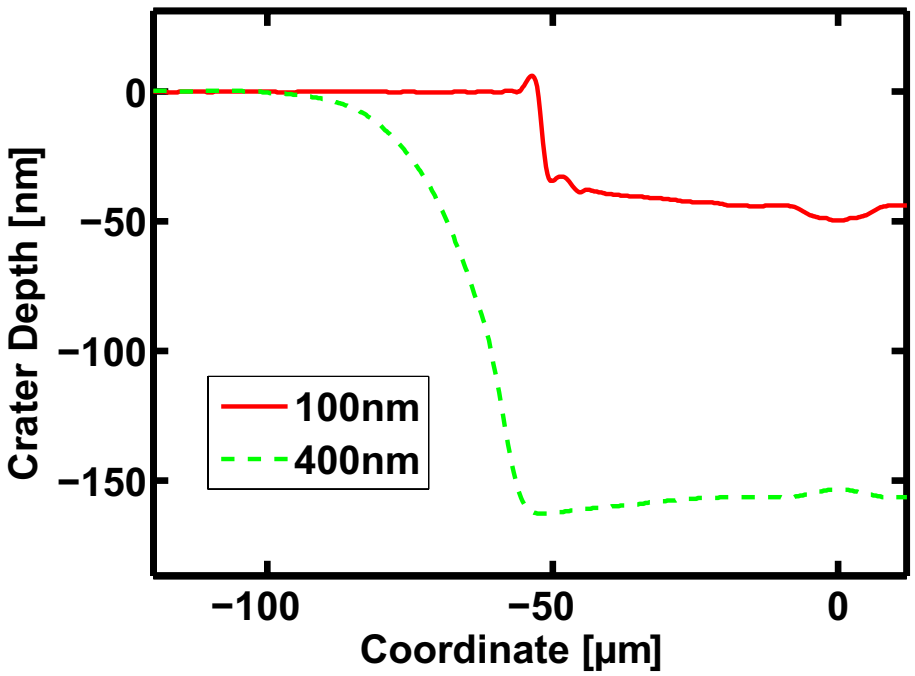

Figure 3.15: Depth profiles of the ablation craters on aluminium films, from figure 3.14.

detached at all, and for thinner some residual pieces of shell are still attached to the sample.

In the case of the 400nm thick film, near the threshold part of the shell does not detach, but returns back to the sample. It is expected that with increasing fluence shell decreases in thickness as reported by Anisimov *at al* [32], and this would lead to the situation when shell becomes so thin that it completely detaches.

To summarize, the craters on semiconductor samples, with high surface quality (GaAs, Ge, InPh wafers) [13] show the sharp regular elliptical boundary. Craters on 100nm thick aluminium sample indicate that the ablation threshold is indeed sharp for this material, but there is a mechanism that results in wider crater boundaries for thicker film (400nm). The surface irregularities, with a size greater than the wavelength of radiation that initiates the ablation process

induce the interference on surface of the sample, thus rising laser intensity in localized area (interference maxima).

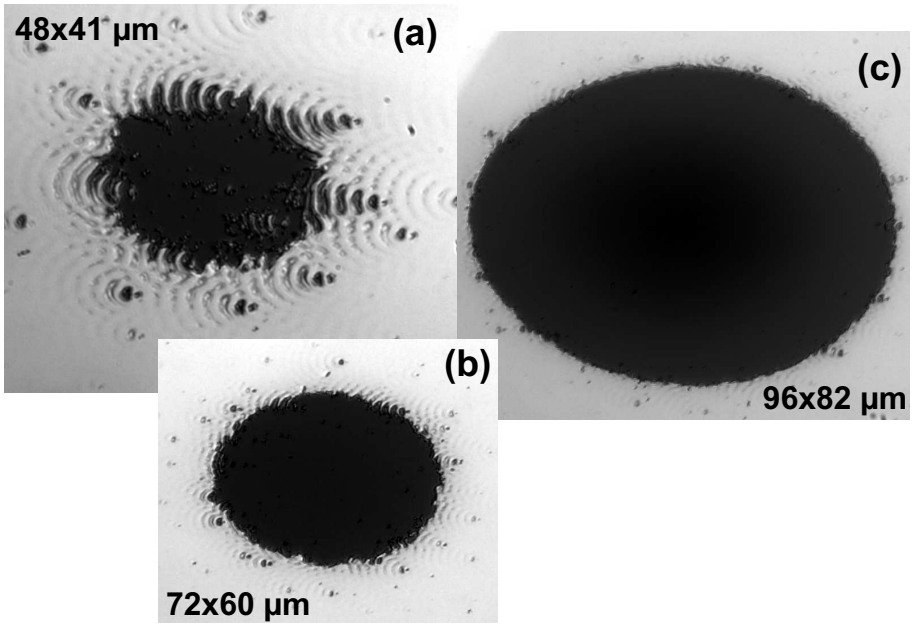

Figure 3.16: Craters on Gold 30nm film, for three fluences ((a)1.03·F_{th}, (b)1.6·F_{th} and (c)3.2·F_{th}). For all three fluences metal film is completely detached from substrate. Notice periodic structures on crater boundary.

Figure 3.16(a) shows an example that illustrates this effect quite clearly. These are micrographs of ablation craters on a 34 nm thick gold film on Si substrate. The gold film is completely detached for any fluence that induces visible modification on sample surface. Images are taken using a Normaski microscope that uses illumination light of a wavelength λ=546nm. At this wavelength silicon has considerably lower reflection [40] than gold. Therefore the dark bottom of the ablation crater in this case indicates that the gold film is detached and the Si substrate appears as dark spot. The effect of interference manifests itself in periodical structures on the crater boundary (see figure 3.16 and 3.17), as well as inside of the crater as shown in figure 3.18. On thicker films this effect leads to apparent broadening of the crater boundary, also shown in figures 3.17 and 3.18.

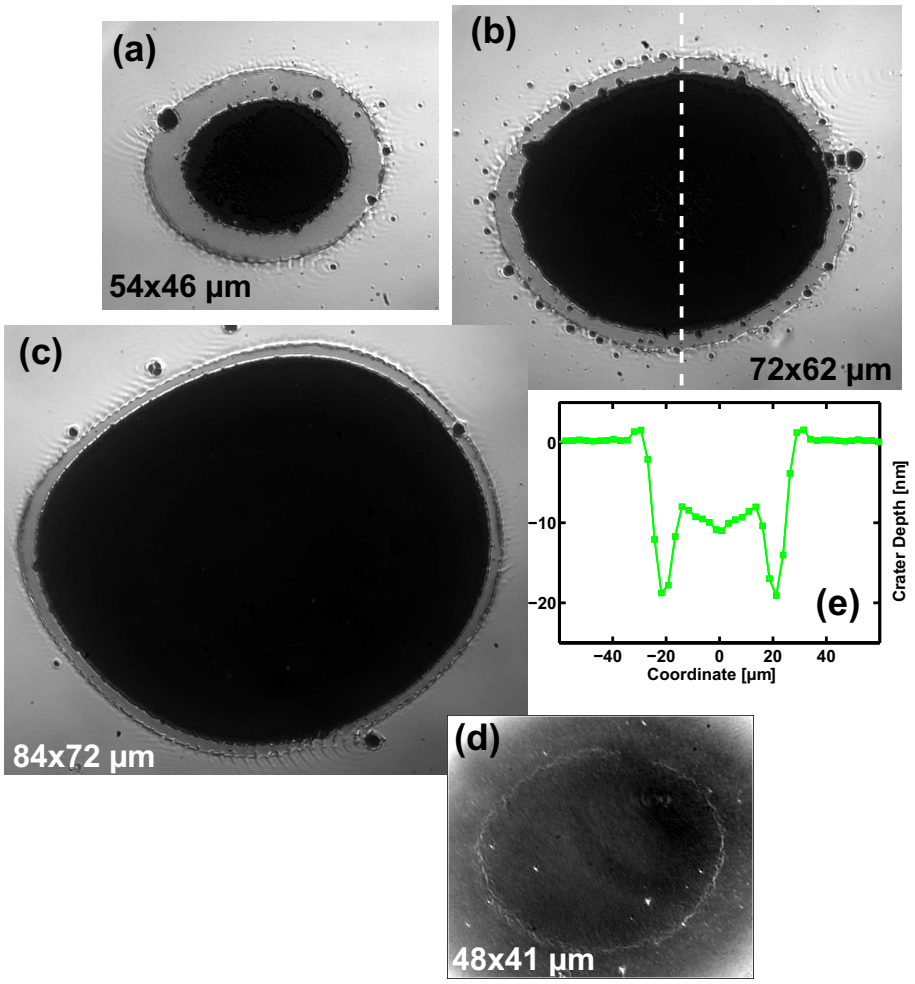

Figure 3.17: Craters on gold 57nm film, for three fluences above the threshold((a) 2.1·F_{th}; (b) 2.7·F_{th} and (c) 3.3·F_{th}). Film is detached in the center of the crater, and Si wafer can be seen. For highest fluence(c), in the center of the crater on Si substrate crater-like structure is visible(d); Graph (e) shows profile of the crater, from image (b) and demonstrates ambiguity when interferometry technique is used for materials of different optical properties.

Detachment of the metal film due to laser ablation was observed in all investigated gold films, as well as on 31 and 60 nm thick platinum films. On thicker films, formation of an ablation crater in material is observed, and only for higher fluences does the film detach from the substrate. Threshold fluences for detachment on samples where this is observed are approximately two times the respective ablation threshold fluences. On figure 3.17 craters on 57 nm thick

gold film are presented, for three different fluences. On the crater created with the lowest fluence (figure 3.17(a)) there is a approximately a 6 μm wide region of gold layer left after ablation. In this region, reflectivity is lower indicating that its thickness is smaller enough so that a significant portion of the probe light is transmitted and absorbed in the Si substrate (reflectivity for bulk Au is 81% and for Silicon 30% at λ=546nm).
An attempt to retrieve the crater profile using interferometry technique is presented in graph 3.17(e) which represents phase of the light reflected from the surface at position of crater presented at image 3.17(b). A phase profile is taken along the white dashed line. The unexpected apparent decrease of crater depth to 10 nm from initial 20 nm[6], coinciding with a sudden drop of reflectivity in microscopic image, can be explained by a phase jump of probe light due to the change of optical constants between film and substrate. Using optical constants for gold ($\tilde{n} = 1.56 + 1.96i$) and silicon ($\tilde{n} = 5.57 + 0.39i$)[40] the expected jump of the phase due to the different optical properties of these two materials is estimated to ≈50nm. This jump explains the unexpected value for crater depth at place where metal film is detached.

Another feature observed on 57 nm thick gold films is that higher fluences (more than three times the ablation threshold) modify the silicon substrate that underlies gold film. Careful optical investigation of the irradiated spot reveals the presence of additional crater-like structures in the center of the ablation crater.

3.2.5 Laser induced periodic structures

A laser beam that irradiates the surface of a sample can scatter on the surface irregularities or on dust particles. The scattered light interferes with the incident wave, imposing a modulated fluence distribution on the sample surface. This modulation influences the ablation process because it shifts threshold fluence

[6]Unexpected because when gold film is detached, crater depth should increase, rather than decrease.

value towards or away from the center of the laser beam, depending weather modulation decreases or increases local fluence. Assuming that the fluence gradient along the surface due to diffraction is much higher than the one due to the Gaussian distribution of laser pulse, the ablation threshold will be reached two times for each modulation period. That is why the crater boundary shape represents superposition of ellipse and this interference pattern.
The most obvious example is the case of 34 nm gold films irradiated with laser pulses near threshold peak fluences (see figure 3.16(a)), where the gold layer is completely removed from the substrate, and deviations of the crater boundary from a perfect ellipse are easiest to observe. Visually similar deviations can be observed on the 57 nm and 125 nm thick gold films (see figure 3.17) and 3.18).

These laser induced periodic surface structures are known as "ripples" or LIPSS in the literature [82, 83], and here I will refer to them as *ripples*. The two most obvious quantities which characterize these ripples are their characteristic wavelength and their spatial extent.

For ripples presented here, the maximal distance from the scattering center to the disappearance of the ripple structure is approximately 25μm, .
To analyze the formation of the ripples, a laser pulse is assumed to be a plane wave packet with a typical lateral size significantly larger than observed ripple structures. As focus size is typically 100 μm in diameter and the pulse duration is τ=50 fs this condition is fulfilled. The leading part of scattered waves interferes with the incident wave that follows. The last interference occurs between falling edge of the incident laser pulse and the leading edge of the scattered wave. The leading edge of the incident wave wipes along the surface with a velocity $c\sin\theta$ (see figure 3.19(a)), while the scattered wave travels with c (c being the velocity of light and θ angle of incidence). When the trailing part of the wave scatters, the leading edge has already advanced $\tau c\sin\theta$. The time it takes these two waves to meet is $t = \frac{\tau}{1-\sin\theta}$. This parameter determines the length of ripple structure, which is equal to $l = t \cdot c = c \cdot \frac{\tau}{1-\sin\theta}$, or approximately

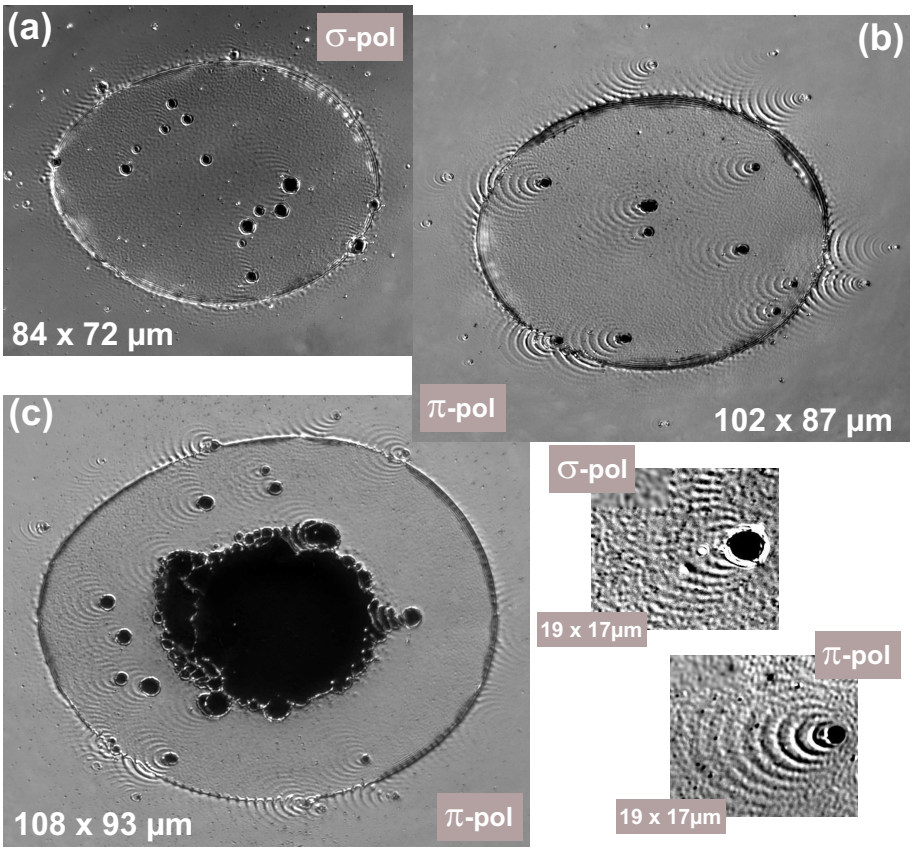

Figure 3.18: Ablation craters on gold films of 100nm thickness, irradiated with (a) σ and (b) π-polarized beam, the peak fluence $1.4{\cdot}F_{th}$ in both cases. For higher fluence (c), $\approx 2.3{\cdot}F_{th}$, film is detached in the center. Notice difference in periodic structures generated around irregularities on the sample in case of σ- and π- and polarization (zoomed insets with enhanced contrast).

30μm.

The wavelength of the ripple structures can be estimated by analyzing the wave vectors of the incident and the scattered wave. Figure 3.19(b) presents look from the top of image (a), where z defines vertical axis and the incident wave defines direction of x axis. In this scheme the component of wave vector of incident light that is parallel to the surface can be expressed as:

$$\vec{k}_{inc} = \frac{2\pi}{\lambda}\begin{pmatrix}\sin\theta\\0\end{pmatrix} \tag{3.17}$$

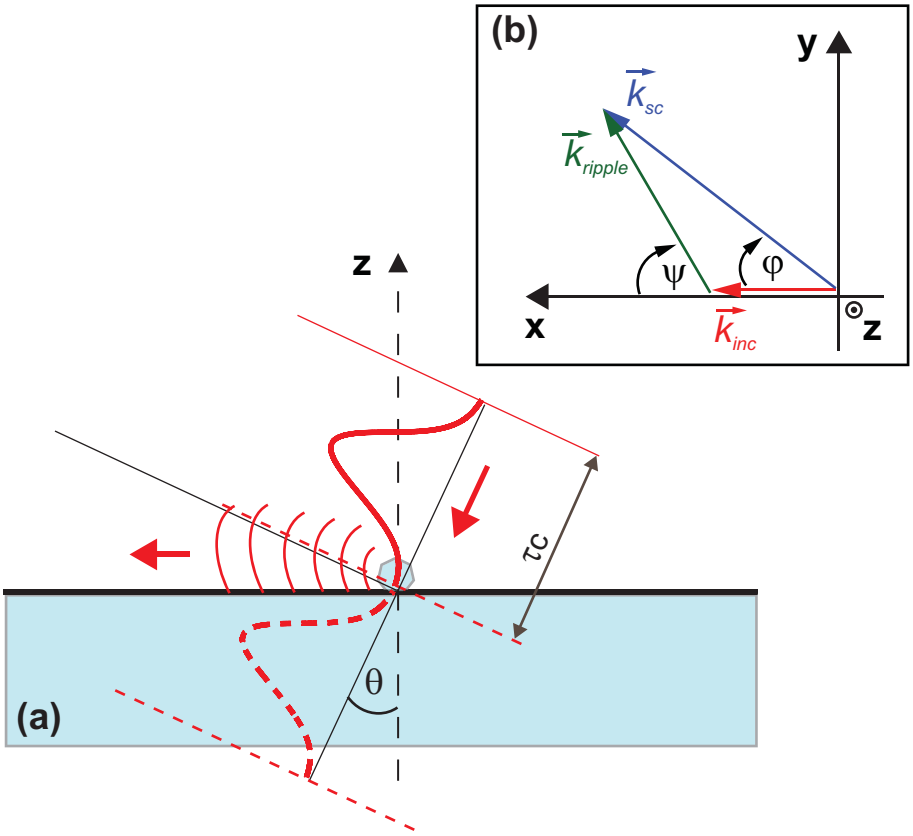

Figure 3.19: Formation of laser induced structures. Scattered light interferes with portions of the incoming pulse. Inset (b) shows formation of ripple wave vector (see eq. 3.19)

where λ is the wavelength and θ is the angle of incidence [84]. The scattered wave vector, on the other hand is assumed to take all directions across the surface, and it can be expressed as:

$$\vec{k}_{sc} = \frac{2\pi}{\lambda}\begin{pmatrix}\cos\varphi \\ \sin\varphi\end{pmatrix} \tag{3.18}$$

where φ is horizontal azimuth angle, defined by vector $\vec{k}_{inc}$ and radius vector between the scattering center and the observed ripple in $x-y$ plane. The resulting interference pattern is characterized by wave vectors:

$$\vec{k}_{ripple} = \pm(\vec{k}_{inc} - \vec{k}_{sc}) \tag{3.19}$$

The ripple wave vector can be represented in similar form as incident and scattered ones:

$$\vec{k}_{ripple} = \frac{2\pi}{\Lambda_R}\begin{pmatrix}\cos\psi\\ \sin\psi\end{pmatrix} \tag{3.20}$$

where ψ is the horizontal azimuth angle of the vector $\vec{k}_{ripple}$ with respect to the x axis and Λ_R is the ripple wavelength in the specific direction (see figure 3.19(b)). Solving this system of equations, we get relation for the wavelength of ripple structure, as function of the incident angle θ and the angle φ.

$$\Lambda_R = \frac{\lambda}{\sqrt{(\cos\varphi - \sin\theta)^2 + \sin^2\varphi}} \tag{3.21}$$

An example for the typical ripple pattern for a wavelength of incident light λ=800nm and the angle of incidence θ=35°[85], calculated using the equation 3.21, is presented in figure 3.20. The scattering center is represented by a cross (+), and interference maxima produced by the incident and the scattered wave are drawn as full green lines. The spatial wavelength of the ripple structures changes for different azimuthal angles of the incident wave (x axis).

The observed ripple pattern in case of 125 nm thick gold film is shown in figure 3.18. Image (a) shows the crater created by $\sigma-$ polarized and image (b) with $\pi-$ polarized pump beam. Efficiency of formation of ripple pattern as function of polarization and scattering direction have been discussed extensively in literature [84, 83, 82, 86, 87], but details will not be considered here.

A general trend confirmed in our measurements (see figure 3.18) is that the ripple pattern is perpendicular to the polarization of the incident light.
The measured wavelengths of patterns produced with $\sigma-$ polarized beam on image 3.18(a), which have been directed at an angles of 45° and 65° are Λ_1 =1.2μm and Λ_2 =1.0μm. Values calculated using equation 3.21 are Λ_1 =1.1μm and Λ_2 =0.9μm respectively.
The $\pi-$polarized beam produces a pattern that differs from one created with

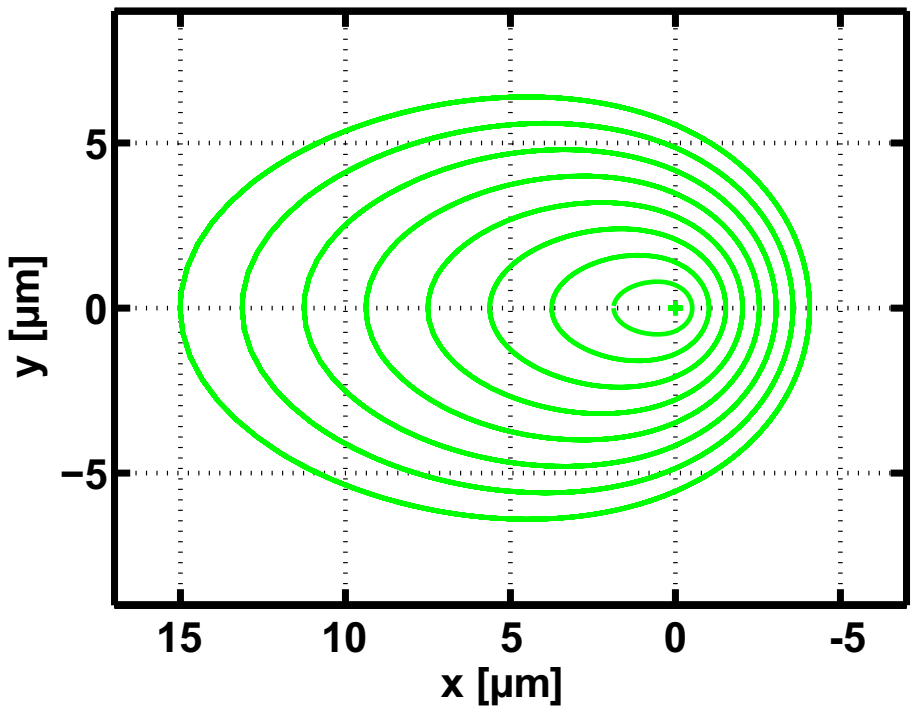

Figure 3.20: Calculated ripple pattern around scattering source assuming same efficiency in all directions. Wavelength depends on azimuth angle from incident wave (x axis).

$\sigma-$ polarized light, as shown on image 3.18(b). The measured wavelength of the ripples in this case is Λ_R =1.9μm, while the calculated value is Λ_R =1.8μm. Considering that the incident angle θ and azimuth angle φ are known with an accuracy of about 5-10%, calculated and measured values for ripple wavelength are in good agreement.

The laser induced periodic structures presented in this section represent a limiting factor for the accurate determination of ablation thresholds because they strongly distort the elliptical crater boundary shape, which, as we have seen, is critical to determining the incident laser pulse shape. On the other hand, as we will see in following section, diffraction between scattered and incident waves induces transient reflectivity modulations during the laser ablation process. Due to its high spatial frequency, these modulations of reflectivity in-

duces errors in the fourier processing of interferograms. Therefore, one would like to avoid ripple appearance in these interferometric measurements as much as possible. It has been observed that intensity of transient ripple pattern is much lower in the case of $\sigma-$polarized than in $\pi-$ polarized pump radiation. Therefore the interferometric measurements of surface expansion presented in section 3.4 were conducted with $\sigma-$polarized pump radiation.

3.3 Transient reflectivity and Newton rings

Reflection of light between two surfaces, a spherical surface and an adjacent flat surface produces an interference pattern [88]. This phenomenon is called Newton rings, named after Isaac Newton, who first analyzed them. When viewed with monochromatic light, the pattern appears as a series of concentric, alternating dark and bright rings centered at the point of the largest distance between the two surfaces. The slope of the spherical surface increases outwards, so the distance between the rings gets smaller for the outer rings.

The discovery of Newton rings (N.R.) during the fs laser ablation led to the development of a "bubble model" [16] (figure 1.2 in Chapter 1). The idea is that an optically sharp but transparent interface of relatively high density (the flying shell (1)) is moving away from the sample surface leaving a gas-liquid mixture in between. As a result of the interference between the light reflected from the shell and the light which is transmitted through the shell and reflected from the non-ablating back surface (3), the N.R. are observed. The pattern changes with time, and by counting the number of fringes, one can follow the expansion of the surface, i.e the movement of the shell. This type of measurement gave the first quantitative information on ablation plume dynamics [80]. In the work by Bialkowski *at al* the appearance of the Newton rings has been found as a universal feature for a large number of materials, which include semiconductors (Si and GaAs) and metals (Al, Au, Ti, Pt ...).

In the experiments presented in this thesis, the transient reflectivity measurements are a supplement to the interferometric measurements. Although it has been observed that N.R. occurrence on metals is qualitatively similar to that on semiconductors (i.e. Si and GaAs) there are some aspects that shed new light on this phenomena, which are discussed here.

The next section discusses the calculations of reflectivity for ablating plume using the thin film modeling, in order to prepare ground for discussing experi-

mentally measured transient reflectivity during fs ablation, which are presented in the section 3.3.2. In this section are presented some examples of the appearance of N.R. on metals during the ablation process. And finally, the conclusions will be summarized to explain and briefly report on the transient ripples, which precede the periodic structures discussed in the previous section and how these influence observation of the Newton rings and the interferometric measurements.

3.3.1 Modeling of reflectivity for a moving shell

A schematic of the physical system whose reflectivity we want to calculate is presented in the figure 3.21. There is a shell, with a thickness d_1, of the expanded liquid material at some distance from the nonablating back-surface (usually considered to be molten). The space between the shell and the back-surface is filled with a two phase mixture (gas and liquid). The shell moves away from the surface, so its distance $z(t)$ from the initial position increases with time.

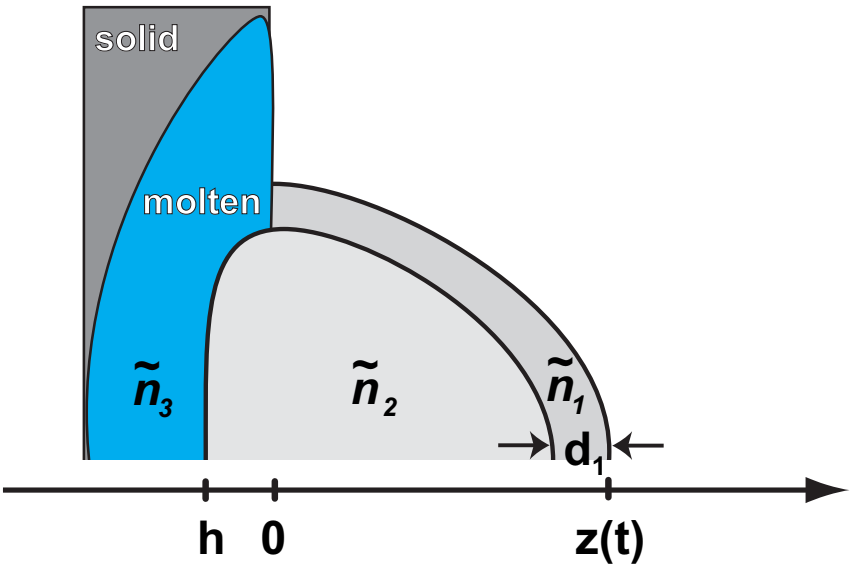

Figure 3.21: Scheme of a ablating plume in "bubble model": the flying shell of thickness d_1 moves away from the sample surface and at a certain moment in time it is at distance $z(t)$. The space in between is filled with two phase mixture. (Adapted from: Temnov 2004 [25])

The incoming probe light is partially reflected and partially transmitted from this shell. The ratio of reflected and transmitted intensity depends on the shell thickness d_1 and on its optical properties (i.e. optical constants $\tilde{n}_1$). Absorption of the light in the two phase region, between the shell and non ablating substrate, is neglected. The calculations of the absorption in this kind of system [25], with much lower density than that of a solid or a liquid[7], show that absorption is much lower in the two-phase region than in the flying shell, and thus it can be neglected.

The light inside the shell reflects from the back-surface, transmits through the shell once again and finally interferes with the light reflected from the shell, resulting in Newton rings pattern. The method for calculating reflectivity and phase shift is derived in Reference [89] and details will not be presented here.

One can estimate the ablation shell thickness, considering typical crater depth values, which can be up to several tens of nanometers, depending on the material. The bottom of the crater is considered to be a thick bulk material. For both the ablating shell and crater bottom, optical constants of unexcited metals are taken in order to get first impression on optical behavior of the ablating front. In the real case, the optical constants of the material that the shell is made from which in a hot and expanded state near the binodal can differ from that of a unexcited material. For an exact quantitative study of reflectivity, they must be taken into account.

The main result of this calculations is that both the phase shift and the intensity modulation of the reflected light are extremely sensitive to the shell thickness (d_1). The summary of calculations results for an ablating gold film is presented in the figure 3.22. The ablating gold shell is assumed to have a parabolic shape [80], and the maximum shell distance from unexcited sample surface is a 1000 nm. The thickness of the shell is considered to be constant on

[7] When Newton rings are visible, shell has moved at a distance that equals few wavelengths away from the surface (this is why inteference is visible in the first place. Therefore, the volume inside the shell is much larger than one occupied by material before excitation and density is dramatically decreased.)

each graph, but it differs from one graph to the other, as indicated.

For a 60 nm thick shell, the observed phase follows the ablation front closely. However, the reflectivity is only weakly modulated, which relates to a very low contrast of the Newton rings. As the thickness decreases, the fringe contrast increases but phase starts to deviate from the ablation front. In the extreme case, for the shell thickness of approximately 10 nm, the modulation contrast is the highest, but the phase is also modulated. The phase jumps coincide with minima in the reflectivity profiles. These jumps can even lead to negative values of observed phase, as in example of the 12 nm thick shell on figure 3.22. Further decrease of shell thickness decrease the reflectivity modulation amplitude (leading to the decrease in contrast of N.R). The detected phase in this case does not follow the ablation front at all.

The other investigated metals (Al, Pt and Ti) have been subjected to the same analysis. They show similar qualitative behavior, which can be grouped into three cases:

- Thin shell: low to high contrast of the Newton rings, the phase does not follow the ablation front;
- Shell of the medium thickness: high contrast of the Newton rings and the phase follows the ablation front (with jumps which coincide with reflectivity minima);
- Thick shell: low contrast or no Newton rings; the phase exactly follows the ablation front.

As a consequence, one can expect problems detecting the expansion of the flying shell for some materials which show good contrast of Newton fringes during the ablation, like silicon (studied by Temnov *at al*[25]) and titanium, which is presented in this work in folowing sections. As a contrast to that, materials that form thick shell during the ablation process show weak or no Newton

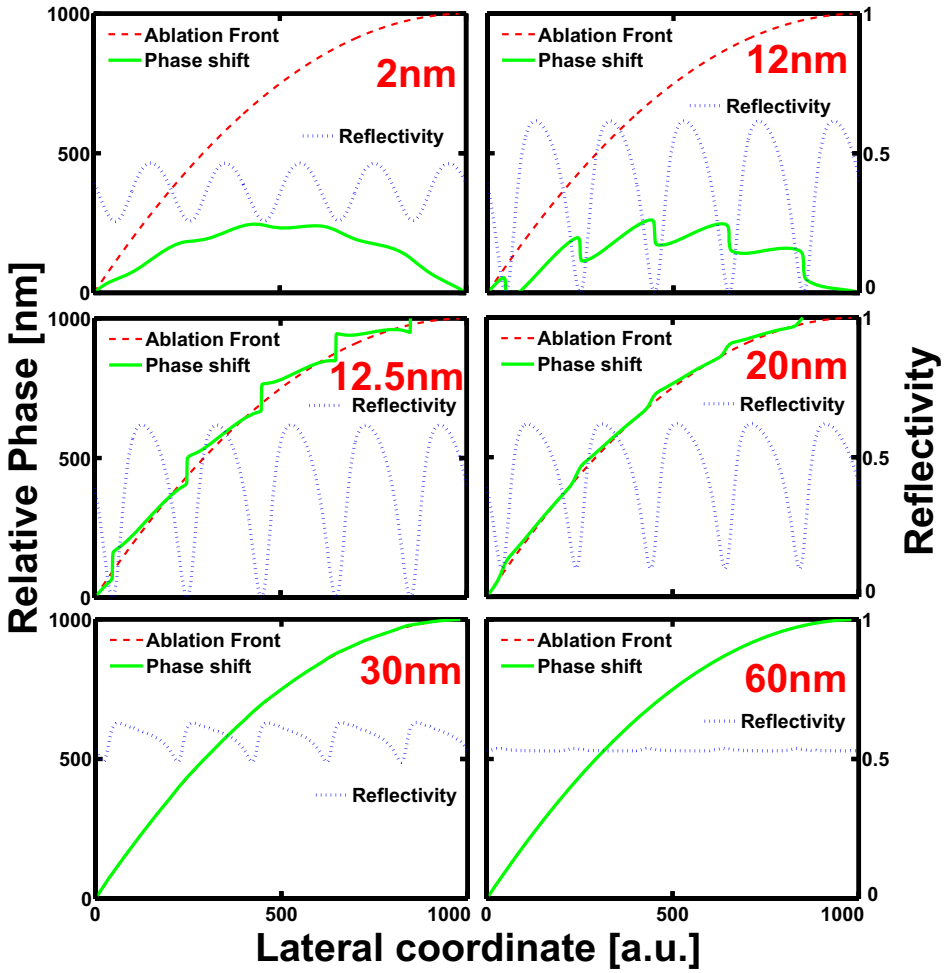

Figure 3.22: Thin film modeling of the the reflectivity and the phase shift between incident and reflected light from the ablating gold film. Shell is of a constant thickness for each graph, and it takes values in range from 2nm to 60nm, as indicated. Shell has parabolic profile (red dashed line) to resemble ablation front expansion. Maximal expansion is 1000nm. Full green line is relative phase of reflected with respect to incident pulse Blue dashed line represents total reflectivity of incident light. The horizontal axis is in arbitrary units.

rings in transient reflectivity maps. These materials present good candidates for interferometric measurements. Examples are all thick ($\gtrsim$100nm) metal films investigated in this study, except Ti which forms thin shell and in that respect behaves similarly to the Si.

3.3.2 Newton rings

It has already been mentioned that the occurrence of Newton rings represents an indication of a steep expanding front during the ablation[8] induced by femtosecond pulses for fluences low enough that heated material does not exceed the critical point during adiabatic expansion.

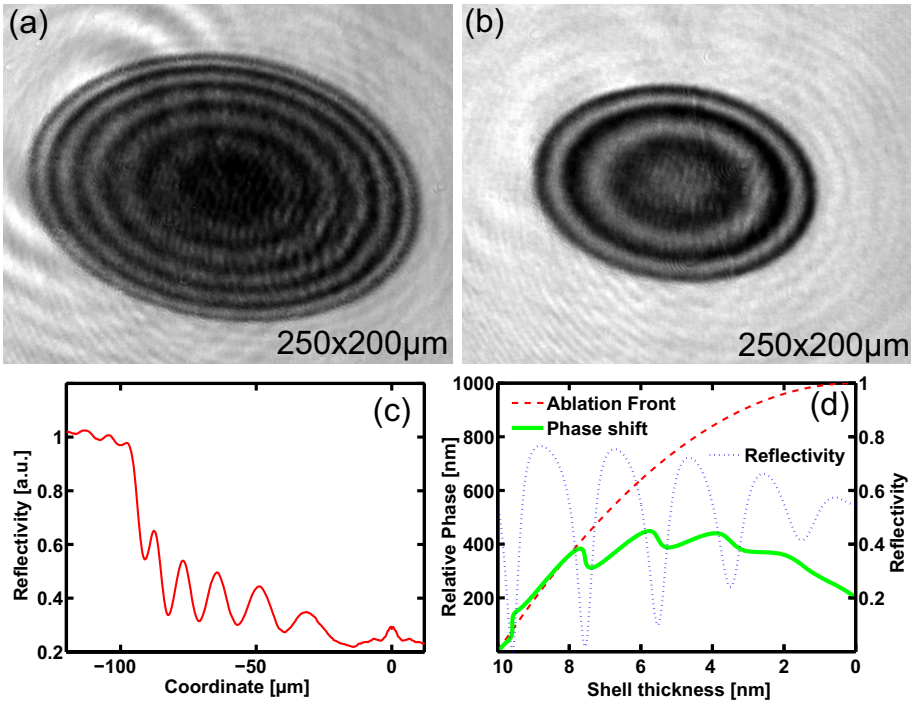

Figure 3.23: Reflectivity of the titanium film irradiated with two different fluences ($0.41 J/cm^2$ (a) and $0.27 J/cm^2$ (b)) 1.8 ns after the pump pulse. There are more Newton fringes on higher fluence shot which indicates bigger surface expansion for higher fluence shot. Graph (c) shows measured reflectivity profile from image (a) and (d) calculated reflectivity and phase profile for titanium shell of varying thickness.(See text for more information)

An example of Newton rings with good contrast is presented on figure 3.23. Images (a) and (b) show titanium sample approximately 1.8 ns after the excitation by pulses with peak fluences $2.3 \cdot F_{th}$=$0.41 J/cm^2$ and $1.5 \cdot F_{th}$=$0.27 J/cm^2$

[8] They are sufficient indication for formation of steep shell, however, they are not necessary. As it has been demonstrated, shell that is thick only reflects but does not transmit any light, and thus no N.R. are observed.

respectively. Bigger number of fringes for the shot with the higher fluence indicates that for the surface has expanded more in the same time .
In order to compare observed and calculated reflectivity, reflectivity profiles are presented in the figure 3.23 (c) and (d). The calculation conditions are the same as for the calculations in the previous section, with the exception of shell thickness. Shell thickness varies from 10nm at minimum expansion to zero at the maximum expansion. The reflectivity modulation amplitude decreases with the decreasing shell thickness in both measured and calculated profile. The phase stops following the expanding surface at approximately 7nm shell thickness. The phase shift will be discussed further in section 3.4.

The situation is not so clear with the investigated Au, Pt and Al films . Depending on the film thickness and the excitation conditions (namely the fluence and the polarization), Newton rings could not always be observed. The examples are presented in figure 3.24(a) and (b) for 33nm and 57nm thick gold films and figure 3.25(a) for 31 nm thick platinum film where the Newton rings are observed during ablation induced by femtosecond laser pulses.

Two qualitatively different situations are observed for the reflectivity modulation during the ablation of the thicker films. Here I refer to the 125 nm thick Au, 104 nm Pt and 100 nm and 400 nm Al films. First, for the lower fluences (roughly up to $2 \cdot F_{th}$) in the ablating area that corresponds to the final ablation crater, there is a clearly visible boundary of excited material, but inside this area the reflectivity is modulated randomly (i.e. no radial reflectivity modulations), and it does not change for the time delays from 200ps up to few nanoseconds.

Examples are presented for 125nm thick gold (figure 3.24(c) and (d)), 104nm thick platinum (figure 3.25(b)) and 100nm aluminium film (figure 3.26(a) and (c)).
Second, in the center of the irradiated spot, a dark area develops for higher fluences (above $2 \cdot F_{th}$). In the case of the 104 nm platinum film there is radial modulation of reflectivity inside the dark area (see figure 3.25(d)), which resem-

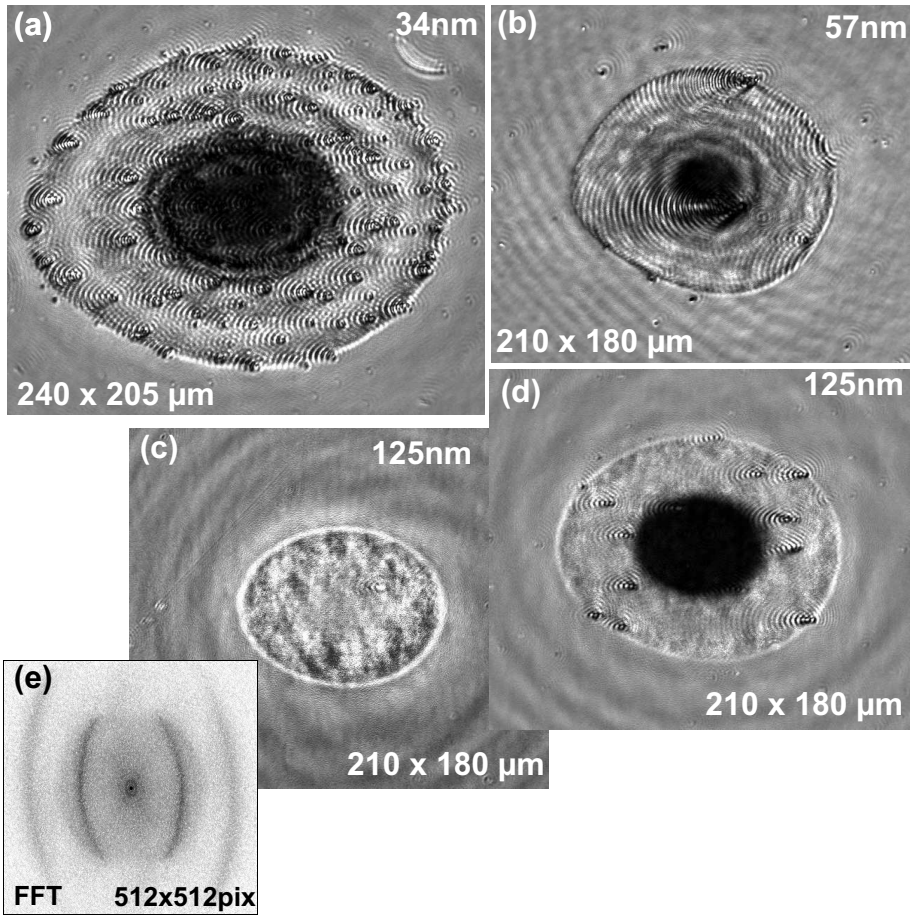

Figure 3.24: Gold films, 2.8ns after pump pulse. On (a) 34nm and (b) 57nm films irradiated with there $3.25 \cdot F_{th34nm}$ and $1.76 \cdot F_{th57nm}$ respectively there is an indication on low contrast fringes. Thick film (125nm film) shows little change in reflectivity when it is irradiated with fluence near threshold ($1.45 \cdot F_{th125nm}$)(c), while for the higher fluence ($2.35 \cdot F_{th125nm}$) reflectivity drops in central area (d) and coincides with area where complete film is removed. Image (e) is Fourier transform of image (a) and is typical for ripple pattern.

bles Newton rings. A similar, but less indicative pattern is observed for the 100 nm thick Al film (see figure 3.26(b) and (d)). The dark area that appears in center of the irradiated 125nm thick gold film does not show any sign of radial reflectivity modulation (figure 3.24(d)).

The summary of the results presented above shows that no Newton rings are observed on metal films irradiated with fluences up to approximately 50% above

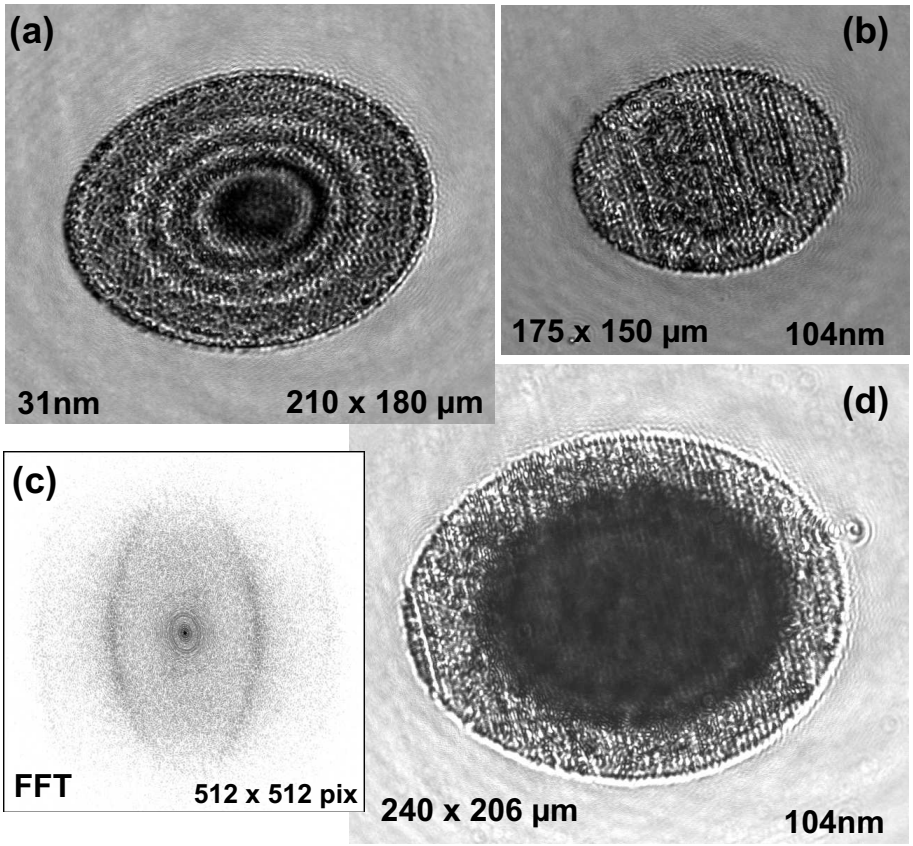

Figure 3.25: Platinum 2.8ns after irradiation with a fs laser pulse. (a) 31nm thick film, fluence is $1.9 \cdot F_{th}$; (b) and (d) 104nm thick film irradiated with $1.4 \cdot F_{th}$ and $2.9 \cdot F_{th}$ respectively. For higher fluence, reflectivity drops in the middle of irradiated spot, but there is no indication of film detachment. Fourier transform (c) of all three images shows same feature, two arcs always at same distance from center ($\sim$110 pixels).

the threshold, with the exception of titanium. Reflectivity does not change dramatically. For titanium, Newton rings of high contrast appear during the ablation. For higher fluences (100% above the threshold and more), reflectivity drops in the central area and in some cases radial modulation that can be interpreted as N.R. is observed. The question arises about the conditions for the appearance of N.R.

In a work by Anisimov *at al* [32], it has been shown that during the ablation process, near the threshold fluences, the mass of two-phase layer between shell

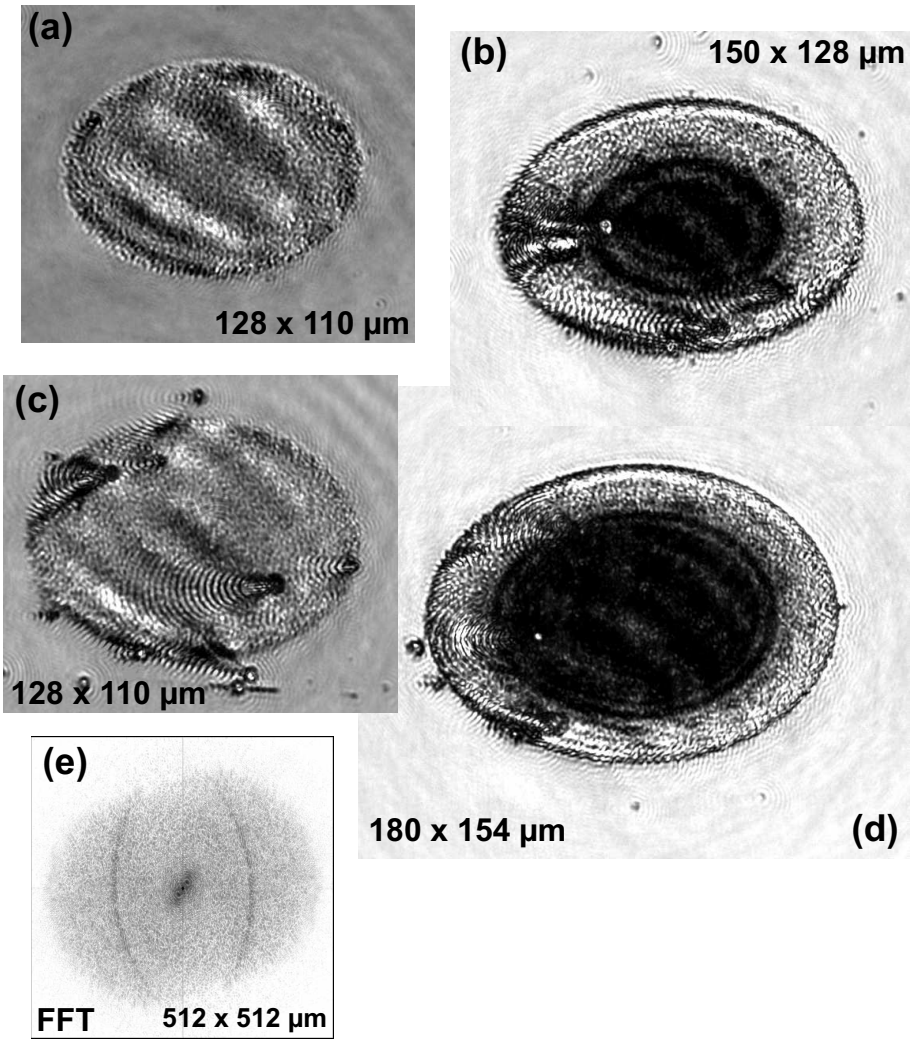

Figure 3.26: Aluminium, 100nm thick film, 2.8ns after irradiation with a single fs laser pulse. Image shows spots, irradiated with increasing fluence (a) $1.2 \cdot F_{th} = 0.43 J/cm^2$, (b) $1.95 \cdot F_{th} = 0.7 J/cm^2$ and (d) $2.42 \cdot F_{th} = 0.87 J/cm^2$. Like on Pt, there is a grainy structure, developing at same timescale as ripples. If spot contains particle of bigger size, there is a ripple formation (c) $1.3 \cdot F_{th} = 0.47 J/cm^2$, similar to that on gold. Images with higher fluence shots have enhanced contrast (10% saturated pixels), to bring out detail in the dark area. Fourier transform of images (a) and (c) reveals that ripples and grainy structure have same origin.

and non-ablating substrate is much smaller than that of the shell, and most of the ablating material is concentrated in the shell. Furthermore, it has been demonstrated that the shell thickness decreases monotonically, and that the relative mass[9] of the two-phase system increases with the incident fluence increase. The shell completely disappears at some critical fluence. Similarly, Changrui *at al* [90] report that dependance of ablation shell thickness from irradiation fluence in the molecular dynamics simulation of ablation on Nickel.
Therefore one can assume that the ablation shell thickness has some initial value, which is typically equal to the crater depth at threshold. This depth depends on the material and the nature of the ablation process, as it was discussed in Chapter 2.
Ablation craters on titanium are shallow (see Table 3.1), typically less than 10 nm, and because of that, one can expect that the flying shell will have a thickness less than this value, resulting in high contrast N.R.
On the other hand, from table 3.1 in Section 3.2.2, one can see that crater depths on other investigated materials are significantly deeper. Thicker shell which do not transmit light forms close to the threshold, and the Newton rings are absent.

For higher fluences, as the ablating shell gets thinner two processes occur at the same time:
First, at some point, when the shell gets thin enough, and as discussed in Section 3.3.1, a portion of the incident probe light will be transmitted through it and upon reflection from back surface will produce interference pattern. The thickness of the shell that causes this phenomenon depends on the optical properties of material. The expected shell thickness on the other hand can be different for the same material, depending on nature of the ablation process. For example, in the case of spallation in the middle of the film, the shell thickness directly depends on film thickness. This situation can be expected in 57 nm and 125 nm Au and 100 nm and 400 nm Al films, because of the observed crater depth

[9] with respect to the complete amount of the ablating material.

vs. film thickness ratio, which is exactly one half, as expected for the spallation of the homogeneously heated film. The drop of reflectivity in the center of irradiated spots indicate that a thick shell of uniform reflectivity is not present anymore.
Indications of this decrease in shell thickness can be seen for titanium as well. Graph (c) on the figure 3.23 shows elliptically averaged reflectivity profile from image image (a). The experimentally measured fringes decrease in contrast towards the center of irradiated spot, where fluence is highest, as expected from the results of reflectivity calculations (figure 3.23(d)).

Second, as the shell gets thinner, the amount of the ablating material concentrated in the two phase mixture, gets higher. Since the crater bottom is almost flat for most investigated materials, one can expect that for increasing fluence and a decreasing shell thickness, the mass of the two phase mixture increases with respect to that one of the shell.
The result of these two processes is that a portion of the incident light is transmitted through the shell, leading to the interference. Some of the light will also be absorbed, in the area between shell and the back surface, explaining the dark area in the center, mentioned above. This light absorption could also be responsible for absence of the Newton rings that are expected to appear for higher fluences.

3.3.3 Transient periodic structures

As already mentioned, laser induced periodic surface structures (ripples) appear on materials with surface irregularities as consequence of scattering of the incident laser wave (see Section 3.2.5). Previous studies focused on ripples as final morphological structure. Here I present observation of ripple formation in transient micrographs. Ripples appear within several tens of picoseconds after the irradiation.
Presented here are the transient ripples produced by $\pi-$polarized laser beam.

Ripples produced by $\sigma-$polarized radiation are of much lower amplitude and their spatial frequency is higher than the resolution of time-resolved microscope, and they are not observable using this technique.

Transient ripple structures on gold, take regular elliptical shape (see figure 3.24), as predicted by simple model presented in Section 3.2.5. They are grouped around surface irregularities. An example of Fourier transform of these images, presented on figure 3.24(e), reveals arc-shaped pattern, which was reported on many materials [84]. For ablation of gold free from the visible surface irregularities, reflectivity has smooth profile, noperiodic modulation, and in Fourier transform arc-shaped pattern that correspond to the ripple pattern are absent.

Contrary to gold surface, platinum and aluminium surface show, different behavior. For what appears surface free from defects before irradiation, during ablation develops reflectivity pattern that is modulated in way that appears to be random. Examples are presented in figure 3.25(b) for Pt and figure 3.26(a) for Al. However, Fourier transform of these images (see figure 3.25(c) for Pt and 3.26(e) for Al) have same frequency components pronounced, like in case of ripple pattern on gold (figure 3.24(e)), which indicates same origin. Typical ripple pattern appears on these two metals when irregularity of bigger size is present. The scattered wave has higher amplitude, which induces enhancement of the ripple pattern. An example of these two situations on aluminium can be seen on figure 3.26(images (a) vs. (c)). "Random" reflectivity modulation is present in both cases and its Fourier transforms contains arc-shaped pattern, which has enhanced intensity in case with large scattering center.

3.4 Long lasting deformations of metal surfaces exited below ablation threshold

The simple reflectivity measurements do not provide enough information to understand the ablation process, as mentioned in introduction. Using the interferometry technique, I was able to follow small movements of the surface from the moment of irradiation with fluences close to the ablation threshold, for several nanoseconds. These fluences are a result of laser intensities below ones needed for plasma formation 10^{13} W/cm^2 [91, 92].[10]

Some interesting phenomena occur in the fluence range below a mentioned plasma formation threshold. Due to the short pulses, fast energy deposition, even for moderate fluences[11] that are not sufficient to heat material up to a melting point, leads to the generation of strong pressure waves in the material. It has been observed that this leads to the expansion and retraction of the surface in an oscillatory manner. In gold (as well as on aluminium), this thermo-acoustical oscillations were observed by Maznev *at al* [93]. The characteristic rise time of the oscillations scales with film thickness, and for 100nm and 150nm gold films have values of 25ps and 50ps respectively.

However, reversible excursions of excited surface are observed close to the ablation threshold [25] that last up to several nanoseconds and have the rise time of a nanosecond. These long expansion times can not be explained by a simple acoustical model in that assumes local sound velocity as constant.

The interferometric technique described in the previous chapter allows to follow surface expansion of spot irradiated by femtosecond laser pulse. First measurements showed the behavior of semiconductors (GaAs and Si) excited by fluences a few percent around ablation threshold. As an example, repeated mea-

[10] This can be somewhat misleading. Namely, for the ablation, relevant quantity is the fluence (energy per area), since process occurs on timescales much longer than the pulse duration. On the other hand, plasma formation depends on peak intensity, and this depends on pulse duration as well as on fluence, since for shorter pulses fluence needed to reach plasma formation is lower. In mentioned references pulse duration was in 100fs range leading to fluence of 1J/cm^2.

[11] approximately 10 mJ/cm^2

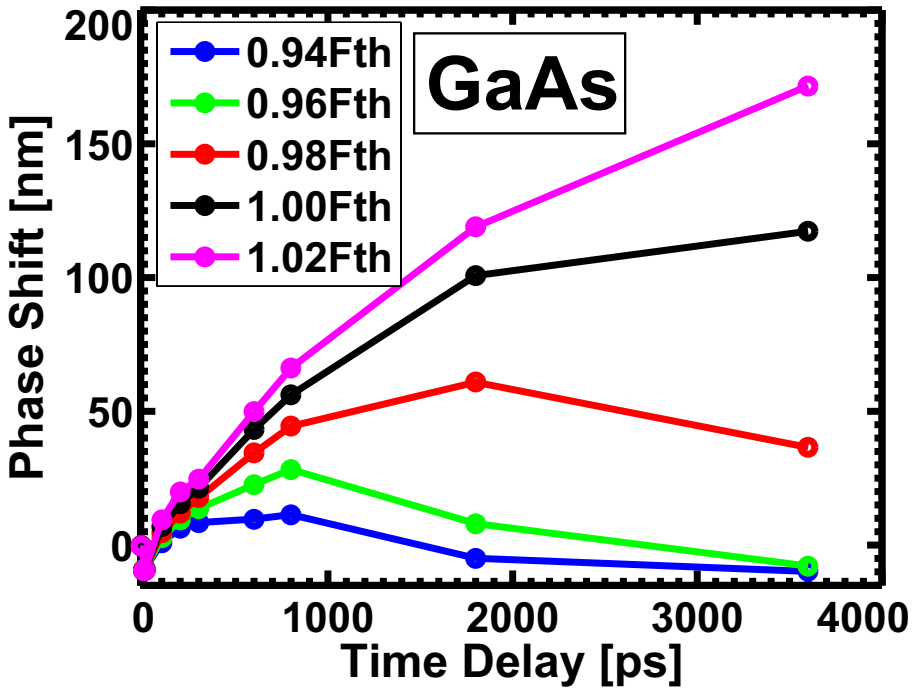

Figure 3.27: Temporal evolution of the surface expansion for GaAs irradiated with fluences close to the ablation threshold F_{th}. Each line represents expansion of the surface irradiated with one particular fluence, whose value is given in legend.

surement on GaAs presented in figure 3.27 demonstrates the already mentioned process of reversible expansion. Irradiated with fluences few percent below ablation threshold, surface of GaAs expands for a long time and finally retracts. These excursions last two to three orders of magnitude longer than expected in the simple thermo- acoustical model (nanoseconds instead 10's of picoseconds) and have a magnitude that exceeds the expected thermal expansion. The estimated thickness of molten layer for GaAs is ≈50nm while the detected surface expansion is more than 60 nm, which corresponds to a decrease in density down to a value of than 45% of ρ_{solid}.

Covalent semiconductors like Si and GaAs, which have been extensively studied so far [25], are relatively complex materials. In both materials density decreases upon melting by approximately 10%, which can be seen in figure 3.27

as a surface retraction just after the excitation within first 100 ps. Therefore, considerable heating above the melting point is required to induce a net expansion of the material. Moreover, for strong femtosecond excitations melting of these materials is caused by a $non-thermal$ mechanism [94] and it is not clear whether this has an influence on the subsequent expansion and ablation dynamics. The important question arises about the observed expansion dynamics observed on Si and GaAs for fluences just below the ablation threshold. Is it determined by the specific material properties or represents a "universal" characteristic of the material response in the vicinity of the ablation threshold? Selecting metals as samples is a natural choice to address this question because they are *simpler* than semiconductors in many aspects (i.e. linear optical absorption, decrease of density upon melting). It has been demonstrated by Miller *at al*[95, 78] that heating of aluminium and gold by fs laser pulses results in melting that is thermal in nature.

I have investigated the behavior of several metals (Al, Au, Pt, Ti) under conditions equivalent to the previous experiments on Si and GaAs, e.g. excitation fluences in the vicinity of the ablation threshold.

Figure 3.28 shows temporal evolution of the sample surface expansion. The sample is a 125 nm thick gold film irradiated with fluences few percent below and above the ablation threshold. Below threshold, the surface expands slowly, compared to the acoustical expansion and finally retracts. Above the threshold, the surface expands continuously until the final material removal and the formation of the ablation crater.

Expansion of the surface irradiated with 98% F_{th} (ablation threshold fluence) lasts for more than 4 ns and reaches more than 80 nm. Maximum expansion is reached after more than 2 ns. In the case of the 125 nm thick film, assuming that the whole layer is completely melted, and expands, the expected time for expansion in a simple thermo- acoustical model is less than 150 ps. The observed expansion induced by heating near the threshold fluence (98% F_{th}), lasts over

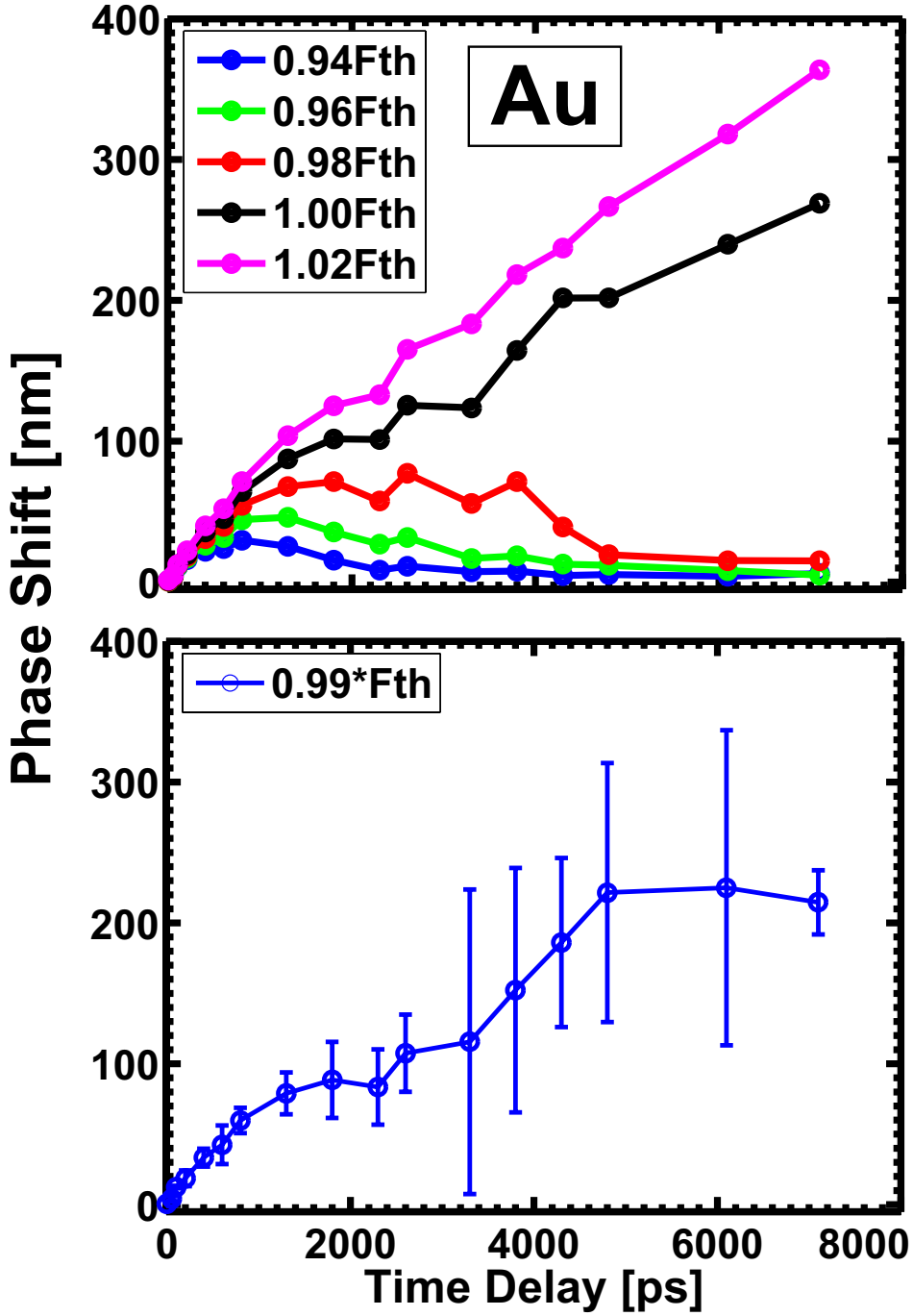

Figure 3.28: Upper graph shows the time evolution of the surface expansion for Gold film (125nm thick) irradiated with fluences close to the ablation threshold. Lower graph shows one time profile of the surface irradiated with 99% F_{th}. Error bars show uncertainty of surface position and illustrate difficulties of detecting surface position near threshold in late stages of expansion explained in subsection 3.1.3.

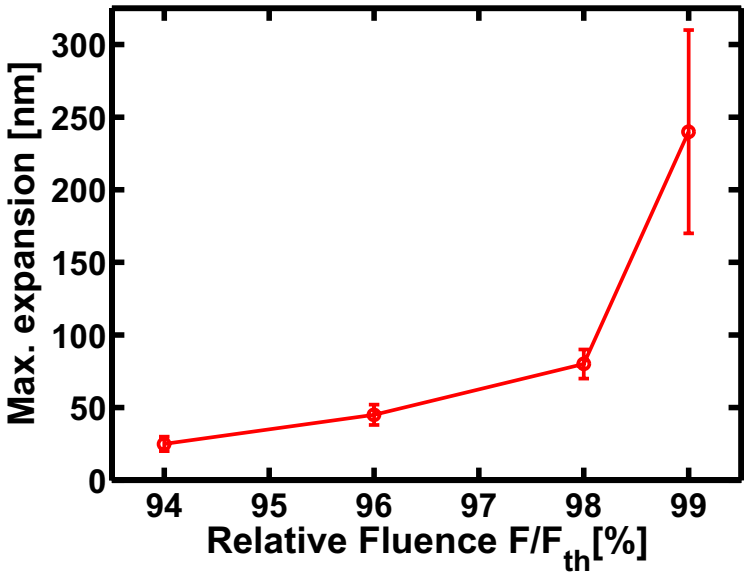

Figure 3.29: Maximal expansion of gold film for different fluences, as presented in 3.28

20 times longer.

Although the final phase maps show that for the surface irradiated with 99% F_{th} no material is removed, it is not possible to observe a retraction of of the expanded surface until after 8 ns. However, for the fluences around 99% Fth, there are large fluctuations in the detected surface expansion from pulse to pulse. As can be seen in figure 3.28 the error for the retrieved surface position is up to 100%.

Another feature of the surface expansion profiles is the fact that for small changes in incident fluence maximal expansion changes dramatically and in a nonlinear fashion. Figure 3.29 shows this clearly.

Again, as in the case GaAs, a question arises: is behavior of gold demonstration of general principle or a specific case? To demonstrate that the observed phenomena is not specific for gold, three other metals were investigated: aluminium, platinum and titanium. Results for Al and Pt are summarized in figures 3.30(a) and 3.30(b). Both investigated samples are approximately 100

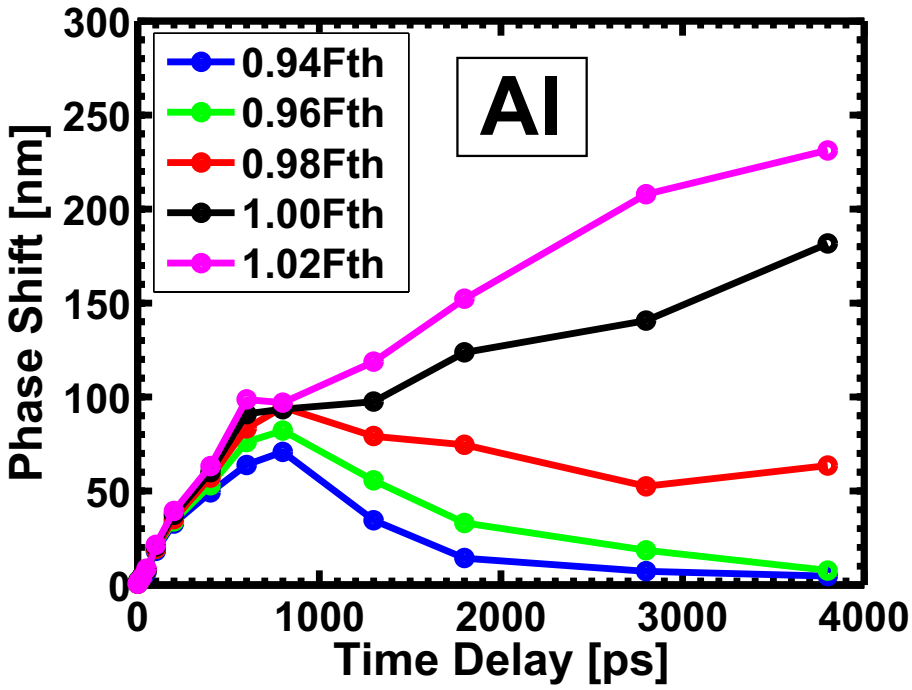

(a) Aluminium

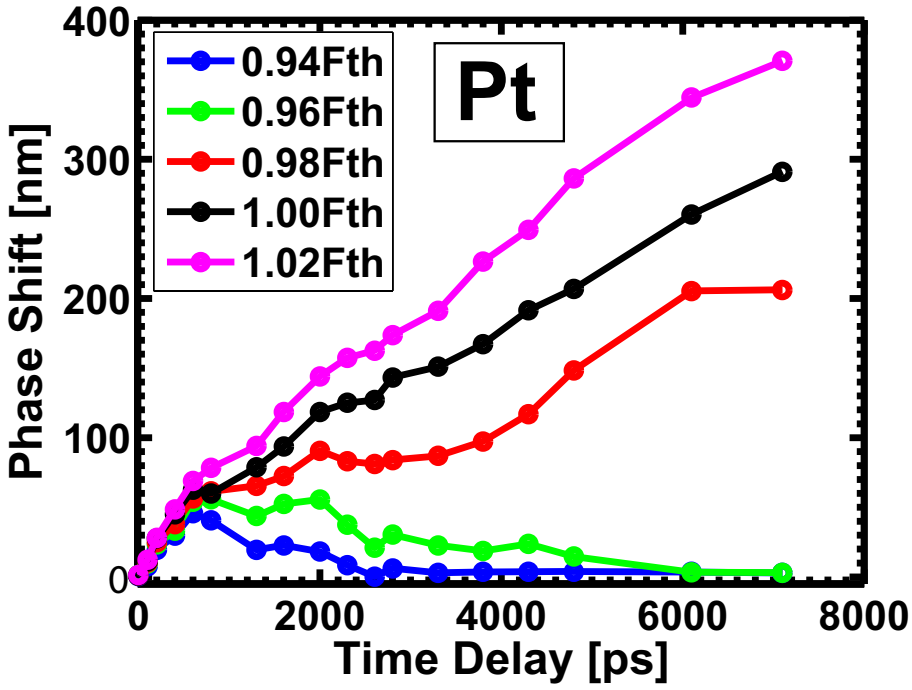

(b) Platinum

Figure 3.30: Time evolution of surface expansion for Aluminium and Platinum films 100nm and 104nm thick respectively, irradiated with fluences close to the ablation threshold. Surface expansion shows qualitatively similar behavior as one for gold and GaAs.

nm thick, and show qualitatively similar behavior. The surface irradiated below ablation threshold expands and retracts, and in both cases the time needed to reach maximum expansion is much longer than expected in the acoustical model (≈1.5ns for Pt and ≈1ns for Al).

The surface of Ti samples, irradiated with fluences near ablation threshold, was investigated in a similar fashion, but it shows qualitatively different behavior. Results will be summarized in the next section.

3.4.1 Behavior of Ti surface near the ablation threshold

Interferometrically measured phase evolution has a qualitatively different behavior than the materials discussed in previous section. In this section, results of this measurements are presented and their fit into the existing picture about ablation process is discussed. The evolution of interferometrically measured phase of expanding Ti surface, irradiated with fluences around ablation threshold is presented in figure 3.31.

Titanium phase evolution in time has three main different features to than the other investigated materials[12]. First, expansion and subsequent retraction is much faster: it occurs on timescale of few hundreds of ps rather than on few ns. Second, absolute amplitude of expansion is in the range of 20-30nm rather than few hundreds of nm. Third, and most important, is that the retrieved phase shows qualitatively no difference in expansion below and above the ablation threshold. This is important find, because expansion above threshold results in material removal (i.e. never returns back) and below it does not.

For all presented fluences, the measured phase indicates retraction after the initial expansion within a narrow time interval. After retraction it even reaches negative values. Here I would like to again make an emphasis to the fact that for both fluences above and below the threshold phase behave in a qualitatively

[12]namely, Au, Pt, Al and GaAs presetnted above.

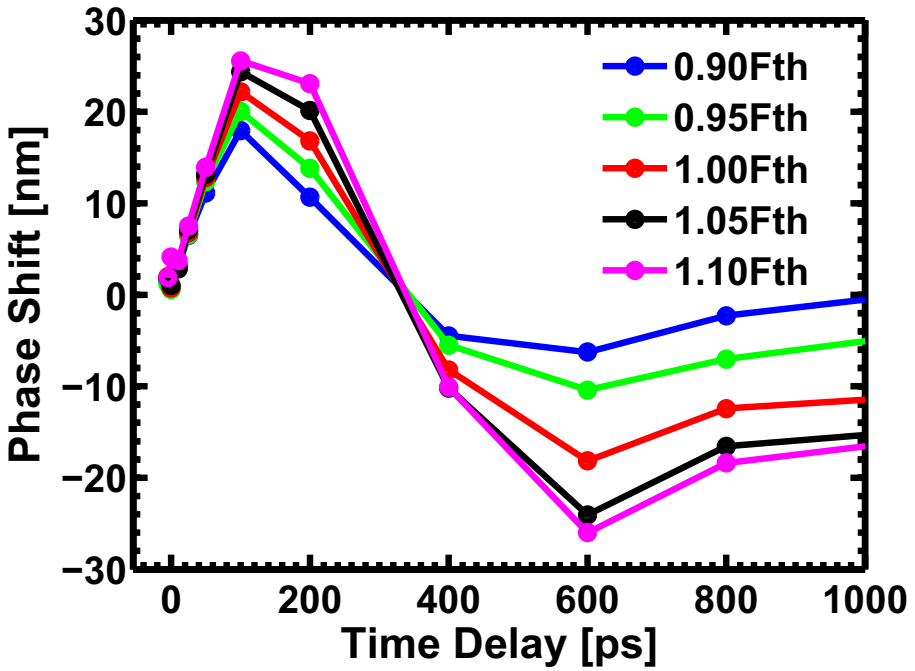

Figure 3.31: Phase shift dynamics of Titanium surface irradiated close to the ablation threshold. There is a point between 200 and 400 ps when the phase abruptly changes sign, the measured phase does not follow the ablating front.

similar fashion. This is different than measurements on Au, Pt and Al, presented above, where the surface irradiated with fluences below threshold retracts after initial expansion and surface irradiated above expands continuously for all delays and leads to material removal.

To better illustrate this process, phase and reflectivity profiles for one irradiated spot are presented in figure 3.32, for 100 ps to 600 ps time delay. Up to 100 ps phase continuously increases and at 200 ps delay time, phase starts decreasing its amplitude, and for 400 ps it has become negative. At later delays (600 ps and more) the phase profile closely follows the shape of the transient reflectivity profile.

Observed sudden drop of the phase can not be explained by the surface retraction, since it occurs both for fluences below and above the ablation threshold (expansion is expected to be non-reversible above the threshold). Note that, al-

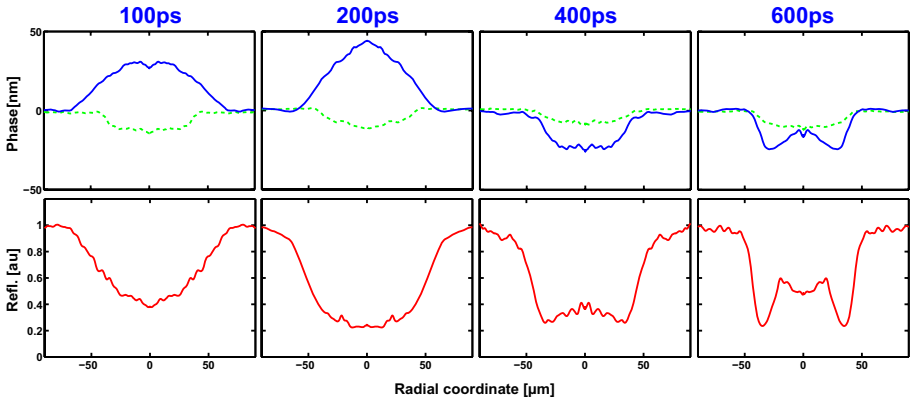

Figure 3.32: Phase (blue) and Reflectivity (red) radial profiles of Ti film irradiated with peak fluence $1.2 \cdot F_{th}$ for different delays. Between 200 and 400 ps phase changes sign, and follows shape of reflectivity profile, and not ablation front. Green dashed line represents final crater profile.

though transient phase has the somewhat unexpected behavior, the final phase shows typical ablation crater, indicating that the ablation mechanism is similar to that of the other materials.

The shallow craters found on Ti[13] and high contrast Newton rings indicate that while the ablation shell is formed, it is also very thin compared to the other investigated materials mentioned here.

Section 3.3.1 demonstrated that the relative phase of the reflected light does not represent the shell surface when the shell is too thin (typically ∼10 nm). A good example is titanium, for which figure 3.23 illustrates that for shell thicknesses between 7nm and 8nm the phase of reflected light does not represent the ablation front anymore.

In work by Temnov [25], it was observed that due to the thin ablating shell, interferometric technique was not capable to accurately follow the ablating front for Si. Still, for fluences below threshold this material shows behavior analogous to one observed on GaAs, and here reported behavior on Au, Pt and Al, for which measured phase shows good agreement with expected surface expansion. In that sense Ti represents an even more extreme case than Si, because even

[13] as it can be seen from figure 3.32 and table 3.1

below the threshold the expanding surface can not be followed.
This drop of the phase, even below threshold indicates that thin shell is formed even for low fluences, which indicates the spallation of material even below threshold.

3.4.2 Conclusions on long lasting deformations of metal surfaces

In this section two models explaining material behavior close to the ablation threshold are presented.
The first is the thermo- acoustical model, describing expansion below threshold, and second is the hydrodynamics model that is used to describe continuous expansion of hot liquid above threshold.

It is considered that the film is homogenously heated in the case of Gold, because of the fast electron transport (in range of 100fs for 100nm film [42]), . Homogeneously heated film, on a hard substrate, is allowed to expand in one direction.
In the previously mentioned work, Maznev *et al* [93], used thermo- acoustical model for describing surface displacement. In sucha a case formula (3) describes surface displacement as a function of time:

$$u(z=0,t) = \frac{3\beta B}{\rho v_L^2} \int_0^{tv_l} T_l(z', tv_l - z')dz' \tag{3.22}$$

If I assume constant temperature along film thickness, equation 3.22 can be further simplified to:

$$u(z=0,t) = \frac{3\beta B}{\rho v_L^2} tv_L T_l \tag{3.23}$$

The longitudinal speed of sound in gold is v_L=2030m/s, the linear expansion coefficient β=1.4x10^{-5} 1/K and bulk modulus B = 220GPa [39]. The lattice temperature rise is estimated to the T_l=1090K at the threshold fluence F_{th}=0.85J/cm^2, assuming that for reflectivity R=0.96 and a film thickness of

d=125 nm energy is homogeneously spread over the whole volume.
For these values, expansion velocity taken as $v_{exp} = \frac{u(z=0,t)}{t}$, and has value of v_{exp}=161m/s. For this velocity, the maximum observed surface expansion of 100nm would be reached in t_{max}=300ps, which is almost ten times less than measured time.
Fluences in range 10-50 mJ/cm^2 induce linear acoustic perturbations [93]. The rise time for this expansion is in range of 100ps for 2.5μm thick gold films and down to 25ps for 100nm. For Al films and stainless steel bulk samples this time is even shorter [93]. This confirms that simple calculation presented above is an overestimate.
In this model, at maximum expansion, surface velocity simply changes sign and the surface starts retracting. This is in agreement with experimental results for low fluences, but when fluences are close to ablation threshold, the expansion shows different behavior.

The hydrodynamic model for behavior above ablation threshold was described by Sokolowski *et al* [14, 18]. The initial stage of the expansion can be described as one dimensional rarefaction wave which propagates inside the material. The fluid flow velocity at vacuum boundary is approximated by:

$$v_{exp} = c_0 \ln(\frac{\rho_1}{\rho_0}) \tag{3.24}$$

The initial sound velocity $c_0 = v_L$, ρ_0=19.3 g/cm^3 is initial density and ρ_1=15.6 g/cm^3 is density at binodal, reached by isentropic expansion (this value is estimated from equation of state diagrams for Au [38]). In this model, v_{exp}=687 m/s, and is clearly an even bigger overestimate. The expansion time would be t_{max}=73ps.
This model is in agreement with experimental results for fluences above the ablation threshold[14], but it can not explain reversible behavior below threshold.

[14] an example can be seen on figure 3.33, which presents surface expansion on gold irradiated with fluences slightly above the threshold.

In the case of gold, as already mentioned, surface irradiated with 98% F_{th} expands to 80nm and reaches this expansion after 2ns. This gives average expansion velocity v$\cong$ 40 m/s. Similarly for 99% F_{th}, estimating time to reach maximum expansion to 6 ns and maximal surface expansion to 250 nm, yields the average expansion velocity of v$\cong$ 40 m/s.

Going back to the acoustic model ($v_L^2 = 3\frac{1-\nu}{1+\nu}\frac{B}{\rho}$, where ν is Poisson ratio), the surface displacement can be rewritten from equation 3.23 as $u_{exp} = 3\beta\frac{1+\nu}{1-\nu}v_L T_l$. From this equation, the expansion velocity depends directly on the material sound velocity. Low expansion velocities indicate decreases of local sound velocities in the expanding material an order of magnitude smaller than the unexcited material.
Sound velocity in thermodynamics is defined as $c_s = \sqrt{\frac{\partial p}{\partial \rho}}_S$. As already mentioned, when a material enters two phase region (crosses the binodal), the sound velocity jumps to a very low value. In the two phase mixture, the pressure remains almost constant for large variations in density, while portions of the material change their aggregate state (gas-liquid) on microscopic scale. Mathematically, this means that partial derivative goes to zero and physically that sound velocity has a low value.
Following this reasoning, one possibility is that material below the ablation threshold transiently changes to the two phase composition, which has the low sound velocity. The jump in the sound velocity is responsible for formation of the liquid shell in hydrodynamic model of femtosecond ablation, as has been demonstrated [17, 16, 37].

The large transient surface expansions around threshold indicate significant decrease in density of expanding material. The surface irradiated with the 98% of threshold fluence expanded for more than 80nm, resulting in decrease of the average material density by more than 40%. The question arises weather the hot material that expands along isentrope can reach these densities and still stay homogeneous. For this to happen, material would have to pass close or

above the critical point, and fluences needed to push the material to this region are several times higher than the threshold fluence [37].

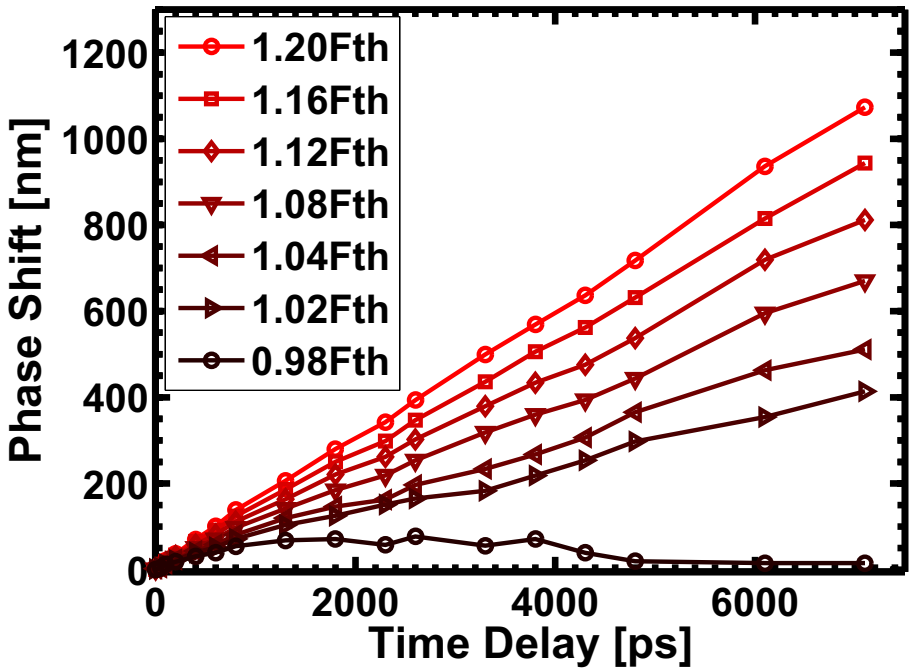

Figure 3.33: Expansion of gold film, including fluences above ablation threshold, up to 120% of F_{th}. In this range, ablation front moves with constant velocity, which scales linearly with laser fluence.

Chapter 4

Ablation by femtosecond XUV pulses

4.1 Why use XUV radiation for ablation excitation

Using ultrashort pulses of optical radiation to induce single shot ablation introduces some difficulties. At high intensities, absorption can be largely nonlinear and in general not known. This leads to uncertainty of deposited energy. Second difficulty lies in the fact that for the same reason, the depth of excited layer is not generally known and it can be only roughly estimated from ablation craters. On the other hand, there are several advantages in using short wavelength radiation, with photon energies high enough to directly ionize material, as an excitation for ablation. For example, the range of $6-100$ nm corresponds to the range of $12-207eV$ in photon energy, which is above the ionization potential for most elements. Using ultrashort intense radiation in this range of wavelengths induces a high degree of electron excitation which in turn reduces nonlinear absorption mechanisms, such as free carrier absorption and multi-photon absorption, which could change self-reflectivity as in the case of optical excitation

[27, 28]. This allows a good estimate of the energy deposited in the sample.
For the photon frequencies higher than the plasma frequency, but lower than the frequency of the inner shell absorption edge, the absorption depth for some materials can be rather long. In the case of the presented materials, Si and GaAs, the absorption depth is 257nm and 67nm respectively [96], at 32.5nm wavelength. The reflectivity at angles of incidence up to 40° does not exceed few percent [96], so most of the incident energy is absorbed in the material. This provides knowledge about the amount of energy absorbed into the material, as opposed to excitation by optical fs radiation, where this is not always known.
Although 250nm is not a particularly large absorption depth, it does not change with intensity, which is not the case for excitation with optical radiation at intensities in the range of $10^{14}\mathrm{W/cm}^2$.
As a consequence, irradiating samples with XUV pulses gives the opportunity to create well defined excitation conditions over relatively large volumes, as compared to femtosecond optical pulses.

Results of the first experiments, on the interaction of ultrashort high intensity ($10^{12} - 10^{14}\mathrm{W/cm}^2$) XUV pulses with solid surfaces, which had been performed at FLASH (FLASH stands for "F"reie-Elektronen-"LAS"er in "H"amburg or the equivalence in other languages), are presented here. Microscopic optical imaging with picosecond time resolution is used in an XUV-pump/optical probe configuration, to follow the dynamics of short-pulse XUV-induced phase transitions and ablation. The time-resolved measurements were supplemented by a characterization of the permanent structural modifications of the irradiated surfaces. A comparison with femtosecond optical excitation reveals distinct differences in the material response which are attributed to the absence of absorption nonlinearities and the increased penetration of the XUV light in the materials (Si and GaAs) discussed in this study.

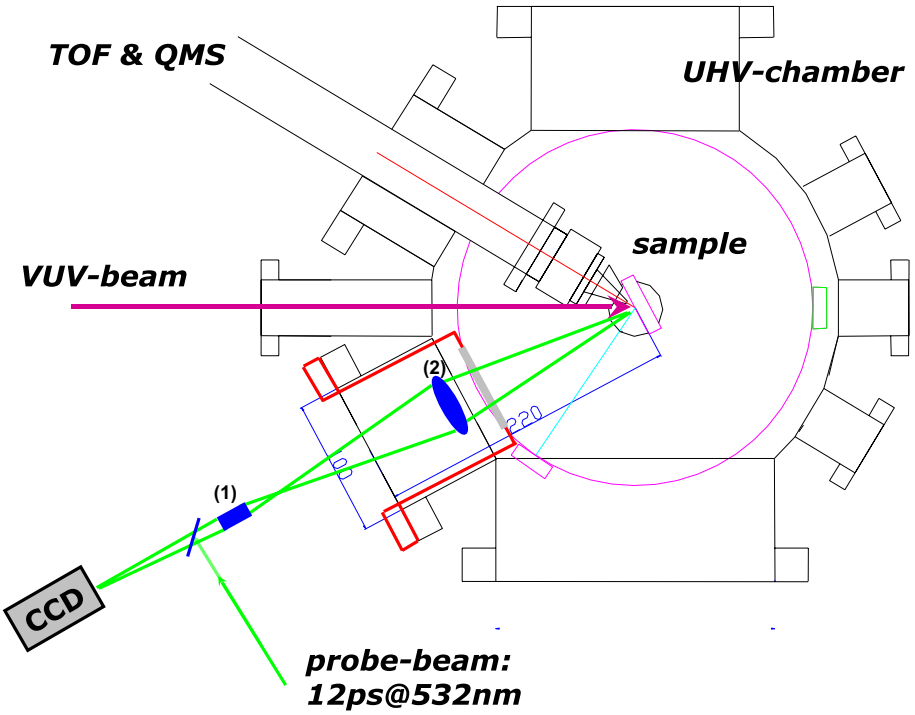

Figure 4.1: Scheme of the experimental setup, as it appears from above. The VUV beam (purple; pulse duration τ =25fs and wavelength λ =32.5nm) hits sample at approximately. 35° and the probe beam (green; τ =12ps λ =523nm is normal to the sample.

4.2 Experimental setup

Experiments were performed at beamline BL2 of the FLASH facility with the FEL operating at a wavelength of 32.5 nm and a pulse duration of approximately 25 fs (full width at half maximum). The XUV beam is focused to a spot size of 20 μm, using a grazing incidence carbon-coated elliptical mirror. Average pulse energies were 10−15μJ and thus fluences higher than 3.5 J/cm^2 (10^{14}W/cm^2) were available.

A scheme of the experimental setup is presented in Figure 4.1. The samples were mounted in an ultrahigh vacuum chamber equipped with a motorized high precision, multiaxis manipulator. A time-delayed optical probe pulse of 12 ps duration and a wavelength of 523 nm serves as an illumination in an optical mi-

croscope. The probe pulse is synchronized to the FEL pulse with an accuracy of approximately 1 ps. The optical microscope is mounted outside of the chamber, in the open air, and it images the sample surface, through the separate flange with a glass window, outside of the vacuum chamber. The flange where VUV beam enters the chamber and the flange for the optical microscope are positioned at an angle of 35°, with respect to each other. The microscope is used as an illumination source as well as a magnifying tool and, in this geometry, the sample has to be normal to the microscope objective axis. For that reason the sample is irradiated by the XUV pulse at an angle of incidence of 35°.
The optical microscope is similar to the system described in section 3.1.2. The same objective is used, but its working distance (17mm) was not long enough to image the sample surface outside the chamber. For that reason, relay imaging is utilized, and an additional objective (LOMO OKS-1-80-1) is used to image the sample surface from outside of the vacuum chamber. Since the focal distance of the relay imaging objective was still not large enough to image the sample surface outside of the chamber, a special inlet was built inside the flange, to reduce distance from sample surface to objective (red flange on figure 4.1). The relay objective was mounted in the inlet, so that the sample was in its focal plane.
The relay objective has a calculated theoretical resolution of 3.1μm[1], and the microscope of 2.1μm. The relay objective was adjustable along the horizontal and vertical axis, but not along azimuth (φ) and elevation (θ) angle. This limited adjustment and resolution to approximately 5μm.
This setup allows the evolution of the reflectivity of the irradiated surfaces to be measured with temporal resolution limited by probe pulse duration (12ps) and spatial limited by the imaging optics (5μm).

The elliptical mirror used for focusing the FEL beam has a fixed position in the direction of the beam propagation. The focus position of the FEL beam with respect to the sample has to be adjusted by moving the sample. This was

[1]Focal distance of this objective is 80nmm and lens numerical aperture is 0.167.

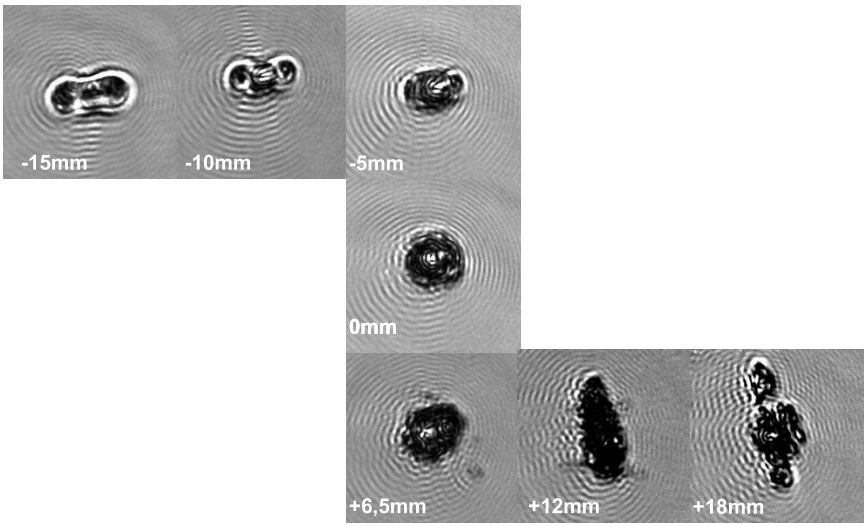

Figure 4.2: Damage on the Si sample, used to optimize the focal spot, whose shape depends on the relative chamber position with respect to focusing mirror. Picture marked 0mm represents best focus.

achieved by moving the whole chamber around the focus position. To find the focus position, the Si sample was irradiated with several pulses, until visible damage was observed (see figure 4.2) and position of the chamber was changed along FEL beam till optimum focus spot was observed. Due to astigmatism of the elliptical mirror, the beam deforms to an ellipse outside of the focus. The best focal position is determined at the place where the beam has the most circular shape.

4.3 Time evolution of reflectivity on Si and GaAs

As an example of the time-resolved measurement, figure 4.3 shows a sequence of time-resolved micrographs from a Si surface irradiated with a fluence of 2.5 J/cm^2. This fluence corresponds to about 25x the melting threshold F_m=0.1 J/cm^2 and 6.5x the ablation threshold F_{ab}=0.38 J/cm^2 (the thresholds for melt-

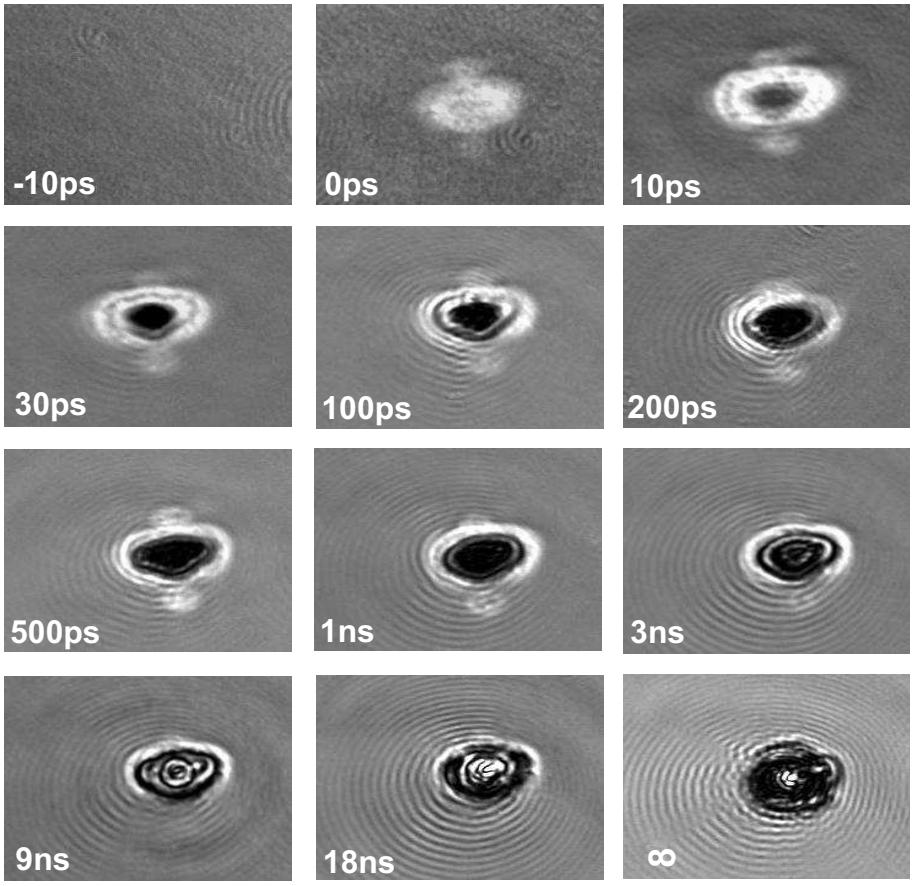

Figure 4.3: Time-resolved micrographs of a silicon surface irradiated with a sub 50fs XUV-FEL pulse (λ=32 nm) and a fluence of 2.5 J /cm^2; frame size is 120x80 μm^2.

ing and ablation have been determined using the technique introduced by Liu [77]).

For very short delay times we observe a pronounced increase of the reflectivity. The increase is more than twice of the initial value of unexcited Si. Similar behavior has been observed in the case of femtosecond optical excitation [97, 26] and attributed to nonthermal melting [98]. Although the temporal resolution in the experiment discussed here was limited by the probe pulse duration to 12 ps, the observed increase of the reflectivity most likely occurs on a subpicosecond time scale and is similarly related to an electronically induced phase transition.

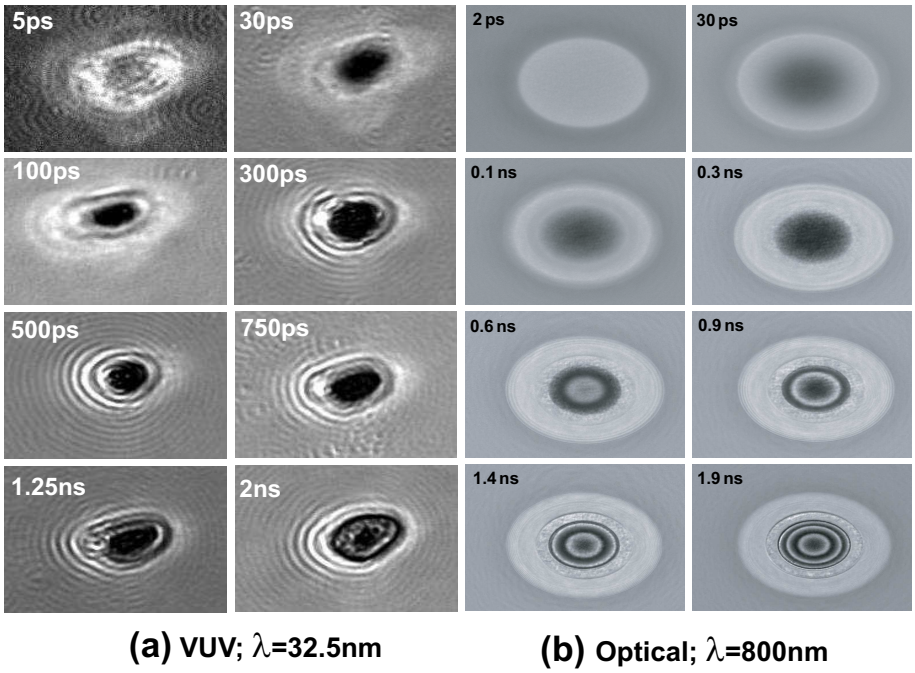

Figure 4.4: GaAs, comparation of reflectivity for irradiation with (a) VUV and (b) optical excitation (200μm x 150μm). (Source for (b) Temnov 2004 [25])

As early as 10ps after irradiation, the center of the spot shows a drastic decrease in reflectivity. This decrease can be explained by material dilution, because for such a high incident fluence one can expect early fragmentation of the ablating substance[21]. For times up to approximately 1 ns after the excitation, the relative size of the low reflectivity region increases while the size of the molten area (high reflectivity) remains unchanged. On a nanosecond time scale, the high reflectivity area decreases its size, and this indicates resolidification of the material at the periphery of the spot where the excitation fluence was low. Approximately 3ns after excitation, an additional, circular feature appears in the center of the spot. The diameter of this structure increases with time as can be seen in the frames from 3 to 18 ns. Even after 18 ns ablation has not come to an end, and the irradiated surface has not reached its final state. The final state of the irradiated spot can be seen from the last frame of the series, and this was taken a few seconds after the irradiation. The ring-like periodic modulation of

the reflectivity observed outside the laser-excited area is an artifact caused by the limited spatial resolution (3−5 μm) of the microscopy setup.

As an comparison, similar evolution of reflectivity, observed on GaAs is presented in figure 4.4, and is compared with the evolution of reflectivity changes induced by an optical λ=800nm pump beam, and observed with femtosecond resolution (τ=100fs). The excitation fluences in both cases were in the range of 0.5 J/cm^2. The two main features are the initial increase in reflectivity and the subsequent decrease in the center of the irradiated spot. Newton rings that appear in the case of optically excited material are not visible in the case of VUV radiation. There are several reasons for this. First, optical resolution is so low and the spots are so small, that even if there were fringes, they most probably would be masked by diffraction artifacts. Still, considering linear absorption, one can assume that material is heated with some (almost exponential) profile and thus, according to the model presented in chapter 2, tensile waves in the material would induce the rise of the shell whose thickness decreases with increasing fluence. By improving resolution, increasing the focal spot size and fluence range, one would expect to observe fringes.

4.4 Morphologies of craters on Si and GaAs

Although the general direction of FEL induced ablation on Si and GaAs can be concluded from time-resolved reflectivity studies, the question is what is the structure of artifacts produced during this process, since this can not be answered from low resolution micrographs.

High resolution micrographs[2] taken with a Normaski interference microscope give better insight into the structure of the ablation craters. Typical examples for Si and GaAs are presented in figures 4.5 and 4.6 respectively. The images in figure 4.5 show micrographs of craters produced on Si for different XUV pump

[2]optical resolution is better than 1μm

fluences. The graph shows the crater depth profiles along the white dashed lines in images (b), (c) and (e). The depth profiles were measured by optical interferometry and represent the crater depth along the white-dashed lines.
For Si, at the lowest fluence, 10% above the ablation threshold, an ablation crater with a well-defined boundary is formed. The crater depth increases with increasing fluence. A further increase of fluence gives rise to an additional feature appearing inside (for F=1.5 J/cm^2, also not pictured). For the two highest fluences (F_1=2.5 J/cm^2 and F_2 >5 J/cm^2) the size of this secondary feature becomes even larger than the actual crater size. The visual impression suggests that the ejection of molten material is the responsible mechanism. This interpretation is supported by the time-resolved data which suggest that the expanding circular feature visible in the nanosecond range is due to the process of melt expulsion.

To better illustrate this process in figure 4.7 temperature profiles are presented for material heated to two different depths. For both cases heating is induced by ideal linear absorption of radiation. The absorption depths are 16nm and 116nm, which illustrates nonlinear absorption of optical and linear absorpiton of VUV radiation[3]. The laser pulse shape is assumed to be Gaussian in both cases, and the peak fluence is chosen so that the maximal temperature reached in the center of the irradiated spot is the same in both cases.
In figure 4.7 two temperature/pressure profiles are shown, for the absorption depths of 16nm and for 116nm, respectively. The maximum temperature is in the center of the irradiated spot on the surface. The fluence in both cases is chosen so that at this spot the temperature is the same.
Due to linear absorption , the temperature decreases exponentially with increasing depth. At the initial moment of the expansion, the pressure is proportional to the temperature. In the case of a larger absorption depth there are greater lateral pressure gradients, that can induce the movement of material sideways. For optical lasers such behavior is well known in the case of cw- and long-pulse

[3]Optical radiation is of 800nm wavelength and VUV of 32.5nm.

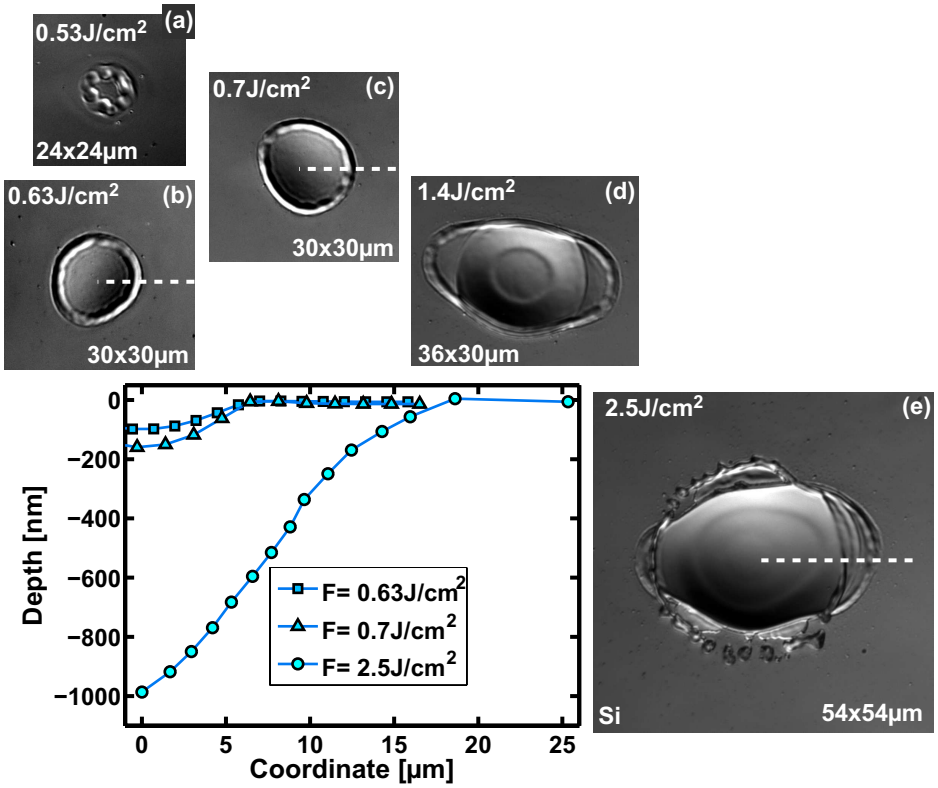

Figure 4.5: Micrographs of permanent structural modifications on a Si surface after irradiation with XUV pulses of increasing fluence. Depth profiles, as obtained from interferometry, along the white dashed lines of the ablation crater for three different fluences. Images are to scale.

irradiation and is attributed to the recoil pressure of the ablating material [99]. However, this "piston effect" requires significant lateral pressure gradients compared to the pressure gradient normal to the surface. It is usually not observed for ultrashort-pulse irradiation (only for very tight focusing conditions [1]). For short optical pulses the energy deposition depth (<100 nm) is much smaller than the typical lateral dimensions ($\approx 10-100\mu$m), making the pressure profile essentially one dimensional along the surface normal.

The observation of the piston effect in our experiment therefore provides evidence that the energy deposition depth and the lateral pressure gradients are larger in the case of XUV irradiation despite the short-pulse duration and the

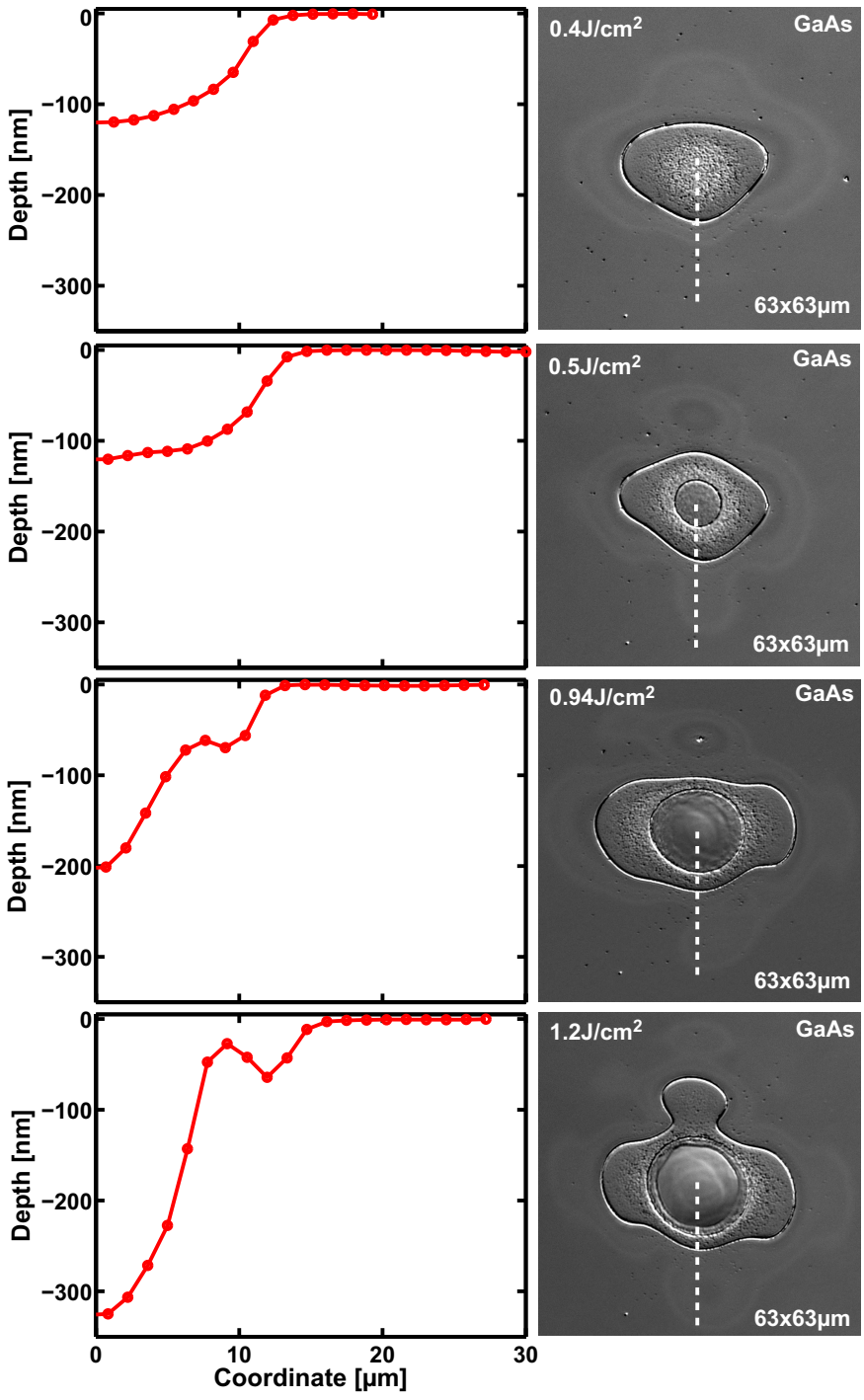

Figure 4.6: Right column: Micrographs of permanent structural modifications on a GaAs surface after irradiation with XUV pulses of increasing fluence. Left column: depth profiles, retrieved from interferometry along white dashed lines, for presented micrographs.

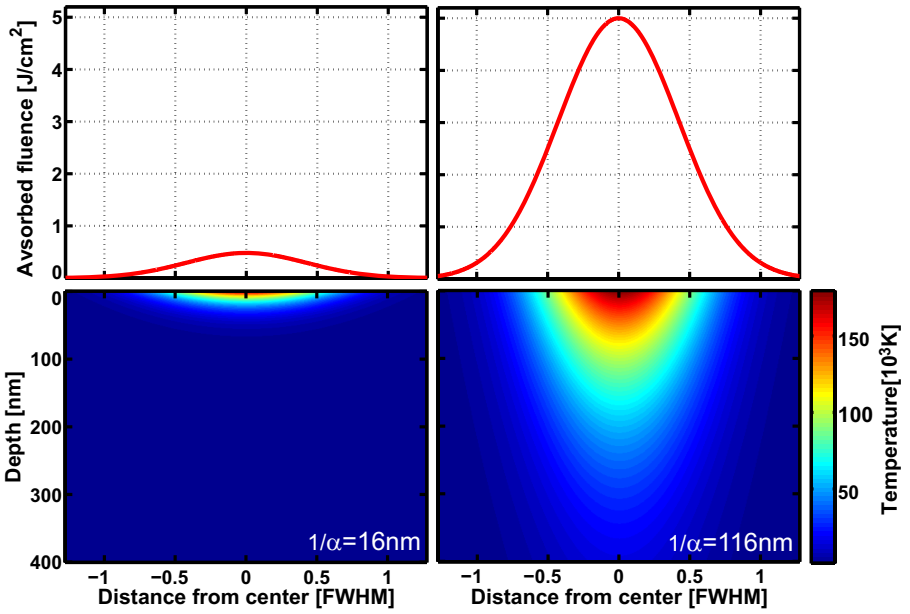

Figure 4.7: Piston effect: Calculation for Si, for two different absorption depths (16nm and 116nm). Fluence has value needed to reach the same maximal temperature at the surface (∼180kK). In the case of a longer absorption depth, deeper in the sample higher temperatures are reached. This results in higher pressures inside the depth of the sample, the pressure distribution is not one dimensional anymore, considerable lateral pressures can eject the material sideways and not only upwards.

weak focusing conditions. As a consequence, rather deep craters (almost 1 μm at F=2.5 J/cm^2−see bottom part of figure 4.5) are formed.

Depth profiles on Si and GaAs presented above confirm qualitatively similar behavior for both materials. For lower fluences a relatively flat crater is formed, whose depth weakly increases with fluence. For higher fluences (typically 3·F$_t h$) there is a sudden decrease in crater depth which scales with fluence in a different manner than the crater shape.

It is quite instructive to directly compare morphology of the craters produced by femtosecond optical pulses and femtosecond XUV pulses of similar fluence. Two examples are presented in figure 4.8, for the case of GaAs irradiated with a fluence of F=1.5 J /cm^2. The left column shows a Normarski micrograph (a) and a depth profile (c) in the case of optical excitation with 100 fs pulses at 620

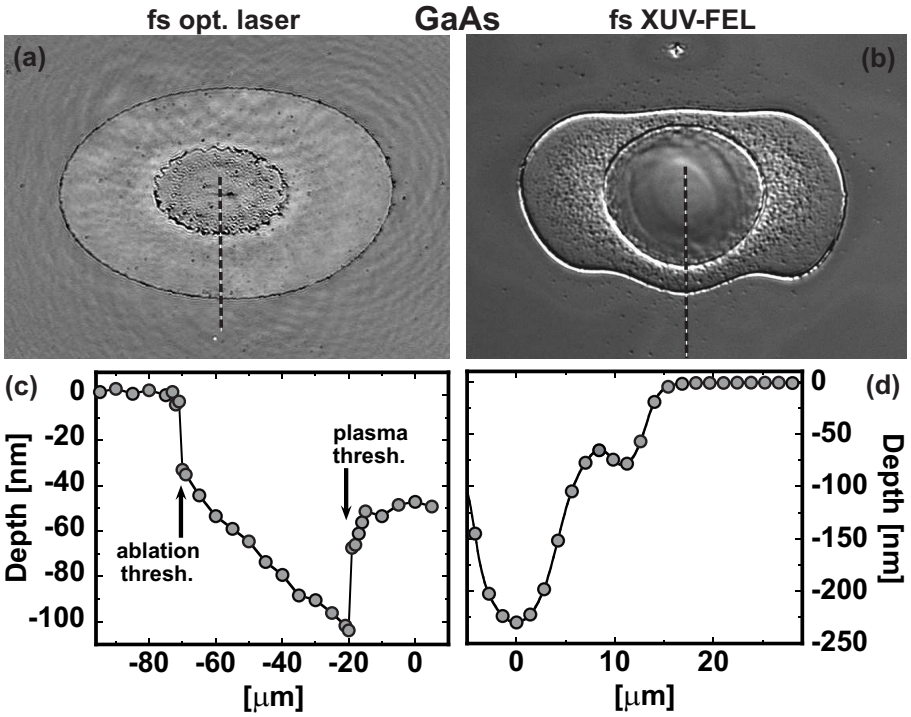

Figure 4.8: Comparison of ablation craters on GaAs induced by femtosecond optical excitation (left column) and femtosecond XUV irradiation (right column). The upper part shows optical micrographs; the lower part shows corresponding depth profiles (obtained from interferometry) along the blackdashed lines. (Source: Stojanovic *at al* [100])

nm wavelength. The right column shows corresponding data for femtosecond XUV excitation at 32.5 nm.

In both cases the craters exhibit an outer crater boundary marking the ablation threshold and a secondary feature inside the main crater. Despite some similarities in their visual appearance, a comparison of the depth profiles reveals important differences.

For the optical excitation an ablation crater with steep walls is formed indicating a very sharp ablation threshold. The crater depth at the threshold is approximately 40 nm and it increases to more than 100 nm towards the center of the spot (higher fluences). However, near the center a sudden decrease in depth is observed. It occurs at a fluence of 1.2 J /cm^2 and can be attributed to optical

breakdown at the surface and the formation of a high density plasma during the pulse. Multi-photon and avalanche ionization lead to strong nonlinearities in the absorption process and a drastic decrease of the effective absorption depth. All the energy is deposited in a very thin layer close to the surface. Due to the high energy density in this layer, the material is rapidly carried away from the surface leaving behind less-excited material underneath which does not ablate. Consequently, a much shallower crater is formed upon crossing the breakdown threshold.

In the case of XUV excitation the crater exhibits a completely different depth profile. Close to the threshold the crater depth is comparable to the optical excitation case, while for higher fluences (closer to the center) a drastic increase in depth is observed. The second feature discernible in (b) corresponds to the wall-like rim delimiting the inner crater region. In this region the crater surface appears very smooth. In analogy with the case of Si discussed above, we attribute the observed behavior to the process of melt ejection (piston effect). We conclude that evidently no threshold like increase in absorption and no reduction in the energy deposition depth takes place at higher intensities. Short-pulse XUV irradiation therefore, permits a smooth and controllable variation of the excitation density to go continuously from an electronically excited solid to a high density, high temperature plasma state.

4.5 Conclusion on XUV ablation

In conclusion, we have presented time-resolved reflectivity measurements of solid surfaces irradiated with intense short-wavelength femtosecond light pulses from an XUV free electron laser supplemented by a postmortem analysis of the induced permanent structural surface modifications. The experimental data confirm the expectations of an increased energy deposition depth and the absence of absorption nonlinearities. Future experiments with improved temporal and

spatial resolution will allow us to investigate the dynamics of the rapid phase transformations which are the result of electronic relaxation after excitation with high energy photons.

Chapter 5

Conclusions

I investigated the behavior of different materials irradiated with intense femtosecond radiation with wavelengths in near infrared and XUV range and fluences close to the ablation threshold. Expansion of the surface irradiated with optical radiation shows distinctively different behavior for fluences below and above the ablation threshld. Few percent below the threshold, large long lasting expansions of material are observed for a wide range of materials. Contrary to the expansion induced by low fluences, these expansions can not be explained by the existing thermo-acoustical model, and they give validation to models of pressure driven spallation mechanism of material decomposition.

Interferometric measurements are complemented with time resolved microscopy (evolution of reflectivity) and final crater morphology, by interferometric and Normaski microscopy. These measurements, together with thin film modeling of ablation front reflectivity yield an insight into the conditions under which steep ablation front and Newton rings can be expected, for different materials. The combined results support the current "bubble" model of ablation by fluences near the ablation threshold (with femtosecond NIR pulses). Long lasting surface expansion indicates that changes in expanding material can be contributed to void formation inside the material and support the important role

of tensile stresses. Irreversible surface expansion above the ablation threshold and expansion velocity which scales linearly with fluence indicate that the phase explosion model of ablation is applicable for higher fluences.

Interferometric measurements on metals are more complex compared with similar measurements on semiconductors, and improvement in sample surface quality will improve measurements accuracy. In the case of gold films it became apparent that deposited energy can not be uniquely determined, while reflectivity can change significantly from tabulated values. In this respect, measurements of self reflectivity for the investigated fluence regime could give a better insight into the energy deposition that induces the ablation process.

The first results of experiments studying the dynamics of ablation by XUV pulses that took place at FLASH in Hamburg are presented in the Chapter 4. Experimental data confirm the absence of absorption nonlinearities and increased absorption depth, with respect to fs optical excitation. To gather more detailed data, both spatial and temporal resolution will need to be improved. Increased pulse energies are expected to allow the excitation of a larger spot on the sample, and this will permit surface expansion dynamics to be monitored using the interferometric technique described in Chapter 3.

As a complement to the XUV pump optical probe experiments described in Chapter 4, a new type of XUV probe optical pump experiments are expected to give insight into void formations in expanding material, during ablation in the early stage, using diffractive imaging [101].

Appendix A

Single pulse selection

The goal is to select a single laser pulse from the 1kHz train. Limiting factors are the beam size, which is fixed and the speed of mechanical devices used to interrupt the pulse train. At this moment of technological development, the mechanical shutters with an aperture size of approximately 1cm have a minimum opening time in the 10ms range (3ms rise time, 1ms full open and 3ms fall time). We use the optical chopper to reduce the repetition rate in range (50Hz) where the mechanical shutter can open and close between two subsequent pulses.

The chopper is a model from Thorlabs (MC1000A), which has an option for external synchronization. The master clock signal from the KHz laser system is fed to the signal frequency divider with adjustable delay. Frequency is reduced by a factor of two and the 500Hz signal is used to synchronize the chopper, and the adjustable delay is used to precisely adjust the timing between the laser pulse and chopper synchronization. As one can see in Figure 3.2, the blade periphery has 10 rectangular openings, which are used for internal synchronization of the chopper. Synchronizing the chopper with 500Hz results in 50 revolutions of the blade per second. The distance from the center and the aperture rotation speed (50Hz) result in an aperture velocity of 12.3m/s. Moving with this velocity, the aperture of diameter d=12mm, sweeps the position where the laser beam is in time $\tau \approx$0.98ms, so that only one pulse from the KHz train is selected.

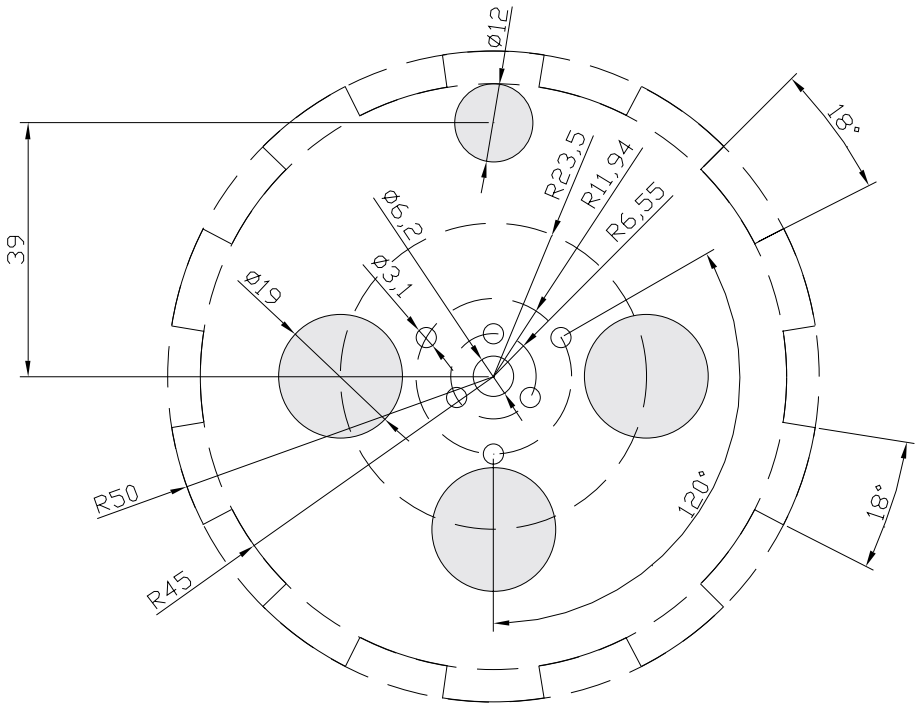

Figure A.1: Optical chopper custom blade, smaller aperture (12mm diam), at 39mm from center, is used to select one pulse from KHz train. The three bigger openings (19mm diameter at 23.5mm from center) are there to return center of mass back to the center of chopper blade.

The maximum beam size (FWHM) that can pass the aperture, without being clipped is approximately one third of the aperture radius (less than 0.01% of energy is lost due to clipping). The physical size of the chopper blade (50mm maximal radius) limits the maximal diameter of the aperture on the blade. After the compressor beam has $\approx$ 8mm FWHM, and it will be cut on the blade aperture. Just after the last amplifier stage the beam has FWHM $\approx$ 1mm, which seemed to be a good place for the chopper, before the already mentioned problem of the compressor thermal loading was discovered.

The solution to both problems was found by using another compressor with a smaller beam size (FWHM $\approx$ 4mm) and placing the chopper after the compressor, and avoiding influence on the laser system.

A commercial mechanical shutter (opening and closing rise time $\approx$ 3ms) is used

to select one pulse from the 50Hz train.

Due to high intensity of the chopped laser beam, the scattered light of blocked pulses was intense enough to interfere with the so-called "Photo-interrupter speed sensor". For this purpose, a special shield was designed that isolated above mentioned sensor from ambient light.

Appendix B

Description of the investigated metal samples

The investigated materials are platinum(Pt) and gold(Au) films on silicon(Si) wafers and titanium(Ti) and aluminium(Al) films on microscope glass substrates.

Table B.1: Gold sample thickness and structure

Thickness and material	Total thickness	In text referred to as
25 ÅPt + 310ÅAu	335Å	34 nm
25 ÅPt + 542ÅAu	567Å	57 nm
25 ÅPt + 1228ÅAu	1253Å	125 nm

Table B.2: Platinum sample thickness

Thickness	In text referred to as
314 Å	31 nm
602 Å	60 nm
1039 Å	104 nm

The platinum and gold samples are silicon wafers coated with metal films. The platinum samples are deposited directly on a silicon sample, while a gold

film is deposited on a thin platinum layer (25). The thin platinum layer serves as an adhesion layer, as the gold deposited directly on the silicon-oxide surface does not adhere. The metal films are prepared by sputter deposition and are polycrystalline. The samples are provided by Quantum Science Research at Hewlett-Packard Laboratories in USA. The exact thicknesses and labels used further in text are given in tables B.1 and B.2.

The titanium and aluminium samples are made by arc vaporization deposition, at the University of Duisburg-Essen. The titanium samples are more than 500 nm thick, while the aluminium ones are made in 100 nm and 400nm thicknesses.

Appendix C

Properties of Gold and Aluminium

Table C.1: Properties of Gold [39]

Heat capacity	25 418	J· K^{-1} · mol $^{-1}$
Density	19 300	kg/m^3
Latent heat of fusion	63 705	J/kg
Melting temperature	1337	K
Sound speed	2030	m/s
Linear expansion coefficient	1.4x10^{-5}	1/K
Bulk modulus	220	GPa

Table C.2: Properties of Aluminium [39]

Heat capacity	24 200	J· K^{-1} · mol $^{-1}$
Density	2 700	kg/m^3
Latent heat of fusion	3 960	J/kg
Melting temperature	933	K
Sound speed	5 000	m/s

Appendix D

Experimentally determined reflectivity of Au

Table D.1: Experimentally measured reflectivity for gold films of different thicknesses. The first column represents film thickness, and the second one reflectivity for the corresponding films.

Thickness [nm]	Reflectivity
34	0.82
57	0.93
125	0.944

Bibliography

[1] A. Borowiec, M. MacKenzie, G. C. Weatherly, and H. K. Haugen. Femtosecond laser pulse ablation of GaAs and InP: studies utilizing scanning and transmission electron microscopy. *Applied Physics A: Materials Science & Processing*, 77:411–417, 2003.

[2] W. Zapka, W. Ziemlich, and A. C. Tam. Efficient pulsed laser removal of 0.2 mu m sized particles from a solid surface. *Applied Physics Letters*, 58(20):2217–2219, 1991.

[3] Jean-Numa Gillet, Jean-Yves Degorce, and Michel Meunier. General model and segregation coefficient measurement for ultrashallow doping by excimer laser annealing. *Applied Physics Letters*, 86(22):222104, 2005.

[4] S. R. Shinde, S. B. Ogale, R. L. Greene, T. Venkatesan, P. C. Canfield, S. L. Bud'Ko, G. Lapertot, and C. Petrovic. Superconducting mgb_2 thin films by pulsed laser deposition. *Applied Physics Letters*, 79:227–+, July 2001.

[5] S. Amoruso, G. Ausanio, R. Bruzzese, M. Vitiello, and X. Wang. Femtosecond laser pulse irradiation of solid targets as a general route to nanoparticle formation in a vacuum. *Physical Review B (Condensed Matter and Materials Physics)*, 71(3):033406, 2005.

[6] Thornton Ernest Glover. Hydrodynamics of particle formation following femtosecond laser ablation. *J. Opt. Soc. Am. B*, 20(1):125–131, 2003.

[7] J.-P. Sylvestre, A. V. Kabashin, E. Sacher, and M. Meunier. Femtosecond laser ablation of gold in water: influence of the laser-produced plasma on the nanoparticle size distribution. *Applied Physics A: Materials Science & Processing*, 80:753–758, February 2005.

[8] A.V. Kabashin, M. Meunier, C. Kingston, and J.H.T. Luong. Fabrication and characterization of gold nanoparticles by femtosecond laser ablation in an aqueous solution of cyclodextrins. *Journal of Physical Chemistry B*, 107(19):4527–4531, 2003.

[9] A. Vogel and V. Venugopalan. Mechanisms of pulsed laser ablation of biological tissues. *Chemical Reviews*, 103(5):2079–2079, 2003.

[10] F. Korte, J. Serbin, J. Koch, A. Egbert, C. Fallnich, A. Ostendorf, and B. N. Chichkov. Towards nanostructuring with femtosecond laser pulses. *Applied Physics A: Materials Science & Processing*, 77:229–235, 2003.

[11] P. P. Pronko, S. K. Dutta, J. Squier, J. V. Rudd, D. Du, and G. Mourou. Machining of sub-micron holes using a femtosecond laser at 800 nm. *Optics Communications*, 114:106–110, February 1995.

[12] C. Momma, B. N. Chichkov, S. Nolte, F. von Alvensleben, A. Tünnermann, H. Welling, and B. Wellegehausen. Short-pulse laser ablation of solid targets. *Optics Communications*, 129:134–142, February 1996.

[13] V.V. Temnov, K. Sokolowski-Tinten, N. Stojanovic, S. Kydryashov, D. von der Linde, B. Kogan, B. Weyers, R. Mller, J. Seekamp, and C. Sotomayor-Torres. Microscopic characterization of ablation craters produced by femtosecond laser pulses. In C. R. Phipps, editor, *SPIE Proceedings, High Power Laser Ablation IV*, volume 4760, 2002.

[14] K. Sokolowski-Tinten, J. Bialkowski, A. Cavalleri, D. von der Linde, A. Oparin, J. Meyer-ter Vehn, and S. I. Anisimov. Transient states of

matter during short pulse laser ablation. *Phys. Rev. Lett.*, 81(1):224–227, Jul 1998.

[15] Sokolowski K., Bialkowski J., Cavalleri A., and Linde D. von der. Time resolved studies of femtosecond laser induced ablation from solid surfaces. In *Ultrafast Phenomena XI*, volume 63 of *Springer Series in Chemical Physics*, page 316, Heidelberg, 1998. Springer.

[16] Dietrich von der Linde and Klaus Sokolowski-Tinten. Physical mechanisms of short-pulse laser ablation. volume 3734, pages 2–9. SPIE, 1999.

[17] N. A. Inogamov, S. I. Anisimov, and B. Retfeld. Rarefaction wave and gravitational equilibrium in a two-phase liquid-vapor medium. *Soviet Journal of Experimental and Theoretical Physics*, 88:1143–1150, June 1999.

[18] N. A. Inogamov, Yu. V. Petrov, S. I. Anisimov, A. M. Oparin, N. V. Shaposhnikov, D. von der Linde, and J. Meyer ter Vehn. Expansion of matter heated by an ultrashort laser pulse. *JETP Letters*, 69(4), 1999.

[19] S. I. Anisimov, N. A. Inogamov, A. M. Oparin, B. Rethfeld, T. Yabe, M. Ogawa, and V. E. Fortov. Pulsed laser evaporation: equation-of-state effects. *Applied Physics A: Materials Science & Processing*, 69:617–620, 1999.

[20] V. V. Zhakhovskiĭ, K. Nishihara, S. I. Anisimov, and N. A. Inogamov. Molecular-Dynamics Simulation of Rarefaction Waves in Media That Can Undergo Phase Transitions. *Soviet Journal of Experimental and Theoretical Physics Letters*, 71:167–+, February 2000.

[21] Danny Perez and Laurent J. Lewis. Molecular-dynamics study of ablation of solids under femtosecond laser pulses. *Phys. Rev. B*, 67(18):184102, May 2003.

[22] S. I. Anisimov, V. V. Zhakhovskiĭ, N. A. Inogamov, K. Nishihara, A. M. Oparin, and Y. V. Petrov. Destruction of a Solid Film under the Action of Ultrashort Laser Pulse. *Soviet Journal of Experimental and Theoretical Physics Letters*, 77:606–+, June 2003.

[23] M. C. Downer, R. L. Fork, and C. V. Shank. Femtosecond imaging of melting and evaporation at a photoexcited silicon surface. *Journal of the Optical Society of America B Optical Physics*, 2:595–599, April 1985.

[24] V. V. Temnov, K. Sokolowski-Tinten, P. Zhou, and D. von der Linde. Femtosecond time-resolved interferometric microscopy. *Applied Physics A: Materials Science & Processing*, 78:483–489, 2004.

[25] Vasily V. Temnov. *Ultrafast Laser-induced Phenomena in Solids Studied by Time-resolved Interferometry.* PhD thesis, University of Duisburg-Essen, 2004.

[26] K. Sokolowski-Tinten, J. Bialkowski, and D. von der Linde. Ultrafast laser-induced order-disorder transitions in semiconductors. *Phys. Rev. B*, 51(20):14186–14198, May 1995.

[27] K. Widmann, T. Ao, M. E. Foord, D. F. Price, A. D. Ellis, P. T. Springer, and A. Ng. Single-state measurement of electrical conductivity of warm dense gold. *Physical Review Letters*, 92(12):125002, 2004.

[28] T. Ao, Y. Ping, K. Widmann, D. F. Price, E. Lee, H. Tam, P. T. Springer, and A. Ng. Optical properties in nonequilibrium phase transitions. *Physical Review Letters*, 96(5):055001, 2006.

[29] L. Ke K. Eidmann F. Rosmej T. Schlegel K. Sokolowski-Tinten D. von der Linde J. Meyer-ter Vehn, A. Krenz and T. Tschentscher. Third international conference on inertial fusion sciences and applications(ifsa 2003). In *Monterey, CA, 2003 (American Nuclear Society, LaGrange Park, IL, 2004), p. 912.*, 2003.

[30] R. C. Cauble J. S. Wark A. Ng S. J. Rose C. Lewis D. Riley J. C. Gauthier R. W. Lee, H. A. Baldis and P. Audebert. Plasma-based studies with intense x-ray and particle beam sources. *Laser and Particle Beams*, 20:527–536, Jul 2002.

[31] M.V. Yurkov E.L. Saldin, E.A. Schneidmiller. *The physics of free electron lasers*. Springer, Berlin, 2000.

[32] S. Anisimov. Ablated matter expansion and crater formation under the action of ultrashort laser pulse. *Journal of Experimental and Theoretical Physics*, 103:183–197(15), August 2006.

[33] P. Lorazo, L. J. Lewis, and M. Meunier. Thermodynamic pathways to melting, ablation, and solidification in absorbing solids under pulsed laser irradiation. *Physical Review B*, 73(13):134108–+, April 2006.

[34] R. Kelly. Comments on explosive mechanisms of laser sputtering. *Applied Surface Science*, 96:205–215, April 1996.

[35] Miotello A. and Kelly R. Laser-induced phase explosion: new physical problems when a condensed phase approaches the thermodynamic critical temperature. *Applied Physics A Materials Science Processing*, 69, 1999.

[36] V. P. (Van P.) Carey. *Liquid-vapor phase-change phenomena: an introduction to the thermophysics of vaporization and condensation processes in heat transfer equipment*.

[37] Baerbel Rethfeld, Klaus Sokolowski-Tinten, and Dietrich von der Linde. Excitation, melting, ablation: theoretical investigations of key processes during ultrashort pulsed laser machining. volume 5063, pages 71–80. SPIE, 2003.

[38] Igor' V. Lomonosov, Aleksey V. Bushman, and Vladimir E. Fortov. Equations of state for metals at high energy densities. volume 309, pages 117–120. AIP, 1994.

[39] A. M. Howatson, P. G. Lund, and J. D. Todd. *Engineering tables and data*. Chapman and Hall, London, 1972.

[40] E. D. Palik ed. *Handbook of Optical Constants of Solids*. Academic Press, 1985.

[41] D Riley, A J Langley, P F Taday, W Shaikh, and I McCormack. Reflectivity experiments with 60 femtosecond laser pulses. *Journal of Physics D: Applied Physics*, 31(5):515–518, 1998.

[42] S. D. Brorson, J. G. Fujimoto, and E. P. Ippen. Femtosecond electronic heat-transport dynamics in thin gold films. *Phys. Rev. Lett.*, 59(17):1962–1965, Oct 1987.

[43] G. I. Kanel, S. V. Razorenov, A. Bogatch, A. V. Utkin, V. E. Fortov, and D. E. Grady. Spall fracture properties of aluminum and magnesium at high temperatures. *Journal of Applied Physics*, 79(11):8310–8317, 1996.

[44] E. Leveugle, D. S. Ivanov, and L. V. Zhigilei. Photomechanical spallation of molecular and metal targets: molecular dynamics study. *Applied Physics A: Materials Science & Processing*, 79:1643–1655, 2004.

[45] J. C. Bushnell and D. J. McCloskey. Thermoelastic Stress Production in Solids. *Journal of Applied Physics*, 39:5541–5546, November 1968.

[46] G. Paltauf and P.E. Dyer. Photomechanical processes and effects in ablation. *Chemical Reviews*, 103(2):487–518, 2003.

[47] Alexander A. Oraevsky, Steven L. Jacques, and Frank K. Tittel. Mechanism of laser ablation for aqueous media irradiated under confined-stress conditions. *Journal of Applied Physics*, 78(2):1281–1290, 1995.

[48] G. Paltauf and H. Schmidt-Kloiber. Microcavity dynamics during laser-induced spallation of liquids and gels. *Applied Physics A: Materials Science & Processing*, 62:303–311, April 1996.

[49] D. Kim, M. Ye, and C. P. Grigoropoulos. Pulsed laser-induced ablation of absorbing liquids and acoustic-transient generation. *Applied Physics A: Materials Science & Processing*, 67:169–181, 1998.

[50] Tatiana E. Itina, Mikhail Mamatkulov, and Marc Sentis. Nonlinear fluence dependencies in femtosecond laser ablation of metals and dielectric materials. *Optical Engineering*, 44(5):051109, 2005.

[51] C. Thomsen, H. T. Grahn, H. J. Maris, and J. Tauc. Surface generation and detection of phonons by picosecond light pulses. *Phys. Rev. B*, 34(6):4129–4138, Sep 1986.

[52] J. I. Etcheverry and M. Mesaros. Molecular dynamics simulation of the production of acoustic waves by pulsed laser irradiation. *Phys. Rev. B*, 60(13):9430–9434, Oct 1999.

[53] Leonid V. Zhigilei and Barbara J. Garrison. Microscopic mechanisms of laser ablation of organic solids in the thermal and stress confinement irradiation regimes. *Journal of Applied Physics*, 88(3):1281–1298, 2000.

[54] A. G. Zhidkov, L. V. Zhigilei, A. Sasaki, and T. Tajima. Short-laser-pulse-driven emission of energetic ions into a solid target from a surface layer spalled by a laser prepulse. *Applied Physics A: Materials Science & Processing*, 73:741–747, 2001.

[55] L.V. Zhigilei, E. Leveugle, B.J. Garrison, Y.G. Yingling, and M.I. Zeifman. Computer simulations of laser ablation of molecular substrates. *Chemical Reviews*, 103(2):321–348, 2003.

[56] D. Strickland and G. Mourou. Compression of amplified chirped optical pulses. *Optics Communications*, 55:447–449, October 1985.

[57] D. Strickland and G. Mourou. Compression of amplified chirped optical pulses. *Optics Communications*, 56:219–221, December 1985.

[58] M. Pessot, P. Maine, and G. Mourou. 1000 times expansion/compression of optical pulses for chirped pulse amplification. *Optics Communications*, 62:419–421, June 1987.

[59] M. Pessot, J. A. Squier, G. A. Mourou, and D. J. Harter. Chirped-pulse amplification of 100-fsec pulses. *Optics Letters*, 14:797–799, August 1989.

[60] F. Verluise, P. Tournois, V. Laude, Z. Cheng, and C. Spielmann. Acousto-optic filter for femtosecond laser pulse shaping, gainnarrowing and phase distortion compensation. pages 442–443, San Francisco, CA, USA, May 2000. Conference on Lasers and Electro-Optics, (CLEO 2000).

[61] T. Masubuchi, H. Furutani, H. Fukumura, and H. Masuhara. Laser-induced nanometer-nanosecond expansion and contraction dynamics of poly(methyl methacrylate) film studied by time-resolved interferometry. *Journal of Physical Chemistry B*, 105(13):2518–2524, 2001.

[62] L. A. Gizzi, M. Galimberti, A. Giulietti, D. Giulietti, P. Koester, L. Labate, P. Tomassini, Ph. Martin, T. Ceccotti, P. De Oliveira, and P. Monot. Femtosecond interferometry of propagation of a laminar ionization front in a gas. *Physical Review E (Statistical, Nonlinear, and Soft Matter Physics)*, 74(3):036403, 2006.

[63] J. P. Geindre, P. Audebert, A. Rousse, F. Falliès, J. C. Gauthier, A. Mysyrowicz, A. Dos Santos, G. Hamoniaux, and A. Antonetti. Frequency-domain interferometer for measuring the phase and amplitude of a femtosecond pulse probing a laser-produced plasma. *Optics Letters*, 19:1997–1999, December 1994.

[64] R. Evans, A. D. Badger, F. Falliès, M. Mahdieh, T. A. Hall, P. Audebert, J.-P. Geindre, J.-C. Gauthier, A. Mysyrowicz, G. Grillon, and A. Antonetti. Time- and space-resolved optical probing of femtosecond-laser-driven shock waves in aluminum. *Phys. Rev. Lett.*, 77(16):3359–3362, Oct 1996.

[65] P. Audebert, Ph. Daguzan, A. Dos Santos, J. C. Gauthier, J. P. Geindre, S. Guizard, G. Hamoniaux, K. Krastev, P. Martin, G. Petite, and A. Antonetti. Space-time observation of an electron gas in sio_2. *Phys. Rev. Lett.*, 73(14):1990–1993, Oct 1994.

[66] Jr. M. Francon. *Optical Interferometry.* (Academic Press, New York, 1966.

[67] Donald J. Bone, H.-A. Bachor, and R. John Sandeman. Fringe-pattern analysis using a 2-d fourier transform. *Appl. Opt.*, 25(10):1653, 1986.

[68] Claude Roddier and Francois Roddier. Interferogram analysis using fourier transform techniques. *Appl. Opt.*, 26(9):1668, 1987.

[69] A. S. Zakharov, M. V. Volkov, I. P. Gurov, V. V. Temnov, K. Sokolovski-Tinten, and D. von der Linde. Interferometric diagnostics of ablation craters formed by femtosecond laser pulses. *J. Opt. Technol.*, 69(7):478, 2002.

[70] V.V. Temnov, K. Sokolowski-Tinten, P. Zhou, and D. von der Linde. Femtosecond time-resolved interferometric microscopy. *Applied Physics A Materials Science and Processing*, 78, 2004.

[71] Vasily V. Temnov, Klaus Sokolowski-Tinten, Ping Zhou, and Dietrich von der Linde. Ultrafast imaging interferometry at femtosecond-laser-excited surfaces. *J. Opt. Soc. Am. B*, 23(9):1954–1964, 2006.

[72] Robinson W David and Reid Graeme. *Interferogram Analysis Digital Fringe Pattern Measurement Techniques.* IOP, Bristol, 1993.

[73] M. Takeda, H. Ina, and S. Kobayashi. Fourier-transform method of fringe-pattern analysis for computer-based topography and interferometry. *Journal of the Optical Society of America (1917-1983)*, 72:156–+, January 1982.

[74] A.V. Oppenheim and R.W. Schafer. *Discrete-Time Signal Processing*. Upper Saddle River, NJ: Prentice-Hall, 1999.

[75] S. Jr. Lawrence Marple. *Digital Spectral Analysis with Applications*. Prentice Hall, January 1987.

[76] J. M. Elson and C. C. Sung. Intrinsic and roughness-induced absorption of electromagnetic radiation incident on optical surfaces. *Applied Optics*, 21:1496–1501, April 1982.

[77] J. M. Liu. Simple technique for measurements of pulsed gaussian-beam spot sizes. *Opt. Lett.*, 7(5):196, 1982.

[78] R. Ernstorfer, M. Harb, T. Dartigalongue, C. T. Hebeisen, R. E. Jordan, L. Zhu, and R. J. D. Miller. Femtosecond electron diffraction study on the heating and melting dynamics of gold. In *Ultrafast Phenomena XV*, volume 88, pages 755–757, Pacific Grove, USA, JulyAugust 2007. Proceedings of the 15th International Conference, Springer Berlin Heidelberg.

[79] American Institute of Physics. *American Institute of Physics handbook: Section editors: Bruce H. Billings [and others] Coordinating editor: Dwight E. Gray*. McGraw-Hill, New York, 3d ed. edition, 1972. Includes bibliographies.

[80] Jrg Bialkowski. *Femtosekunden-Laserinducierter Materialabtrag*. PhD thesis, Universitt-Gesamthochschule-Essen, 1998.

[81] H. Tamura, T. Kohama, K. Kondo, and M. Yoshida. Femtosecond-laser-induced spallation in aluminum. *Journal of Applied Physics*, 89(6):3520–3522, 2001.

[82] J. E. Sipe, Jeff F. Young, J. S. Preston, and H. M. van Driel. Laser-induced periodic surface structure. i. theory. *Phys. Rev. B*, 27(2):1141–1154, Jan 1983.

[83] Jeff F. Young, J. S. Preston, H. M. van Driel, and J. E. Sipe. Laser-induced periodic surface structure. ii. experiments on ge, si, al, and brass. *Phys. Rev. B*, 27(2):1155–1172, Jan 1983.

[84] J. F. Young, J. E. Sipe, J. S. Preston, and H. M. van Driel. Laser-induced periodic surface damage and radiation remnants. *Applied Physics Letters*, 41:261–264, August 1982.

[85] Y. Kanemitsu, H. Kuroda, and S. Shionoya. Formation of Periodic Ripple Structures in Picosecond Pulsed Laser Annealing of Ion-Implanted Silicon. *Japanese Journal of Applied Physics*, 23:1060–+, August 1984.

[86] B Tan and K Venkatakrishnan. A femtosecond laser-induced periodical surface structure on crystalline silicon. *Journal of Micromechanics and Microengineering*, 16(5):1080–1085, 2006.

[87] X. C. Wang, G. C. Lim, F. L. Ng, W. Liu, and S. J. Chua. Femtosecond pulsed laser-induced periodic surface structures on GaN/sapphire. *Applied Surface Science*, 252:1492–1497, December 2005.

[88] Robert Hooke. *Micrographia: or, Some physiological descriptions of minute bodies made by magnifying glasses. With observations and inquiries thereupon.* Printed by J. Martyn and J. Allestry, 1665.

[89] B. Hoanca. Principles of Optics, by Max Born and Emil Wolf. *Optics & Photonics News*, 11:45–+, September 2000.

[90] Changrui Cheng and Xianfan Xu. Mechanisms of decomposition of metal during femtosecond laser ablation. *Physical Review B (Condensed Matter and Materials Physics)*, 72(16):165415, 2005.

[91] Andrea Cavalleri, Klaus Sokolowski-Tinten, Joerg Bialkowski, Michaela Schreiner, and Dietrich von der Linde. Femtosecond melting and ablation of semiconductors studied with time of flight mass spectroscopy. *Journal of Applied Physics*, 85(6):3301–3309, 1999.

[92] D. von der Linde and H. Schüler. Breakdown threshold and plasma formation in femtosecond laser-solid interaction. *Journal of the Optical Society of America B Optical Physics*, 13:216–222, January 1996.

[93] A. A. Maznev, J. Hohlfeld, and J. Gudde. Surface thermal expansion of metal under femtosecond laser irradiation. *Journal of Applied Physics*, 82(10):5082–5085, 1997.

[94] A. Rousse, C. Rischel, S. Fourmaux, I. Uschmann, S. Sebban, G. Grillon, Ph. Balcou, E. Forster, J. P. Geindre, P. Audebert, J. C. Gauthier, and D. Hulin. Non-thermal melting in semiconductors measured at femtosecond resolution. *Nature*, 410(6824):65–68, Mar 2001. 10.1038/35065045.

[95] Bradley J. Siwick, Jason R. Dwyer, Robert E. Jordan, and R. J. Dwayne Miller. An Atomic-Level View of Melting Using Femtosecond Electron Diffraction. *Science*, 302(5649):1382–1385, 2003.

[96] Henke B.L., Gullikson E.M., and Davis J.C. X-ray interactions: photoabsorption, scattering, transmission, and reflection at e=50-30000 ev, z=1-92. *Atomic Data and Nuclear Data Tables*, 54(2):181–342, July 1993.

[97] C. V. Shank, R. Yen, and C. Hirlimann. Time-resolved reflectivity measurements of femtosecond-optical-pulse-induced phase transitions in silicon. *Phys. Rev. Lett.*, 50(6):454–457, Feb 1983.

[98] P. Stampfli and K. H. Bennemann. Time dependence of the laser-induced femtosecond lattice instability of si and gaas: Role of longitudinal optical distortions. *Phys. Rev. B*, 49(11):7299–7305, Mar 1994.

[99] M. van Allmen and B. Blatter. *Laser-Beam Interactions with Materials*, volume Vol. 2. Springer Series in Material Science (Springer, Berlin), 1998.

[100] N. Stojanovic, D. von der Linde, K. Sokolowski-Tinten, U. Zastrau, F. Perner, E. Forster, R. Sobierajski, R. Nietubyc, M. Jurek, D. Klinger, J. Pelka, J. Krzywinski, L Juha, J. Cihelka, A. Velyhan, S. Koptyaev,

V. Hajkova, J. Chalupsky, J. Kuba, T. Tschentscher, S. Toleikis, S. Dusterer, and H. Redlin. Ablation of solids using a femtosecond extreme ultraviolet free electron laser. *Applied Physics Letters*, 89(24):241909, 2006.

[101] H. N. Chapman, A. Barty, M. J. Bogan, S. Boutet, M. Frank, S. P. Hau-Riege, S. Marchesini, B. W. Woods, S. Bajt, W. H. Benner, R. A. London, E. Plönjes, M. Kuhlmann, R. Treusch, S. Düsterer, T. Tschentscher, J. R. Schneider, E. Spiller, T. Möller, C. Bostedt, M. Hoener, D. A. Shapiro, K. O. Hodgson, D. van der Spoel, F. Burmeister, M. Bergh, C. Caleman, G. Huldt, M. M. Seibert, F. R. N. C. Maia, R. W. Lee, A. Szöke, N. Timneanu, and J. Hajdu. Femtosecond diffractive imaging with a soft-X-ray free-electron laser. *Nature Physics*, 2:839–843, December 2006.